Doctoral Dissertation

Study of charge state of Au nanoclusters on oxidized rutile TiO_2(110) surface by atomic force microscopy/Kelvin probe force microscopy

Qiang Zhu

June 2023

Graduate School of Engineering
Osaka University

Abstract

Surface catalytic reactions based on metal oxide semiconductors have been widely researched for environmental remediation and energy conversion due to their unique properties of selectivity, stability, and high activity. In the TiO_2 catalytic system, surface defects, such as oxygen vacancy, Ti interstitial, and polarons, play a crucial role in its catalytic activity. Furthermore, Au nanocluster-mediated catalytic reactions exhibit high activity. We chose a relatively active crystal face (110) for our research. Based on the TiO_2(110) surface, the adsorption characteristics of reactants and the charge states of Au nanoclusters are strongly influenced by these surface defects. However, the charge state of Au and its application for CO oxidation on the TiO_2(110) surface remain unclear in experiments. A lot of research on the charge state and manipulation of adsorbates on rutile TiO_2(110) has been investigated by theoretical calculations and experimental works. There is a lack of systematic experimental studies about surface and subsurface defects of TiO_2(110) for surface adsorptions, and the catalytic oxidation mechanism of carbon monoxide has not been fully understood. Therefore, it is important to clarify the surface and subsurface defects of TiO_2(110) for the adsorption of reactant molecules, the adsorption properties of catalytic reactions, and the overall performance of the charge states of Au nanoclusters for catalyst.

In this doctoral thesis, the charge states of Au nanoclusters on the TiO_2(110) surface were investigated by atomic force microscopy (AFM) and Kelvin probe force microscopy (KPFM) with nanoscale resolution in ultra-high vacuum at 78 K. To investigate the charge states of Au nanoclusters for the oxidation catalysis of carbon monoxide, my first step is identification of the surface adsorptions and defects. This identification is based on the analysis of the charge states of Au nanoclusters, which can be influenced by the presence of surface defects. Adsorptions and defects on the TiO_2(110) surface, such as H_2O, hydroxyl, and oxygen vacancy defect, are still not systematic identified by experimental condition. the water molecule, hydroxyl, and oxygen vacancy have successfully identified by KPFM at different tip modes. The identification process was carried out by correlating the charge states of these species with the corresponding tip modes during the KPFM measurements. Furthermore, we have successfully operated with important adsorbates such as water and hydroxyl, enabling us to design the catalytic reaction pathway. And then, the adsorption and motion of carbon monoxide (CO) have been investigated at 78 K. CO molecules are unstable on the TiO_2(110) surface at 78 K, to research its reaction mechanism, oxygen molecules are exposed to the surface. And it is found that oxygen adatoms (O_{ad}) can enhance the adsorption of CO molecules. Furthermore, the moving of CO molecules in two-dimensional was realized, which can be used for designing CO to the active catalytic reaction sites. Finally, the Au nanoclusters were adsorbed on the TiO_2(110)

surface, and the charge states of Au nanoclusters were identified. This is essential for understanding the Au effect of the CO catalytic reaction. By applying a bias voltage to the CO-Au-O_{ad} complexes, CO was oxidized and desorbed from the surface.

This thesis can gain insights into the catalytic mechanisms and develop strategies to enhance catalytic activity, selectivity, and stability by researching the surface and subsurface defects, reactants adsorption, and Au charge states on TiO_2(110) surface. This study is not only a fundamental insight, but also an important issue for the application of catalysis and a significant contribution to the development of applied physics, surface science and especially nanocatalysis science.

Contents

Chapter 1 Introduction

1.1 Background

1.1.1 Surface catalysts

To improve the chemical reaction rate by lowering the activation energy required for the reaction to occur, catalysis has been invented and produced [1-6]. Catalysis is a concrete manifestation of the complexity and controllability of reactions, which is a typical representative of intersection of physical chemistry with related disciplines. Catalysts work by providing an alternative pathway for the reaction that has a lower activation energy than the uncatalyzed reaction, allowing the reaction to occur more quickly and with less energy input. By researching the interaction between molecule and surface, lots of materials are produced and used to many reaction fields. Some common examples of catalysts include enzymes in biological systems, transition metal complexes in industrial chemical reactions, and acids and bases in organic chemistry. In 1909, a German chemist Fritz Haber discovered an effective method to synthesis NH_3 by N_2 and H_2. He also produced a lot of cheap fertilizers to promote agricultural production [7,8]. And farmers have got a higher harvest than before, which increased the global food supply. After that, catalysis mediated chemical reactions were put forward, such as the air purification, wastewater treatment, and conversion of noxious gas. Catalysis plays a crucial role in many areas of chemistry and industry, including the production of fuels, plastics, and pharmaceuticals. It also has important environmental applications, such as in the catalytic converters used in automobiles to reduce emissions of harmful pollutants [9-11]. Surface catalysis refers to the process by which a catalyst promotes a chemical reaction by providing a surface on which reactant molecules can come together and react, which is the basic science to study the adsorption, diffusion, reaction, and desorption of reaction molecule on the catalyst surface. Therefore, surface catalysis becomes the scientific basics of catalytic science and technology [12-14]. This surface can be a solid, liquid, or gas and is often made up of atoms or molecules that are arranged in a specific way to allow for efficient and effective catalysis [15-18]. Generally, surface science is a technique that mainly research on the chemical and physical reactions with relevant characteristics on the interface of two phases, such as the liquid-gas, liquid-liquid and liquid-solid interfaces. At present, surface catalysis and heterogeneous catalysis have become one of the most active frontier research fields in physical chemical science. In the past twenty years,

surface catalytic has been developed as a branch of science.

Up to now, catalysis is used in many areas, such as crude oil refining and petro-chemistry, organic and inorganic chemicals, energy-conversion production, and environmental protection. Most of the catalysts are solid phase catalysts, which rely on the participation of atoms or ions on the solid surface to reduce the activation energy of the reaction and increase the reaction rate. Solid catalytic reaction, also known as heterogeneous catalytic reaction, includes the main processes of reactant surface adsorption, surface diffusion, chemical bonding and bond breaking, intramolecular rearrangement, and product desorption. In catalytic research, solid catalysts have advantages of long service life, easy activation, regeneration and recycle, and can be operated automatically during operation. Surface catalysis based solid catalysts is mainly studying the surface structure and mechanism of catalysis [19-21].

Usually, noble metals, such as palladium (Pd), platinum (Pt), and gold (Au), are deposited on the catalytic reaction system in the catalytic process [22-24]. Molecules have a discrete electronic structure, the quantum effect (called quantum confinement) will appear when the size of nanoparticles (NPs) is less than 2 nm. And adsorbed noble metals in large NPs are capable of surface plasmon resonance effect. The trapped free electrons on the noble metals makes band structure split into highest occupied molecular orbital (HOMO) and lowest unoccupied molecular orbital (LUMO) level, respectively. In this way, the noble metals provide exciting opportunities for the application of highly efficient catalytic reactions.

In the surface catalytic reactions research based on TiO_2(110), comparing to other noble metals, Au nanoclusters exhibits a milder adsorption effect on the surface and higher activity for catalyst. A considerable amount of research has been dedicated to discovering the chemical properties or characteristics responsible for the outstanding activity of gold in a particular activity at nanoscale. According to the calculations, different sizes and locations of Au possess different charge states. Furthermore, charge state of the Au species has been proposed to play a crucial role for the enhancement of its catalytic activity. Until now, charge states and its application for waste gas treatment of Au nanoclusters still lack sufficient verification in the experiment.

1.1.2 Mechanism of surface catalytic processes

Reaction kinetics refers to the study of how chemical reactions proceed over time, including the rates at which reactants are consumed and products are formed. Reaction kinetics can be influenced by a variety of factors, including temperature, pressure, concentration, and the presence of a catalyst. The reactants adsorb onto the surface of the catalyst, where they undergo chemical reactions with each other or with other

molecules in the environment. The study of surface catalysis and reaction kinetics is important in a wide range of fields, including materials science, chemical engineering, and catalysis research. By understanding the mechanisms of surface catalysis and reaction kinetics, researchers can develop new and more efficient catalysts for use in industrial processes, as well as gain insight into the fundamental chemistry of complex reactions.

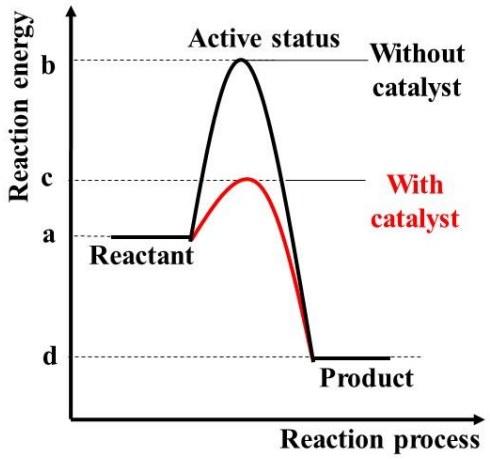

Figure 1.1 The effect of catalyst on the activation energy of a reaction.

Catalysis can be classified into two types, the one is homogeneous, the other is heterogeneous, and main catalytic processes are heterogeneous catalysis in nature [25,26]. In the heterogeneous reactions, solid catalysts are most widely used. The catalysis of solid catalysts is derived from the unsaturation of the coordination of atoms on the solid surface, so that the solid surface can adsorb and activate molecules in the surrounding environment [27]. At least one reactant molecule is adsorbed on the surface of the solid catalyst and activated in the catalytic reaction processes. Subsequently, these reactant molecules conduct physical chemical reactions on the surface of the solid catalyst, generating adsorption products through intermediate species [28]. The final adsorbed product desorbs from the solid surface to generate products, and the solid catalyst surface recovers to the initial state, thus, completing the solid surface reaction cycle. The surface of the catalysts provides a unique environment that can alter the chemical properties of the reactants and lower the activation energy required for a reaction to occur. Catalysts can be heterogeneous, meaning they are present in a different phase than the reactants (e.g., a solid catalyst in a gas-phase reaction), or they can be homogeneous, meaning they are present in the same phase as the reactants (e.g., a dissolved catalyst in a liquid-phase reaction).

1.1.3 Research of surface catalysts

Surface catalysis is a process in which a catalyst interacts with reactants at the surface of a solid material, accelerating a chemical reaction. Examples of surface catalytic reactions include the oxidation of carbon monoxide (CO) on platinum surfaces, the hydrogenation of vegetable oils on nickel (Ni) surfaces, and the conversion of nitrogen oxides (NOx) in vehicle exhaust on cerium oxide (CeO_2) surfaces [29-31]. Surface catalysis is a complex phenomenon that depends on factors such as the nature of the catalyst, the properties of the reactants, and the reaction conditions. As for the transmission of CO and CO_2, reaction systems closely related to energy and environmental issues, such as catalytic conversion of low-carbon alkanes, catalytic selective oxidation, catalytic hydrogenation, and field coupled energy conversion. Furthermore, the solid surface and interface studies can be cooperated experiment with theoretical calculation, combining with the development and application of new in-situ dynamic research methods, understand the catalytic basis of the target reaction system, reveal the relationship between catalyst structure and performance, and optimize the catalyst structure. At the same time, with the development of measurement techniques, such as nano-scale synthesis methods, atomic layer deposition synthesis methods with controllable catalyst structures, researchers can control the synthesis of catalysts with designed structures and apply them to target catalytic reactions to achieve the research and development of efficient catalytic reactions with corresponding catalytic processes. In gas purification processes, catalysts play a vital role in speeding up chemical reactions and controlling the reaction process. They facilitate the conversion of gaseous pollutants in the gas mixture into harmless substances or useful by-products, making them easier to remove from the gas stream. Catalysis mediated reactions have been successfully applied to purification of sulfur dioxide, nitrogen oxides, automobile exhaust, organic gases, and malodorous substances. And many solid catalytic, such as GaAs, CdS, ZnO, Al_2O_3, and TiO_2, were put forward due to high stability and reactivity [32-34]. To reduce the activation energy of reaction molecules, noble metals participated catalytic reaction have been introduced, such as Ag, Pt, Pd, and Au combined with semiconductor solid catalytic.

In surface catalysis, the reactant molecules adsorb onto the surface of the catalyst, where they are held in place by weak attractive forces such as Van der Waals forces, electrostatic interactions, or hydrogen bonding. Once adsorbed, the reactant molecules can interact with each other in ways that promote the desired chemical reaction. With the development of measurement techniques, researchers observe catalytic reactions in the atomic scale, in other word, interaction of atom with atom can be found. In order to observe reaction processes, X-ray photoelectron spectroscopy (XPS), high resolution

electron energy loss spectroscopy (HREELS) and scanning probe microscopy (SPM) were proposed. XPS was first proposed in 1960s, enabling researchers to measure the energy of strongly bound electrons in molecules. X-rays irradiate the sample, thus stripping the electrons bound by the surface atoms. Because the energies of these electrons are sensitive to local chemical environment, optoelectronic technology can obtain the information of bonding [35]. HREEL was invented in 1970s, which detects the force between atoms in molecules by measuring the energy of molecular vibrations [36]. To further study the detailed surface structure and surface reaction, SPM can be used to measure the surface topography, molecular structures and chemical bonds in atomic or subatomic resolution. Scanning tunneling microscope (STM) technique was invented, which is sensitive to the local electron densities of states closed to the Fermi level. And surface atomic scale information can be obtained by STM. The inventors Gerd K. Bining and Heinrich Rohrer were awarded the Nobel Prize [37, 38].

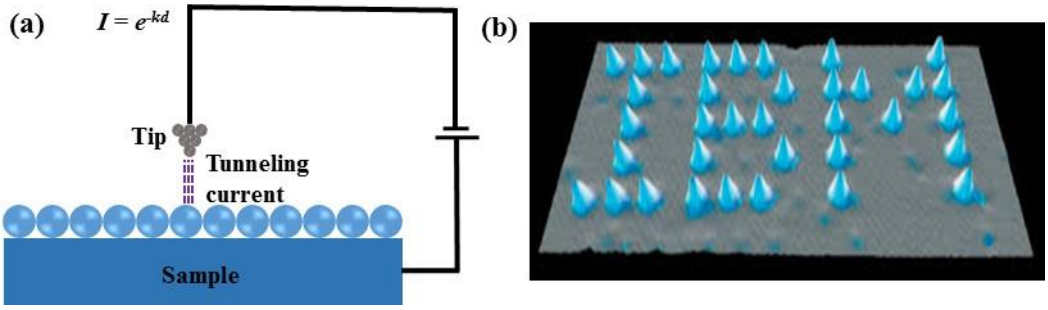

Figure 1.2 Diagram for (a) STM and (b) manipulation of single xenon atoms on nickel surface.

To avoid the tunneling current effect of STM for surface atoms, atomic force microscopy (AFM) was proposed [39]. By detecting the frequency shift of cantilever, the physical properties of surface structure and atoms can be measured. With the further development of instrument technique, the non-contact mode of AFM (NC-AFM) becomes the most widely used method to investigate the nature of surface science [40]. It is a type of AFM that operates in the non-contact mode, where the tip of the AFM probe is brought close to the sample surface without actually making contact with it. Therefore, NC-AFM is a powerful technique for studying the properties of surfaces and interfaces, and has applications in a wide range of fields, including materials science, nanotechnology, and biophysics. It can be used to study the electronic, magnetic, and mechanical properties of surfaces, and can be provided insights into the behavior of atoms and molecules at the nanoscale.

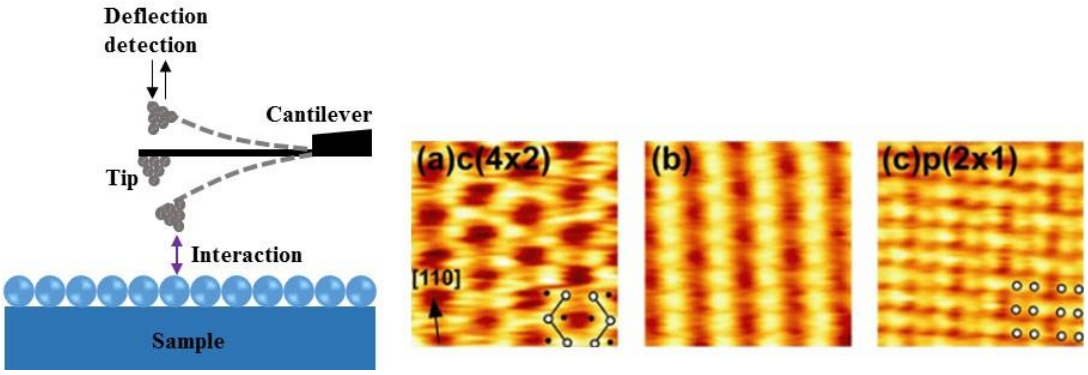

Figure 1.3 Diagram for NC-AFM and observation of the $p(2 \times 1)$ reconstruction of the Si(001) surface [41].

By using the chemical force microscope mode of NC-AFM, local chemical composition analysis of the sample surface can be performed. By scanning the probe on the sample surface and monitoring the charge exchange between the probe and the sample during the scanning process, the surface electrical properties such as charge distribution and electric field distribution can be measured. Observing the arrangement of atoms and molecules, obtaining information about the morphology of the sample surface, investigating the adsorption and movement properties of surface adatoms or molecules are essential for acknowledge the surface catalytic mechanism. Therefore, NC-AFM is used to not only imaging the topography, but also operating adsorptions and chemical interaction bonds.

1.2 Purpose of this research

In this doctoral dissertation, surface adatoms and molecules investigation and operation of the configuration and electronic characteristics in the oxidized TiO_2(110) surface were studied. In detail, surface defect, water, hydroxyl, carbon monoxide and Au properties were investigated by NC-AFM and Kelvin probe force microscopy (KPFM) at 78 K in the home-build ultra-high vacuum condition. The geometric and electronic properties research of surface adsorptions provides effective method to find the mechanism and process of surface catalytic. In homogeneous catalysis, e.g., CO oxidation in catalytic converters, the reactants are adsorbed on the surface of the catalyst and desorbed after reaction from the surface. To reveal the solid surface catalytic characteristic and interaction between adsorbed molecules and surface, we studied the adsorption properties of different molecules on semiconductor catalytic TiO_2(110) surface. Firstly, I introduce the surface defects on the TiO_2(110) surface, which are crucial to the surface state of surface adsorptions. Excess electrons generated from defects migrate on the surface, which can be trapped by surface adsorbates and

lattice atoms. And the active site of surface reactions mainly happens at these locations. Furthermore, the surface defect; oxygen vacancy (O_v) is identified from hydroxyl (OH) by KPFM for the first time. Secondly, I operate the OH and water (H_2O) molecule on the TiO_2(110) surface by applying bias voltage, the adsorption and motion properties of CO molecules are investigated, which can be used to study the catalytic reaction of CO. CO molecules are not stable on the TiO_2(110) surface, and how to move it to an appropriate reaction position is still a challenge. I found that oxygen adatoms (O_{ad}) play an important role for CO adsorption at 78 K. And the unstable state CO can be pinned at the O_{ad} site. Moreover, I was able to move the CO molecules in two-dimensional by using an oxygen modified tip apex. The result of CO motion in two-dimensions on TiO_2(110) surface will be of interest for the CO catalytic reaction at a precise site. Finally, the charge states of Au nanoclusters are clearly identified, which is important to understand the positively charged or negatively charged Au participating the reaction processes of CO oxidation. By using KPFM measurement, I verified that surface and subsurface defects induced polarons and charge redistribution, which makes Au negatively charged. And the diploe moment from Au to the oxygen induces positively charged Au. I found that the negative charged Au nanoclusters are easily desorbed from the surface by operating technique, which indicates negatively charged Au does not stable for catalytic reactions at 78 K. Furthermore, I have successfully performed CO oxidation with oxygen, involving the participation of positively charged Au nanoparticles, for the first time at atomic resolution at 78 K. After reaction, positively charged Au obtain the electrons change into negatively charged.

1.3 Thesis outline

The organization of the dissertation as follows:

■ In chapter 1, research background and importance of surface catalytic in industrial and agricultural life are introduced. Catalytic reaction based on solid semiconductor catalyst is a widely used method to reduce the reaction activation energy. And the adsorbed adatoms properties research on the typical semiconductor catalytic rutile TiO_2(110) surface are still incomplete. The purpose of the dissertation is briefly discussed.

■ In chapter 2, the theory of experimental machine is introduced. Development of SPM techniques has been summarized. I have introduced the emergence and development of STM and the origin of AFM, as well as their current technological applications.

■ In chapter 3, sample preparation and home-build ultrahigh vacuum NC-AFM are proposed. The new sample is fixed with a sandwich structure and is prepared in the

vacuum chamber by sputtering with annealing. Finally, the experimental (110) surface can be obtained.

■ In chapter 4, I talked about the surface defects, such as oxygen vacancy, Ti interstitial, and polarons, which play a crucial role in adsorption properties of the surface reactants. Furthermore, the charge states of Au nanoclusters are influenced by surface and subsurface defects. One of the existing challenges in previous research is the confusion between the surface adsorption of water, hydroxyl, and the presence of surface defects such as oxygen vacancies. This confusion arises because the topographic images of OH and O_v exhibit similar contrast, making it difficult to distinguish between them. To resolve this problem, I combined the AFM with KPFM techniques to systematically identify the difference between H_2O, OH and O_v for the first time. Besides, the operation of H_2O and OH can be realized.

■ In chapter 5, the adsorption and movement properties of CO molecules are investigated, which can be used to study the catalytic reaction of CO. CO molecules are not stable on the TiO_2(110) surface, how to move it to an appropriate reaction position is still a challenge. I found that O_{ad} play important role for CO adsorption at 78 K. And the unstable state CO can be sticked at the O_{ad} site. Moreover, I have achieved the movement operation of CO molecules in two-dimensional by oxygen modified tip apex. The result of CO movement in two-dimensions on TiO_2(110) surface will be of interest for the CO catalytic reaction at a precise site.

■ In chapter 6, the charge states of Au nanoclusters are clearly identified, which is important to understand the positively charged or negatively charged Au participating the reaction processes of CO oxidation. By using KPFM measurement, I verified that surface and subsurface defects induced polarons and charge redistribution, which makes Au negatively charged. And the diploe moment from Au to the oxygen induces positively charged Au. I found that the negatively charged Au nanoclusters are easily desorbed from the surface by operating technique, which indicates negatively charged Au is not stable for catalytic reactions at 78 K. Furthermore, I have successfully performed CO oxidation with oxygen, involving the participation of positively charged Au nanoparticles, for the first time at atomic resolution at 78 K. After reaction, positively charged Au obtain the electrons change into negatively charged.

■ In chapter 7 is the conclusion and outlook for the future research of Au participated reactions based on surface catalysis.

Chapter 2 Theory of scanning probe microscopy

2.1 Introduction

In chapter 2, we present a brief introduction about the theory of SPM. By using SPM technique to image single crystal surfaces and nanoscale systems showing great potential for new scientific progress. The main techniques of SPM include STM, atomic force AFM and KPFM. Three methods can be used to reveal the nature of the surface and the subsurface with atomic resolution. Furthermore, all of these techniques have different advantages. Firstly, I will briefly introduce the STM technique, which is the first testing technology in SPM history. In our experiment, the NC-AFM and KPFM are used to characterize the surface properties.

2.2 Scanning tunneling microscopy

Nanotechnology is truly becoming a scientific field striving to understand, characterize, and control the physical and chemical world in today's surface science. And the detailed atomic resolution to understand physical and chemical processes become more and more important [1-3]. Manipulating and engineering materials at the atomic and molecular level to create new materials and devices with unique properties and functions in surface science research. This has many potential applications in fields such as medicine, electronics, energy, and materials science [4,5]. To reveal the atoms and molecules on the surface, STM has been invented in 1982. In the past decades, the development of STM made great breakthroughs in the field of surface science. And the Nobel Prize was awarded for the surface science analysis and basic physics and chemistry research application of STM technique.

In STM measurement, a small gap exists between the tip and the surface, a sharp metallic tip over the surface and bias voltage is applied between tip and sample, and then electrons tunneling transformation induces current, which is sensitive to the local electron density of state. The Fermi level close to the density of states, so the electrons tunneling current can be used to characterize the surface properties.

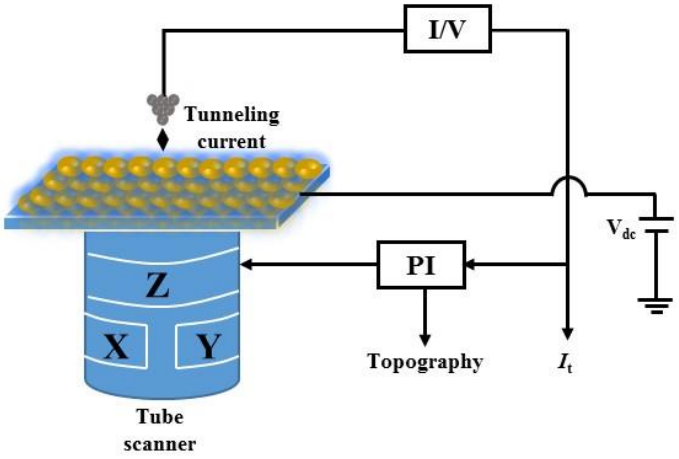

Figure 2.1 Schematic block diagram of scanning tunneling microscopy. The bias voltage is applied to the sample, and tunneling current generates between tip and sample.

The STM tip is made of conducting materials, such as platinum-iridium or tungsten, and tip apex is very sharp with a radius of few atoms. Thus, the STM is able to measure the properties of the surface in atomic resolution. And the basic experimental component is shown in Figure 2.1. STM tip is set close to the sample surface and bias voltage V_{dc} is applied to sample. The electrons get through the vacuum energy state and generate current flow. In this way, by collecting a large tunneling current, the high resolution of surface topography and electronic images can be obtained [6,7].

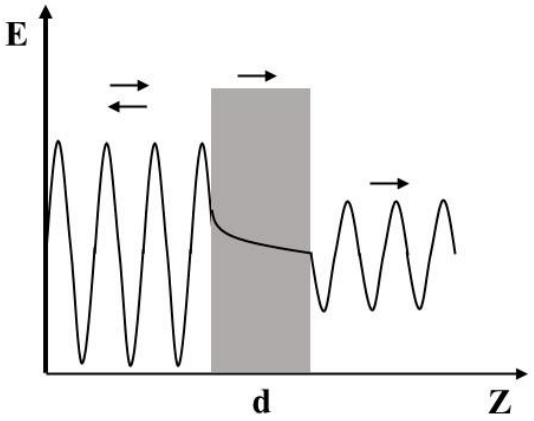

Figure 2.2 Quantum-mechanical of wave function. The tunneling barrier of width *d*. The arrows indicate the reflective, transmission and incident wave direction.

Electron tunneling of two metals depends on the size of the potential barrier between them. Therefore, electrons transfer from one side to another side are considered to be tunneled between these two metal materials. And the potential barrier of electron transmission can be expressed by the Schrödinger equation, as shown below

$$\left[-\frac{\hbar}{2m}\frac{\partial^2}{\partial z^2}+U(\mathrm{z})\right]\psi = E\psi, \qquad (2.2.1)$$

where m is the electron mass, z is the distance between two metal materials, $U(z)$ is the potential barrier, ψ is the wave function and E is the electron energy. When $E > U(\mathrm{z})$, the electrons can overcome the energy barrier and penetrate through the barrier potential generating electron tunneling current. On the contrary, when $E < U(\mathrm{z})$, electrons stay at each side. In the quantum-mechanical of electron tunneling current through a dielectric barrier between two materials that are not in contact. We consider the potential barrier V ($E < V$) as

$$U(\mathrm{z}) = \begin{cases} 0 & (\mathrm{z} < 0, \mathrm{z} > d) \\ V & (0 \le \mathrm{z} \le d) \end{cases}, \tag{2.2.2}$$

taking it into Schrödinger equation, we can get the general solution,

$$\psi_0(\mathrm{z}) = \begin{cases} Ae^{ikz} + Ce^{-ikz} & (z < 0, z > d) \\ B_1 e^{Kz} + B_2 e^{-Kz} & (0 \le z \le d) \end{cases}, \tag{2.2.3}$$

where k and K are the wave factors and can be expressed as

$$k = \sqrt{\frac{2mE}{\hbar^2}}, \tag{2.2.4}$$

$$K = \sqrt{\frac{2m(V-E)}{\hbar^2}}, \tag{2.2.5}$$

which describe the state of electron decaying in the z-direction.

In typical experiments, the sample is biased by positive voltage, and elastic electron tunneling happens from all occupied states of the tip to unoccupied electronic states of the sample. Therefore, the tunneling current depends on the overlap at the same energy between all the electronic wave functions at the tip and all the electronic wave functions of the sample. The tunneling current among all states can be described as

$$I \propto \sum_{E_n = E_F - eV} |\psi_n(0)|^2 e^{-2KW}, \tag{2.2.6}$$

the local density of states (LDOS) is defined at a location z and energy E as

$$\rho_L(z, E) \equiv \frac{1}{\varepsilon} \sum_{E_n = E_F - eV}^{E} |\psi_n(z)|^2, \tag{2.2.7}$$

inserting it to equation (2.2.6), the tunneling current can be written in the manner of LDOS of sample as

$$I \propto V \rho_s(0, E_F) e^{-2KW}. \tag{2.2.8}$$

From the tunneling current by applying bias voltage to the sample, the empty and filled states can be obtained by STM image.

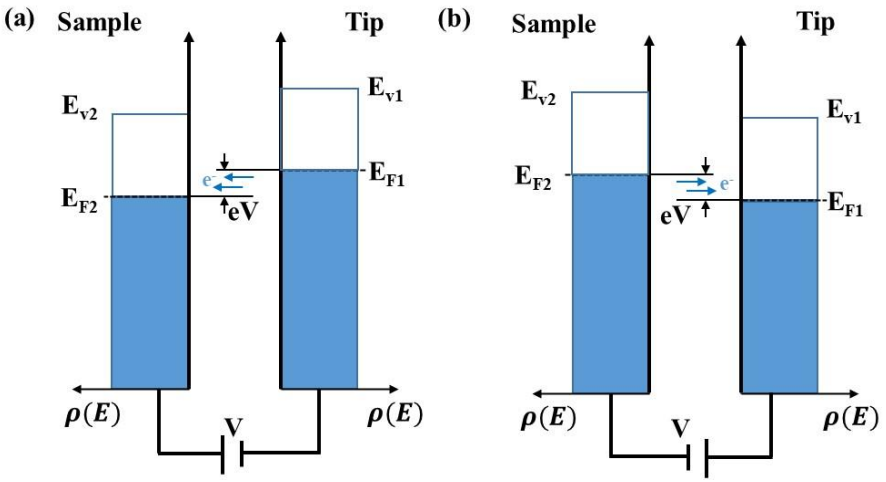

Figure 2.3 Sketch of the tunneling current between electronic states of the sample and the tip. Measurement of (a) empty states and (b) filled states of the sample.

The empty and filled states are displayed with positively and negatively bias voltage. When a positive bias voltage V_{dc} is applied to the sample, the electrons can be transmitted from the filled states of the tip to the empty states in the valance band of the sample. And the tunneling current flows from tip to sample, thus the empty states are imaged. When a negative bias voltage $-V_{dc}$ is applied to the sample, the electrons can be transmitted from the filled states of the sample to the empty states of the tip. In this process, the tunneling current flows from sample to tip, and the integrated density of filled states of below the Fermi level of the sample can be imaged.

2.3 Atomic force microscopy

AFM is a type of scanning probe microscopy that allows imaging and measurement of the topography and physical properties of surfaces at the nanoscale level, which was invented by G. Binning in 1986 (cited in Chapter 1). AFM works by scanning a tiny tip over the surface of a sample, while monitoring the deflection of a cantilever that supports the tip. As the tip scans the surface, it interacts with the atoms and molecules of the sample, causing the cantilever to bend or deflect. This deflection is measured and used to create a three-dimensional map of the surface topography, with high resolution and sensitivity [8-10]. In addition to surface topography, AFM can also measure various physical properties of the sample, such as stiffness, adhesion, electrical conductivity, and magnetic properties. AFM can be operated in air, liquid, or vacuum, and can be used to image both conductive and non-conductive samples [11-14]. It has become an important tool in the field of nanotechnology, enabling researchers to study and manipulate materials at the atomic and molecular scale. This makes AFM a powerful tool for a wide range of applications in materials science, biology, and nanotechnology,

including the study of biomolecules, DNA, and semiconductor devices.

2.3.1 Schematic of atomic force microscopy

In the AFM measurement, the interaction forces between tip of the cantilever and surface of the sample are used, which is reflected from the change of tip oscillation.

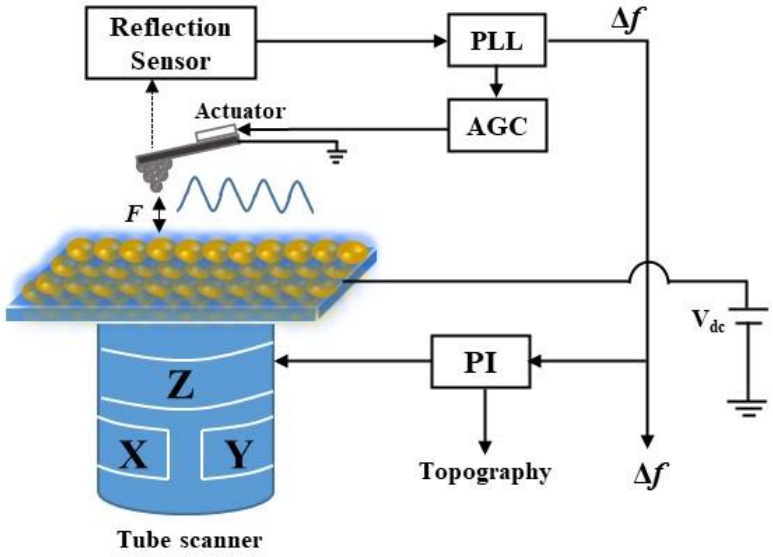

Figure 2.4 Measurement schematic of the atomic force microscopy.

The forces between tip and sample present the key effect. And the forces contributed several factors, long-range van der Waals (vdW) force and electrostatic force, short-range chemical force, which are depended on the range and the strength of the interaction [15]. Based on the operation method, there are three measurement modes, contact mode, tapping mode and noncontact mode. Following is the introduction of these three measurement modes [16].

2.3.2 Scanning modes of atomic force microscopy

There are three types of scanning modes in AFM measurement method.

Since the tip contacts with the surface, namely contact mode. In the contact mode, repulsive force is the main force. The contact mode has the advantage of being relatively simple and fast, making it useful for imaging a wide range of samples. Contact mode is particularly useful for imaging hard or stiff samples, as the tip can penetrate the surface and provide high-resolution images. It is also commonly used in force spectroscopy experiments, which involve measuring the interaction forces between the tip and the sample surface. However, it can also be more destructive than

noncontact mode, as the tip can damage or scratch the sample surface if too much force is applied [17].

In tapping mode, tip taps the surface of the sample at its resonant frequency, and this tapping motion causes the tip to intermittently come into contact with the surface. The amplitude of this tapping motion is kept small to minimize the force between the tip and the sample, which reduces the potential for damage to the sample surface. The interaction forces between the tip and the sample surface cause a change in the frequency and amplitude of the tip's oscillation, and this information is used to create a topographic image of the surface. Tapping mode is particularly useful for imaging soft or delicate samples, as it minimizes the force applied to the surface, reducing the potential for damage. It also provides higher resolution and better contrast than contact mode, making it useful for a wide range of applications, from material science to biology and beyond. Tapping mode is now one of the most commonly used mode in AFM [18].

In noncontact mode, the tip is oscillated, the attractive and repulsive forces between the tip and the sample surface cause a change in the frequency of the tip's oscillation. By measuring this frequency shift, the AFM can create a topographic image of the surface. Noncontact mode is the most commonly used imaging mode in AFM, which is a technique that allows for high-resolution imaging of surfaces at the nanoscale level. In noncontact mode, the AFM tip is oscillated above the surface of the sample, with the tip and the surface separated by a small gap (typically a few nanometers). Noncontact mode is particularly useful for imaging soft or delicate samples that may be damaged by the more forceful contact mode. Noncontact mode also has the advantage of providing information about the chemical composition of the surface, as the frequency shift can be affected by the chemical properties of the sample. This makes noncontact mode useful for a wide range of applications, from material science to biology and beyond. Therefore, the noncontact mode of AFM is used in our experiment [19,20].

2.3.3 Interaction force between tip and sample

The force in noncontact mode is mainly composed of three types of forces. As listed before, van der Waals force, electrostatic force, and chemical force. The total force depends on the oscillation separation between the cantilever and the sample surface. At a separation of z between the cantilever and the surface, the total force acting on the tip apex can be described as:

$$\begin{aligned} F_{\mathrm{ts}}(z) &= F_{\mathrm{vdW}}(z) + F_{\mathrm{es}}(z) + F_{\mathrm{chem}}(z) \\ &= -\frac{\partial}{\partial z}\left[U_{\mathrm{vdW}}(z) + U_{\mathrm{es}}(z) + U_{\mathrm{chem}}(z)\right]. \end{aligned} \tag{2.3.1}$$

The individual contribution of each force is significant, and experiments have shown

that each of them is responsible for the comparison of forces at different positions on the surface. And figure 2.5 shows the deconvolution of the total force between the tip and the surface.

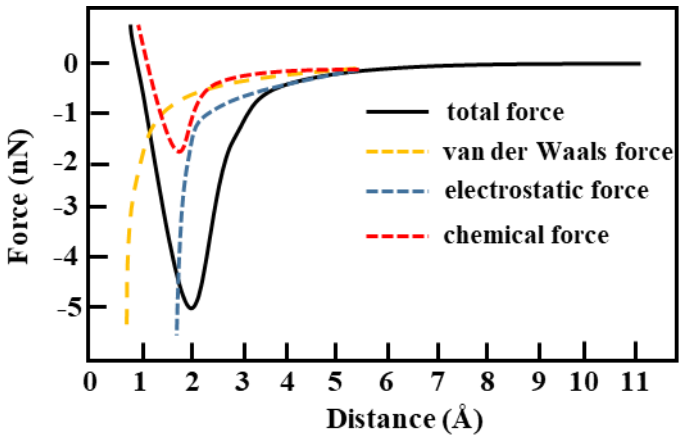

Figure 2.5 Distance dependance of the van der Waals force (yellow), electrostatic force (blue), chemical force (red), and the total force (black).

The van der Waals force is the Coulomb interaction of the atoms, which are induced by electric dipole moment of atoms and the polarization of two matters. We use a sphere-plane model to explain the van der Waals force between the atom of probe and the surface of sample [21].

$$F_{\mathrm{vdW}} = -\frac{2A_H R^3}{3z^2(z+2R)^2}, \tag{2.3.1}$$

where z is the separation distance between the sphere of the probe and the half-space of the surface, R is the radius of the probe, and A_{H} is the Hamaker constant. We consider $z << R$, and get the equation:

$$F_{\mathrm{vdW}} \cong -\frac{A_H R}{6z^2}. \tag{2.3.2}$$

Besides, electrostatic force acts as one of a significant component, owing to the surface charge, should be introduced. Electrostatic forces are attractive or repulsive forces between particles that are caused by their electric charges. This force is also called the Coulomb force or Coulomb interaction and is so named for French physicist Charles-Augustin de Coulomb, who described the force in 1785. The electrostatic force acts over a distance of about one-tenth the diameter of an atomic nucleus or 10^{-16} m. Like charges repel one another, while unlike charges attract one another. For example, two positively charged protons repel each other as do two cations, two negatively charged electrons, or two anions.

In the two-metal surface system, the sum of the difference in work function and applied voltage of the total potential difference within the tip-sample junction as:

$$V_{\mathrm{J}}=V_{\mathrm{B}}+\Delta\,\Phi\,, \tag{2.3.3}$$

where ϕ is the work function at 0 K, and different crystal facets have different values. Considering the potential in the vertical dimension,

$$\Phi = E_F + \frac{q_e}{\varepsilon_0} p_s n_p, \tag{2.3.4}$$

where, E_F is the Fermi level, q_e is the elementary charge, p_s is the surface dipole, and n_p is the cover a surface with an areal density. We consider a geometrically simple arrangement in both tip and surface, which can be regarded as two parallel plates with area A. Here, the electric field between tip and surface is:

$$|\boldsymbol{E}| = E = V_J/z, \tag{2.3.5}$$

then, the potential energy U, stored in the electric field, can be calculated in the form of total work W, as following:

$$-U = W = \frac{\varepsilon_0}{2}\int_V |E|^2 dV = \frac{\varepsilon_0}{2}\left(\frac{V_J}{z}\right)^2 zA = \frac{\varepsilon_0}{2} V_J^2 \frac{A}{z}, \tag{2.3.6}$$

the interaction force between tip and surface would gives the negative gradient of the energy when a purely conservation is considered. Finally, the electrostatic force can be rewritten in z-component [22]:

$$F_{es} = -\frac{dU}{dz} = -\frac{\varepsilon_0}{2} V_J^2 \frac{A}{z^2}. \tag{2.3.7}$$

When the force with a range is less than 1 nm, short-range forces are defined. Then chemical force is generated between tip and surface. And the chemical force includes both attractive force and repulsive force. These are originated from the formation and breaking of the chemical bonds between the atom in tip apex and the surface. Namely, the confinedness of the electronic orbitals limit the interaction range, including the outermost atom of tip-apex and the nearest surface atoms. A simple schematic of chemical force can be described as: in the condition that two atoms are far from each other, the electronic orbitals do not overlap, and chemical force cannot be interacted. With the tip-sample distance decreasing, the valence orbitals are overlapped between the atom from tip and the atom from surface. The molecular bonding and anti-bonding orbital are formed at the same time. And the energy is generated from filling valence electrons into molecular bonding orbitals. This creates an attractive force that drives atoms closer together to a point where the overlap of the valence orbitals, pushing the energy of the bonded molecular orbitals to their lowest energy level, after which the attractive force disappears. The separation distance at which this occurs is also known as the chemical bond length. If the atoms are pushed even closer, repulsive forces between the atoms occur, due to the Pauli Exclusion Principle. The exact strength of the interaction, or the equivalent interaction energy, is difficult to predict as it naturally depends on the chemical properties of the two interacting atoms closely examined. Several approximate methods have been proposed to simulate the distance dependence of chemical interactions as described by Morse potential [23],

$$U_{Morse} = E_{bond}(-2e^{-(z-\sigma)/\lambda} + e^{-2(z-\sigma)/\lambda}), \quad (2.3.8)$$

$$F_{chem} = -\frac{2}{\lambda}E_{bond}\left(e^{-2(z-\sigma)/\lambda} - e^{-k(z-\sigma)/\lambda}\right), \quad (2.3.9)$$

where E_{bond}, σ, λ and z are the chemical bond energy, equilibrium distance, decay length and the distance between two atoms, respectively. When $z >> \sigma$, the initial attractive behavior between the atoms appears. While $z = \sigma$, the interaction force vanishes, and energy reaches a minimum. The second exponential term takes over at $z << \sigma$ and the interaction energy increases resulting in a repulsive force.

Furthermore, we give the minimum AFM detectable force as [24]:

$$\delta F_{min} = \sqrt{2\pi}k\frac{\delta\Delta f_{min}}{f_0}\frac{A^{3/2}}{\lambda^{1/2}}, \quad (2.3.10)$$

where k is the spring constant, f_0 is the resonant frequency of cantilever, A is the oscillation amplitude of cantilever, and λ is the decay length of tip-sample. The $\delta\Delta f_{\text{min}}$ is the minimum detectable frequency shift. Therefore, the force interaction between cantilever and surface is extracted by frequency shift. And the relationship between the oscillation amplitude and frequency shift can be described as:

$$\Delta f = \frac{f_0}{\pi k A^2}\int_{-A}^{A} k_{ts}(z - q'^2)\sqrt{A^2 - q'^2}dq', \quad (2.3.11)$$

where the k_{ts} is the force gradient of tip-sample, q' is the deflection of the cantilever, and z is the tip-sample distance. The integrated section is the weighted average of k_{ts} at one oscillation cycle under the amplitude of A. And the weight w(q', A) is a semicircle with radius divided by the semicircle $\Gamma = \pi A^2/2$.

From the weight function of tip-sample distance with oscillation amplitude, we can get that relatively small oscillation amplitude with small radius induces the interaction force between the tip and the surface in the short-range dominated force. While the weight function increases by increasing the oscillation amplitude, which induces the tip-sample interaction in the long-rang dominated forces. In AFM experiment conditions, the short-range force is used to get atomic resolution imaging. Therefore, the small oscillation amplitude is a preferable choice for nanoscale research.

2.3.4 Working principle of AFM

AFM is a high-resolution scanning probe microscopy technique used to observe the morphology and structure of surfaces. The working principle of AFM is based on the interaction of forces at the nanoscale. AFM utilizes an extremely fine probe, typically a sharp tip, which is connected to a force sensor through a cantilever or spring. The force sensor measures the interaction forces between the probe and the sample. The probe is brought close to the surface of the sample, ensuring a very small distance between the tip of the probe and the sample surface. Typically, this distance is on the order of a few nanometers to allow for the occurrence of interaction forces. As the probe approaches the sample surface, there are interactions between the atoms or molecules

on the sample surface and the tip of the probe. These interactions include adhesive forces, repulsive forces, elastic forces, etc., depending on the properties of the sample surface. The cantilever or spring of the AFM's probe undergoes slight bending or oscillation based on the topographic structure of the sample surface. These variations are transmitted to the control system of the probe through the force sensor. Based on the degree of bending or oscillation of the probe, the control system of the probe can reconstruct the topographic structure of the sample surface and generate an image. By scanning the sample surface, AFM can obtain high-resolution information about the morphology and structure of the sample surface.

It's worth noting that AFM can be operated in air, liquid, or vacuum environments. Additionally, AFM can perform other measurement modes, such as force-distance curve measurement, magnetic measurements, conductivity measurements, etc., to gather more information about the properties of the sample.

As for the formalism of frequency shift Δf and tip-sample interaction force, we need deduce the relationship between oscillation of cantilever and the amplitude with force. Cantilever oscillation can be expressed as:

$$m\frac{d^2z}{dt^2}+\frac{m\omega_0}{Q}\frac{dz}{dt}+kz(t)=kA_{exc}cos\omega t+F_{ts}[z_c+z(t)], \qquad (2.3.12)$$

where m and Q are the effective mass and Q value of the cantilever, k is the spring constant, ω_0 is the intrinsic resonant frequency, ω is the excitation frequency, A_{exc} is the excitation amplitude of cantilever, and z_c is the initial z position of the cantilever. Here, $m = k/\omega_0^2$, substituting into the equation (2.3.12)

$$\frac{d^2z}{dt^2}+\frac{\omega_0}{Q}\frac{dz}{dt}+{\omega_0}^2z(t)={\omega_0}^2A_{exc}cos\omega t+\frac{{\omega_0}^2}{k}F_{ts}[z_c+z(t)], \qquad (2.3.13)$$

the oscillation of the cantilever can be seen as cosine wave, as $z(t) = A\cos(\omega t\text{-}\phi)$. Then, the above equation can be written as:

$$\frac{\omega_0^2-\omega^2}{\omega_0^2}Acos(\omega t-\phi)-\frac{\omega A}{\omega_0 Q}\sin(\omega t-\phi)$$
$$=A_{exc}cos\omega t+\frac{1}{k}F_{ts}[z_c+Acos(\omega t-\phi)], \qquad (2.3.14)$$

to use the orthogonality of the trigonometric function, multiplying $\cos(\omega t\text{-}\phi)$ and integrating with one period $T = 2\pi/\omega$, we will get

$$\frac{\omega_0^2-\omega^2}{\omega_0^2}A\int_{\frac{\phi}{\omega}}^{\frac{2\pi+\phi}{\omega}}cos^2(\omega t-\phi)dt-\frac{\omega A}{\omega_0 Q}\int_{\frac{\phi}{\omega}}^{\frac{2\pi+\phi}{\omega}}\sin(\omega t-\phi)\cos(\omega t-\phi)\,dt$$
$$=A_{exc}\int_{\frac{\phi}{\omega}}^{\frac{2\pi+\phi}{\omega}}\cos\omega t\cos(\omega t-\phi)\,dt$$
$$+\frac{1}{k}\int_{\frac{\phi}{\omega}}^{\frac{2\pi+\phi}{\omega}}F_{ts}[z_c+Acos(\omega t-\phi)]\cos(\omega t-\phi)dt. \qquad (2.3.15)$$

By replacing and integrating with $\theta = \omega t - \phi$ and solving for cosϕ,

$$cos\phi = \frac{\omega_0^2-\omega^2}{\omega_0^2}\frac{A}{A_{exc}} - \frac{1}{\pi k A_{exc}}\int_0^{2\pi} F_{ts}[z_c + Acos\theta]cos\theta d\theta. \quad (2.3.16)$$

In same way, by multiplying sin(ωt - ϕ) to equation (2.3.14), and running integrate with one period T = 2π/ω, we can also obtain

$$sin\phi = \frac{\omega}{\omega_0 Q}\frac{A}{A_{exc}} + \frac{1}{\pi k A_{exc}}\int_0^{2\pi} F_{ts}[z_c + Acos\theta]sin\theta d\theta. \quad (2.3.17)$$

when force interaction is non-functional, sinϕ and cosϕ can be expressed：

$$cos\phi = \frac{\omega_0^2-\omega^2}{\omega_0^2}\frac{A}{A_{exc}}, \quad (2.3.18)$$

$$sin\phi = \frac{\omega}{\omega_0 Q}\frac{A}{A_{exc}}, \quad (2.3.19)$$

according to the characteristics of trigonometric function sinϕ^2 + cosϕ^2 = 1, and replacing with ω to f, ω_0 to f_0 we can get oscillation amplitude A ad tanϕ as:

$$A = \frac{A_{exc}Q}{\sqrt{(1-\frac{f^2}{f_0^2})^2Q^2+\frac{f^2}{f_0^2}}}, \quad (2.3.20)$$

$$tan\phi = \frac{f_0 f}{(f_0^2-f^2)Q}. \quad (2.3.21)$$

When the exited cantilever oscillation frequency equals to the initial resonant frequency $f = f_0$

$$A = A_{\text{exc}}\, Q, \quad (2.3.22)$$

$$\phi = \frac{\pi}{2}, \quad (2.3.23)$$

which indicates that the response signal with 90° phase delay. When $F_{\text{ts}} \neq 0$, the equation (2.3.16) can be described as

$$\frac{\omega_0^2-\omega^2}{\omega_0^2} = \frac{A_{exc}}{A}cos\phi + \frac{1}{\pi k A}\int_0^{2\pi} F_{ts}[z_c + Acos\theta]cos\theta d\theta, \quad (2.3.24)$$

here, we can deduce that

$$\frac{\omega_0^2-\omega^2}{\omega_0^2} = -\frac{\Delta\omega}{\omega_0}\left(1+\frac{\omega}{\omega_0}\right) \approx -2\frac{\Delta\omega}{\omega_0} = -2\frac{\Delta f}{f_0}, \quad (2.3.25)$$

while the Δf can be expressed as

$$\Delta f = -\frac{f_0 A_{exc}}{2A}cos\phi - \frac{f_0}{2\pi k A}\int_0^{2\pi} F_{ts}[z_c + Acos\theta]cos\theta d\theta, \quad (2.3.26)$$

due to the oscillation of cantilever is equal to initial resonant frequency f_0, the cosϕ=0, then

$$\Delta f = -\frac{f_0}{2\pi k A}\int_0^{2\pi} F_{ts}[z_c + Acos\theta]cos\theta d\theta, \quad (2.3.27)$$

by permutation integral with u= cosϕ and $z_c = z + A$, the final relationship between frequency shift of cantilever and interaction force of tip-sample can be derived

$$\Delta f = -\frac{f_0}{2\pi k A}\int_{-1}^{1} F_{ts}[z_c + A(1+u)]\frac{u}{\sqrt{1-u^2}}du. \quad (2.3.28)$$

The conversion of frequency shift and interaction force also can be obtained. Considering the force gradient is not constant due to the dependent of tip-sample distance, regardless the distance dependence of amplitude, Sader-Jarvis put forward a force deconvolution method [25]. The interaction between tip and sample $F_{ts}(z)$ can be obtained. First, $F_{ts}(z)$ is written as an $A(\lambda)$ by Laplace transformation

$$F_{ts}(z) = \int_0^\infty A(\lambda)\exp(-\lambda z)d\lambda, \tag{2.3.29}$$

substituted to equation (2.3.28)

$$\Delta f = -\frac{f_0}{kA}\int_{-1}^{1}\int_{-1}^{\infty} A(\lambda)\exp(-\lambda z - \lambda A(1+u))\ \ \frac{u}{\sqrt{1-u^2}}dzdu, \tag{2.3.30}$$

exchange integral order,

$$\Delta f = -\frac{f_0}{kA}\int_{0}^{\infty}\int_{-1}^{1} A(\lambda)\exp(-\lambda z - \lambda A(1+u))\ \ \frac{u}{\sqrt{1-u^2}}dudz, \tag{2.3.31}$$

Next, we use the Bessel function defined as

$$I_n(z) = \frac{1}{\pi}\int_0^\pi e^{z\cos\theta}\cos(n\theta)d\theta, \tag{2.3.32}$$

when n=1, the equation is

$$I_1(z) = \frac{1}{\pi}\int_0^\pi e^{z\cos\theta}\cos\ \theta d\theta, \tag{2.3.33}$$

where $u = \cos\theta$ and $I_1(z) = -I_1(-z)$,

$$I_1(z) = -\frac{1}{\pi}\int_{-1}^{1} e^{-zu}\frac{u}{\sqrt{1-u^2}}du, \tag{2.3.34}$$

set $T(x) = I_1(x)e^{-x}$,

$$\frac{\Delta f}{f_0} = \frac{1}{kA}\int_0^\infty A(\lambda)T(\lambda A)e^{-\lambda A}dz. \tag{2.3.35}$$

using inverse Laplace transformation, we can get

$$\mathcal{L}[Y(\lambda)] = \int_0^\infty Y(\lambda)\exp(-\lambda z)dz, \tag{2.3.36}$$

Then, given the $A(\lambda)$ as

$$A(\lambda) = \frac{kA}{T(\lambda A)}\mathcal{L}^{-1}[\frac{\Delta f}{f_0}], \tag{2.3.37}$$

the interaction between tip and sample can be deduced as

$$F_{ts}(z) = \mathcal{L}[A(\lambda)], \tag{2.3.38}$$

substituting equation (2.3.37) to equation (2.3.38)

$$F_{ts}(z) = \mathcal{L}[\frac{kA}{T(\lambda A)}\mathcal{L}^{-1}[\frac{\Delta f}{f_0}]], \tag{2.3.39}$$

and the analytical approximation of $T(x)$ is

$$T(x) = \frac{x}{2}(1 + \frac{1}{8}x^{\frac{1}{2}} + \sqrt{\frac{\pi}{2}}x^{\frac{3}{2}})^{-1}, \tag{2.3.40}$$

substitution equation (2.3.40) to (2.3.39)

$$F_{ts}(z) = 2k\left\{\mathcal{L}\left[\lambda^{-1}\mathcal{L}^{-1}\left[\frac{\Delta f}{f_0}\right]\right] + \frac{1}{8}A^{\frac{1}{2}}\mathcal{L}\left[\lambda^{-\frac{1}{2}}\mathcal{L}^{-1}\left[\frac{\Delta f}{f_0}\right]\right] + \sqrt{\frac{\pi}{2}}x^{\frac{3}{2}}\mathcal{L}[\lambda^{\frac{1}{2}}\mathcal{L}^{-1}\left[\frac{\Delta f}{f_0}\right]]\right\}, \quad (2.3.41)$$

where the $\mathcal{L}^{-1}[\Delta f/f_0]$ is a function of λ, and the using next equations

$$\mathcal{L}[\lambda^{-\alpha}Y(\lambda)] = I^{\alpha}\mathcal{L}[Y(\lambda)], \quad (2.3.42)$$

$$\mathcal{L}[\lambda^{\alpha}Y(\lambda)] = D^{\alpha}\mathcal{L}[Y(\lambda)], \quad (2.3.43)$$

$$I^{\alpha}\varphi(\lambda) = \frac{1}{\Gamma(\alpha)}\int_{\lambda}^{\infty}\frac{\varphi(t)}{(t-\lambda)^{1-\alpha}}dt, \quad (2.3.44)$$

$$D^{\alpha}\varphi(\lambda) = \frac{-1}{\Gamma(1-\alpha)}\frac{d}{d\lambda}\int_{\lambda}^{\infty}\frac{\varphi(t)}{(t-\lambda)^{\alpha}}dt, \quad (2.3.45)$$

substituting equations (2.3.42), (2.3.43), (2.3.44) and (2.3.45) to (2.3.41)

$$F_{ts}(z) = 2k\int_{z}^{\infty}\left[\left(1 + \frac{A^{\frac{1}{2}}}{8\sqrt{\pi(t-z)}}\right)\Omega(t) - \frac{A^{\frac{3}{2}}}{\sqrt{2(t-z)}}\frac{d\Omega(t)}{dt}\right]dt, \quad (2.3.46)$$

here, $\Delta f/f_0 = \Omega(t)$. In this way, the interaction force $F_{ts}(z)$ between tip and sample can be derived by frequency shift Δf with feature of FM-AFM mode. The small amplitude approximation is contributed at the first term of the equation, and the large amplitude approximation is contributed at the second term of the equation. Then, the interaction potential $U_{ts}(z)$ is described as

$$U_{ts}(z) = 2k\int_{z}^{\infty}\Omega(t)\left((t-z) + \frac{A^{\frac{1}{2}}}{4}\sqrt{\frac{t-z}{\pi}} + \frac{A^{\frac{3}{2}}}{\sqrt{2(t-z)}}\right)dt, \quad (2.3.47)$$

Finally, equation (2.3.47) satisfying

$$F_{ts}(z) = -\frac{dU_{ts}(z)}{dz}. \quad (2.3.48)$$

2.3.5 Noise in the AFM system

In the measurement of Non-contact FM-AFM, to realize the stable super-high resolution, noise coming from system, electric circuits and environment needs to be resolved. Following, we will analyze the noise in the AFM system.

The frequency shift noise coming from the variation of the vertical oscillation, which is given by the radio from the noise in imaging signal and the slope with respect to the tip-sample distance z [20]

$$\delta z_f = \frac{\delta\Delta f}{|\partial f/\partial d|}, \quad (2.3.49)$$

here, to decrease the oscillation amplitude and spring constant of cantilever to increase signal-to-noise ratio. Thermal noise is effect on the cantilever oscillation and frequency shift. We can directly measure the thermal noise from frequency shift

$$\delta f_{thermal} = \sqrt{\frac{f_0 k_B T B}{\pi k_{cant} A^2 Q}}, \quad (2.3.50)$$

where f_0 is the resonance frequency, k_B is Boltzmann constant, T is the temperature, B is the detection bandwidth, k_{cant} is the spring constant, A is the oscillation amplitude, and Q is the Q-value [26-28]. Besides, the frequency shift noise coming from detection noise can be described as

$$\Delta f_{detec} = \frac{n}{\pi A} B^{\frac{3}{2}};\ n = \frac{\delta z_{cant}}{\sqrt{B}}. \tag{2.3.51}$$

where n and δz are the noise density and the noise in the cantilever oscillation signal, respectively. The difference between equation (2.3.51) and equation (2.3.51) is the dependence on B. For the detection noise, the frequency noise is scaled by $B^{3/2}$, and the detection noise is the main contributing factor. This makes B a critical parameter in NC-AFM measurements.

Oscillator noise is another measurement noise induced by a driving of the cantilever [29]. This noise is proportional to finite n_q and inversely proportional to Q:

$$\frac{\delta f_{osc}}{f_0} = \frac{n_q B^{1/2}}{\sqrt{2} A Q}, \tag{2.3.52}$$

similar with thermal noise, oscillator noise is dependence on the square root of the detection bandwidth B, and inversely to oscillation amplitude.

Besides, frequency drifts noise caused by thermal effect need also considering. The noise parameters dependent on the drift rate of the frequency r and measurement period τ. The force gradient measurement bases on this noise is given:

$$n_{k-drif}(f_{mod}) = \frac{2kr\sqrt{\tau}}{f_0 \pi f_{mod}}, \tag{2.3.53}$$

as we can see, frequency drift rate if proportional to f_0, and the thermal drift is proportional to the stiffness k. The absolute force gradient noise can be deduced by transformed in density representation:

$$n_{k-drif}(f_{mod}) = \sqrt{\frac{\partial \delta k^2}{\partial B}|_{B=f_{mod}}}, \tag{2.3.54}$$

The total noise of force gradient is

$$n_k^2(f_{mod}) = n_{k-det}^2(f_{mod}) + n_{k-th}^2 + n_{k-osc}^2 + n_{k-drif}^2(f_{mod}), \tag{2.3.55}$$

When the stiffness of cantilever is less than a specific value, tip is easily jumped to contact to the surface during approaching. Therefore, stable oscillation condition is necessary to be find. We use the larger spring constant k of cantilever to avoid the jumping of the tip, and the k needs to be met [30,31]:

$$k > max\left(-\frac{\partial F_{ts}}{\partial z}\right) = k_{ts}^{max}, \tag{2.3.56}$$

for the tip oscillating in large enough amplitude A, the jump-to-contact of the tip can be avoided:

$$kA > -F_{ts}^{max}. \tag{2.3.57}$$

In this condition, the restoring force is larger than the maximum attractive force. And

the damping of cantilever of internal dissipation and energy loss per cycle is:

$$\Delta E_{loss} = 2\pi \frac{E}{Q}, \tag{2.3.58}$$

where E is the energy of oscillated cantilever with $kA^2/2$. Usually, the phase difference of cantilever and driving signal have delaying with π/2, then from $A_{drive} = Ae^{i\pi}/Q$, we can get that

$$|A_{drive}| = |A| \frac{\Delta E_{loss}}{2\pi E}, \tag{2.3.59}$$

When tip approaches to the surface, the interaction force between the tip and the sample is generated. An additional damping force is considered into equation (2.3.58)

$$|A'_{drive}| = |A| \frac{\Delta E_{loss} + \Delta E_{ts}}{2\pi E} = |A|(\frac{1}{Q} + \frac{\Delta E_{ts}}{2\pi E}), \tag{2.3.60}$$

to keep a constant value of oscillator circuit, Q value need much larger than $2\pi E/\Delta E_{ts}$. Therefore, the relationship of A and k is given by [32]

$$\frac{kA^2}{2} \geq \Delta E_{ts} \frac{Q}{2\pi}. \tag{2.3.61}$$

Hence, a large oscillation amplitude or a high spring constant of cantilever should be used to achieve the stable oscillation condition.

2.4 Kelvin probe force microscopy

KPFM is a technique used in nanoscale imaging and characterization of surfaces. KPFM combines AFM with Kelvin probe measurements to study the local surface potential and work function of materials. In KPFM, a conductive probe with a sharp tip is scanned across the sample surface, while a small AC voltage is applied between the tip and the sample. The resulting electrostatic force between the tip and the sample modulates the amplitude of the AC voltage. By measuring this modulation, the local surface potential or work function variations can be mapped. KPFM is widely used in various fields such as materials science, semiconductor research, and surface analysis. It provides valuable information about the electrical properties and surface potential distribution of materials at the nanoscale [33].

2.4.1 Principle of KPFM

To understand the principle of KPFM, let's first introduce the work function [34-39]. The work function is the minimum energy required to remove an electron from the Fermi level of a material to a point just outside the material's surface. It represents the energy barrier for electron emission and is a fundamental property of a material's surface.

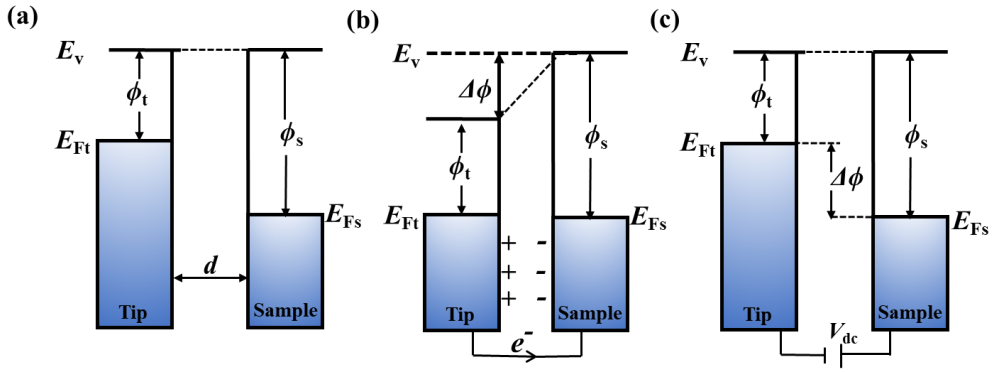

Figure 2.6 A schematic energy diagram of the relationship between the metallic tip and a metallic sample in terms of their work functions and Fermi levels. (a) In the case of two isolated metals with work functions ϕ_t and ϕ_s, the vacuum level E_v is the same for both, while their Fermi levels are different. (b) Two materials come into electrical contact, the Fermi levels align through the exchange of electric charge. Alignment results in the accumulation of surface charges, creating an electric field and leading to a voltage drop of $V_{CPD} = \Delta\phi/e$ across the vacuum gap. (c) By applying a bias voltage of $V = V_{CPD}$, it is possible to compensate for the contact potential difference and achieve a balance between the tip and sample.

As briefly described in Figure 2.6, when two bodies with different Fermi energies come into contact, the electrons redistribute to establish a new joint Fermi level. Electrons from the material with the higher Fermi energy tend to flow towards the material with the lower Fermi energy. This redistribution of electrons enables the establishment of equilibrium and the alignment of Fermi levels between the two bodies. Since the nuclei are fixed, the interaction between two bodies with different Fermi energies leads to the emergence of a contact potential difference (CPD) in electron volts (eV), which in turn contributes attractively to the overall force. In the context of NC-AFM, this additional contribution to the measured frequency shift is generally undesired as it can strongly affect topographic imaging. The CPD contribution to the measured frequency shift can be obtained from the force expression:

$$\Delta f_{CPD} = -\frac{f_0}{2k}\frac{\partial}{\partial z}\left(\frac{1}{2}\frac{\partial}{\partial z}(U_{CPD} - U_{bias})^2\right)$$

$$= -\frac{f_0}{4k}\frac{\partial^2 C}{\partial z^2}(U_{CPD} - U_{bias})^2, \qquad (2.4.1)$$

where f_0 and k are the free resonance frequency and spring constant of cantilever, C is the capacitance between the cantilever and the surface, U_{CPD} is the contact potential difference, and U_{bias} is the applied bias voltage. As indicated by Equation (4.20), the additional frequency shift resulting from the CPD is directly related to the square of the difference between the applied bias voltage (U_{bias}) and the CPD value. When U_{bias} = -

U_{CPD}, the additional frequency shift becomes zero, while for other applied bias voltages, it is negative. This characteristic is utilized to determine the magnitude of -U_{CPD} by sweeping the applied U_{bias} and measuring the resulting frequency shift at a fixed point above the surface. Figure 2.7 presents data obtained from such a measurement, where U_{bias} was swept from -2 to 3 V.

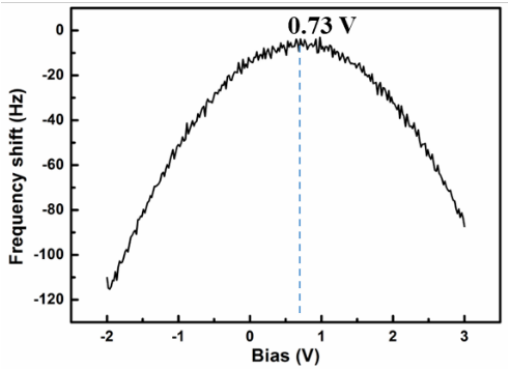

Figure 2.7 The experimentally recorded spectroscopy curve exhibits a parabolic relationship between the frequency shift and the bias voltage. The voltage at the peak of the parabola is recognized as the contact potential difference.

The recorded frequency shift curve exhibits a parabolic shape, reflecting the squared dependence on U_{bias}. The vertex of the parabola corresponds to -U_{CPD}. This allows the determination of the specific U_{bias} value that cancels out the effect of the CPD before acquiring topographic images of the surface. It is important to note that this approach is applicable only to electrically homogeneous metallic and semiconducting surfaces. In the case of insulators, where electrons are not free to move, the concept of Fermi energy is not well-defined, and this method cannot be employed. However, there still be a non-zero bias voltage at the electrostatic forces are cancelled out from surface charging effects. Complex and electrically inhomogeneous systems, such as metal nanoparticles deposited on a single crystal surface, may exhibit additional local contributions to the intrinsic potential difference between the tip and the surface. This contribution can be represented by introducing a term known as the local contact potential difference (LCPD) in units of electron volts,

$$\Delta f_{CPD} \propto -(U_{LCPD} - U_{bias})^2, \tag{2.4.2}$$

$$U_{LCPD} = U_{CPD} + U_{add}(x, y, z). \tag{2.4.3}$$

here, all additional contributions to the intrinsic CPD between the tip and the sample are accounted for by the term U_{add}. U_{add} can be a non-local function of the (x, y) position of the tip over the surface, as well as the tip-sample separation height (z). The z dependence arises from the fact that U_{add} represents a local electrostatic effect that becomes noticeable only at small separation distances, as it gets averaged out at larger distances. The specific composition of U_{LCPD}, which includes U_{add}, needs to be

evaluated for each individual system. It is important to note that U_{LCPD} is generally not a constant value across the entire surface. This means that the conventional method of determining the required bias voltage (U_{bias}) to cancel out U_{LCPD} is no longer applicable. Instead, a new technique called KPFM must be employed. The KPFM method, derived from Lord Kelvin's original experimental technique introduced in 1897, allows for the detection of electrostatic forces on a microscopic scale [40]. Lord Kelvin observed the deflection of a Volta condenser, consisting of two different metals (copper and zinc), caused by the formation and breaking of electrical contact between them. The modern version of this setup, the Kelvin Probe Force Microscope, is more advanced but operates based on the same fundamental principles. It utilizes the intrinsic CPD between materials with different work functions when they are in electrical contact.

The modern KPFM technique involves the application of a modulating AC bias voltage ($U_{mod} = U_{AC} \times \sin(2\pi f_{mod} t)$) in addition to the DC bias voltage (U_{DC}) between the surface and the oscillating tip-cantilever system. When only the capacitance has a non-zero gradient, the resulting electrostatic force between the tip and the sample can be expressed as follows:

$$F_{el} = \frac{1}{2}\frac{\partial C}{\partial z}(U_{LCPD} - U_{DC} - U_{AC}(2\pi f_{mod} t))^2, \tag{2.4.4}$$

$$F_{el} = F_{DC} + F_{f_{mod}} + F_{2f_{mod}}, \tag{2.4.5}$$

where

$$F_{DC} = \frac{1}{2}\frac{\partial C}{\partial z}\left((U_{LCPD} - U_{DC})^2 + \frac{1}{2}U_{AC}^2\right), \tag{2.4.6}$$

$$F_{f_{mod}} = -\frac{\partial C}{\partial z}(U_{LCPD} - U_{DC})U_{AC}\sin(2\pi f_{mod} t), \tag{2.4.7}$$

$$F_{2f_{mod}} = \frac{\partial C}{4\partial z}U_{AC}^2\sin(4\pi f_{mod} t). \tag{2.4.8}$$

There are three distinctive contributions to the electrostatic force between the tip and the surface: F_{DC} (a constant DC term), F_{fmod} (a term oscillating at frequency f_{mod}), and F_{2fmod} (a term oscillating at frequency $2f_{mod}$). Based on equations (2.4.6)-(2.4.8), there are two approaches to adjusting the U_{DC} (applied DC bias voltage) to precisely cancel out U_{LCPD}. In both methods, the U_{DC} applied to the surface can be measured, allowing for a local contact potential measurement ($U_{DC} = -U_{LCPD}$). Additionally, it enables the acquisition of accurate topographical images of the surface, which find applications in various fields such as semiconductor physics, photocatalysis, and more.

2.4.2 Minimum detectable CPD of KPFM

Due to the AFM is mainly used in FM-AFM mode, our KPFM also use frequency modulation mode (FM-KPFM). The KPFM frequency modulation mode is based on

detecting the electrostatic force gradient. The expression for the electrostatic force in equations (2.4.6) to (2.4.8) has an impact on the frequency shift of the tip-cantilever system, introducing modulation at frequencies f_{mod} and $2f_{\mathrm{mod}}$. By employing the small amplitude approximation, the frequency shift resulting from the electrostatic forces can be expressed as follows:

$$\Delta f_{EL} = -\frac{1}{2}\frac{f_0}{k}\frac{\partial}{\partial z}(F_{DC} + F_{f_{mod}} + F_{2f_{mod}}) = \Delta f_{DC} + \Delta f_{f_{mod}} + \Delta f_{2f_{mod}}, \quad (2.4.9)$$

and

$$\Delta f_{DC} = -\frac{1}{4}\frac{f_0}{k}\frac{\partial^2 C}{\partial z^2}\left((U_{LCPD} - U_{DC})^2 + \frac{1}{2}U_{AC}^2\right), \quad (2.4.10)$$

$$\Delta f_{f_{mod}} = \frac{1}{2}\frac{f_0}{k}\frac{\partial^2 C}{\partial z^2}(U_{LCPD} - U_{DC})U_{AC}\cos(2\pi f_{mod}t), \quad (2.4.11)$$

$$\Delta f_{2f_{mod}} = -\frac{1}{8}\frac{f_0}{k}\frac{\partial^2 C}{\partial z^2}U_{AC}^2\cos(4\pi f_{mod}t), \quad (2.4.12)$$

The contributions of $\Delta f_{f\mathrm{mod}}$ and $\Delta f_{2f\mathrm{mod}}$ to the overall frequency shift manifest as sidebands at $f \pm f_{\mathrm{mod}}$ and $f \pm 2f_{\mathrm{mod}}$, respectively. In the frequency spectrum of the cantilever oscillation signal, using a lock-in amplifier (LIA), it is possible to measure the signal at $f \pm f_{\mathrm{mod}}$, which can be nullified by adjusting U_{DC}. At $U_{\mathrm{DC}} = -U_{\mathrm{LCPD}}$, there remains a DC contribution from the electrostatic forces, which is undesirable for the reasons explained in the previous section. The KPFM FM-mode offers several advantages compared to the KPFM AM-mode. In the FM-mode, the measurement of U_{LCPD} is proportional to $\partial^2 C/\partial z^2$, whereas in the AM-mode it is proportional to $\partial C/\partial z$. This theoretically gives the FM-mode higher spatial resolution. Additionally, since the FM-mode operates with significantly smaller f_{mod} (typically ~300 Hz), high resonance frequency cantilevers can be used without exceeding the bandwidth of the detection electronics, resulting in improved topography resolution. However, there are also disadvantages to using the FM-mode. Unlike the AM-mode, which benefits from resonance enhancement at overtone frequencies, the FM-mode does not rely on detecting oscillation amplitude. As a result, the signal-to-noise ratio (S/N) is reduced by a factor of approximately Q (~10000). This means that a larger modulation frequency amplitude (U_{AC}) needs to be applied to achieve an adequate S/N, which can potentially lead to undesired effects.

Chapter 3 Sample and equipment of low temperature ultrahigh vacuum AFM/KPFM

3.1 Introduction

In chapter 3, we will introduce the sample with its preparation method in this study. A rutile TiO_2(110)-1×1 (provided by Crystal Base Corporation) crystal was used. Firstly, we illustrate the fixation of the sample, and then, we introduce the sample preparation in ultrahigh vacuum condition. Finally, the experimental instrument and methods are introduced.

3.2 TiO_2 crystal

Titanium dioxide (TiO_2) is a naturally occurring oxide of titanium. It is a widely used material due to its various properties and applications [1]. TiO_2 is commonly found in the form of a white pigment and is extensively utilized in industries such as paints, coatings, plastics, ceramics, and cosmetics. It is also employed in photovoltaic cells, catalysts, sensors, and medical implants, among other fields. TiO_2 is known for its high refractive index, UV-blocking capabilities, photocatalytic properties, and stability, making it a versatile and valuable material in numerous industries. The crystal configuration of TiO_2 is shown in below.

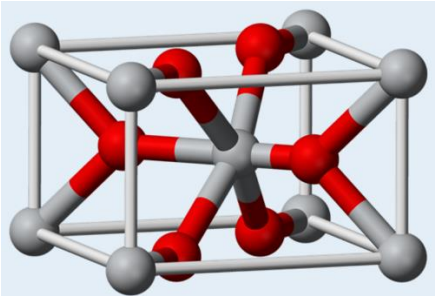

Figure 3.1 Ball-and-stick model of rutile TiO_2.

The structure of rutile TiO_2 is shown in Figure 3.1. In rutile TiO_2, the titanium dioxide crystal adopts a tetragonal crystal structure. Each titanium atom is surrounded by six oxygen atoms, forming an octahedral coordination. The oxygen atoms are positioned at the corners of the octahedron, while the titanium atom resides at the center. The bond lengths between the titanium and oxygen atoms in rutile TiO_2 are relatively equal [2].

Rutile TiO_2(110) is one of the most important materials in the catalytic studies. Because the polished single-crystal sample of high quality are widely available and not expensive, besides, the preparation of sample in ultra-high vacuum (UHV) can be easily achieved by gas sputtering in situ cycles and following annealing. Titanium dioxide has three forms of allotropy in nature, brookite, anatase, and rutile. In order to obtain the energy for free radical activation, the band gap of catalysis needs larger than 2.8 eV. Furthermore, considering the catalytic activity and stability, the most investigated crystal phase is rutile TiO_2 due to the band gap of 3.02 eV, which is beneficial for reducing the recombination of electrons and holes and increasing reaction activity [3].

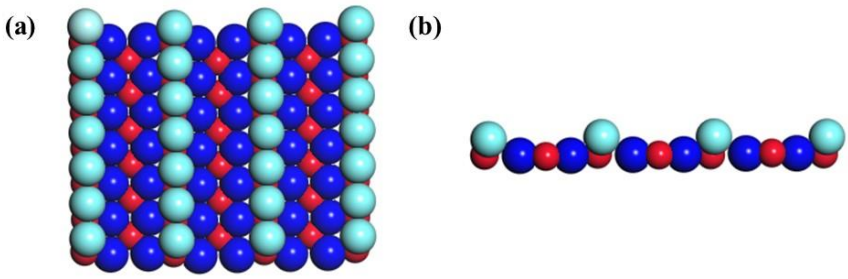

Figure 3.2 Ball model of rutile TiO_2(110)-1×1 surface. (a) Top and (b) side view of single layer.

Figure 3.1 shows the unit structure of the rutile titanium dioxide. In the configuration of TiO_2(110)-1×1 surface. The structure of the prepared surface is accurately known from the quantitative techniques investigation, and the results are well agreed with the discrete Fourier transform (DFT) calculations [4-6]. The titanium atom is surrounded by six oxygen atoms in an octahedral configuration. And the bond between titanium and oxygen atoms at the planer of the octahedron are a little shorter. At TiO_2(110) surface, it is mainly composed by three-fold coordinated oxygen atoms (O_{3c}, dark blue balls), two-fold coordinated oxygen atoms (O_{2c}, bright blue balls) and five-fold coordinated titanium atoms (Ti_{5c}, red balls).

The crystal structure exhibits a close-packed arrangement of oxygen atoms in the (001) planes, with the titanium atoms occupying the spaces between them. This results in a layered structure with alternating layers of titanium and oxygen atoms. The rutile configuration is characterized by its distinct lattice parameters and atomic arrangement, giving rise to its unique properties and applications. Researchers Ramamoorthy and Vanderbilt conducted calculations using an ab initio method to determine the total energy of a periodic TiO_2 slab. They discovered that the (110) surface has the lowest surface energy, while the (001) surface has the highest energy [7,8]. Notably, the rutile phase is the most abundant form.

Furthermore, at lower temperatures, TiO_2 exists in the anatase phase, which has a tetragonal crystal structure. In the anatase structure, the titanium atoms are surrounded

by six oxygen atoms, forming octahedral coordination. However, the arrangement of atoms in the crystal lattice is different, resulting in distinct properties. Upon heating to temperatures typically between 600°C-800°C, an irreversible phase transition occurs, and anatase transforms into rutile [9,10]. Rutile has a different crystal structure, belonging to the tetragonal crystal system. In rutile, the titanium atoms are still coordinated with six oxygen atoms in an octahedral configuration, but the atomic arrangement and lattice parameters differ from anatase. The transformation from anatase to rutile is accompanied by changes in crystal symmetry, lattice parameters, and other physical properties [11,12]. It is influenced by factors such as temperature, pressure, and doping. The transformation process is of interest due to the different properties exhibited by anatase and rutile phases, which can impact their various applications in fields such as catalysis, solar cells, and photocatalysis.

3.3 Point defects in the rutile TiO_2 crystal

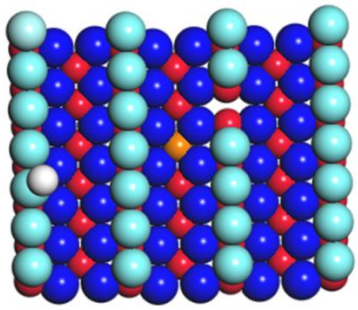

Figure 3.3 The ball model of the rutile TiO_2(110)-(1×1) surface with the surface and subsurface defects. Bright blue balls, O_{2c}; blue balls, O_{3c}; red balls, Ti; white balls, H of hydroxyl, orange ball, Ti interstitial atom.

Defects play a crucial role in transforming rutile TiO_2 from an insulator to a n-type semiconductor. Surface defects, such as oxygen vacancies and hydroxyl groups, can be introduced on the rutile TiO_2(110)-(1×1) surface [13-15]. The formation of oxygen vacancies involves removing an oxygen atom from the bridging two-fold coordinated oxygen rows, while hydroxyl groups are formed by the dissociation of water molecules on the five-fold coordinated Ti rows. Interstitial defects in rutile TiO_2 can occur due to the presence of Ti interstitial atoms. These defects involve the insertion of additional Ti atoms into the crystal lattice at sites between the regular Ti atoms. Ti interstitial atoms can have a significant impact on the material's properties. They can introduce extra electrons into the system, making the material more conductive and altering its electronic behavior. The presence of Ti interstitials can also affect the material's optical and catalytic properties. The formation of Ti interstitial defects can be influenced by

various factors, such as temperature, pressure, and growth conditions. The exact distribution and behavior of these defects depend on the specific crystal structure and the presence of other defects or impurities in the material. Experimental and theoretical studies are conducted to investigate the role of Ti interstitial defects in rutile TiO_2, aiming to understand their impact on the material's properties and their potential applications in various fields, including catalysis and electronic devices.

These defects serve as excess electron reservoirs for catalytic reactions. One hydroxyl defect provides one excess electron, one oxygen vacancy provides two electrons, and one Ti interstitial atom provides four excess electrons [16,17]. Numerous experimental studies, combined with theoretical calculations, have been conducted to investigate the morphological and electronic properties of these defects, as well as the distribution of electrons around them. These investigations help understand the role of defects in the electronic behavior and catalytic activity of rutile TiO_2.

Besides, the excess electrons in the TiO_2 bonding with surrounding lattice lead to polarons to the surface defects. When a bridging oxygen vacancy is created by removing a neutral oxygen atom from the rutile TiO_2 surface, two electrons are left behind due to the breaking of two Ti-Ti bonds. The preferred arrangement of the resulting polaron is known based on the specific location of the vacancies. The consensus from theoretical calculations suggests that the polaron localizes on the second layer of Ti atoms near the oxygen vacancies. Additionally, the relatively positive oxygen vacancy acts as a bonding site for the two polarons. Experimental observations using SPM technique have revealed that the polaron not only bonds to the oxygen vacancy but also exhibits mobility across four specific sites. This mobility is more pronounced at higher temperatures, with complete stabilization occurring around 5K and increased movement beyond 78 K. Similar models can be applied to hydroxyl vacancies, although the presence of a singly positively charged hydrogen atom reduces the number of polarons to one. These polarons play a role in inducing specific local chemical interactions on the surface. For example, adsorbed CO molecules exhibit attractive coupling with polarons in the surface layer and repulsive interactions with polarons in the subsurface layer of the rutile TiO_2 surface.

3.4 Sample preparation

3.4.1 Fixation of sample

First, we will introduce the sample fixing, which is important for sample annealing. In our experiment, we use the Crystal Base Corporation provided rutile TiO_2(110) sample with a rectangle of 10 nm × 2.5 nm and a width of 0.5 nm. The sample is fixed

in sandwich structure, as shown in below:

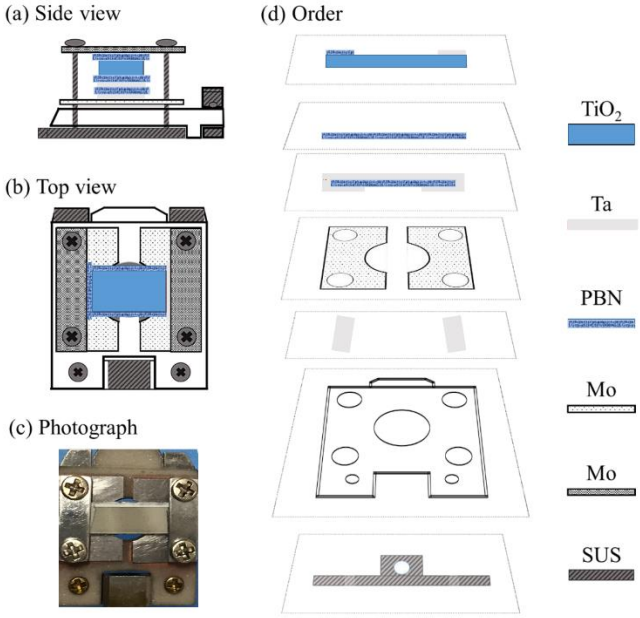

Figure 3.4 Schematic diagram of sample fixation method in sandwich structure.

The physical material property of bulk rutile TiO_2 can be considered as wide band-gap semiconductor with a resistance dependence on the surface oxygen defects. Thus, it is difficult to directly use electric annealing, and the oxygen defects on the surface can lead to fluctuations in the current owing to the oxygen vacancies can introduce localized states within the material's bandgap. These localized states can act as traps for charge carriers, affecting the flow of current. We use the indirect method to heat and annealing to make surface generated atomic structure. To apply a bias voltage to the sample, two electrodes are connected to the bottom of the sample holder. These electrodes serve as the electrical contacts for the sample. They enable the application of a voltage across the sample, which can influence its electrical properties. In addition, a metal tantalum (Ta) foil with a thickness of 0.1 mm is employed as a heater in the setup. The Ta foil is responsible for generating heat and controlling the temperature of the sample. By supplying electrical current to the tantalum foil, it heats up and transfers thermal energy to the sample, allowing for precise temperature control during the experiment. Besides, the insulator pyrolytic boron nitride (PBN) is sandwiched by Ta foil to avoid the deformation of Ta foil. PBN is covered on the sandwich structure to make temperature changes gradually. To establish electrical contact between the tip and the TiO_2 sample, a small cut PBN sheet and a Ta film are placed between the metal plate and the TiO_2 sample. In general, The PBN sheet acts as an insulating layer to prevent electrical contact between the metal plate and the TiO_2 sample, except through the designated area where the cut is made. This ensures that the current flow is directed through the desired pathway. The Ta film, on the other hand, facilitates electrical contact

between the metal plate and the TiO_2 sample. It acts as a conductive bridge, allowing the current to flow from the tip to the TiO_2 sample and then to the backside metal plate.

3.4.2 Sample preparation

A rutile TiO_2(110)-1×1 sample is transferred to ultrahigh vacuum chamber to clean and generate atomic structure. Usually, repeated Ar (argon) ion sputtering and high temperature annealing are operated on the surface. The schematic of sample preparation is shown in Figure 3.5.

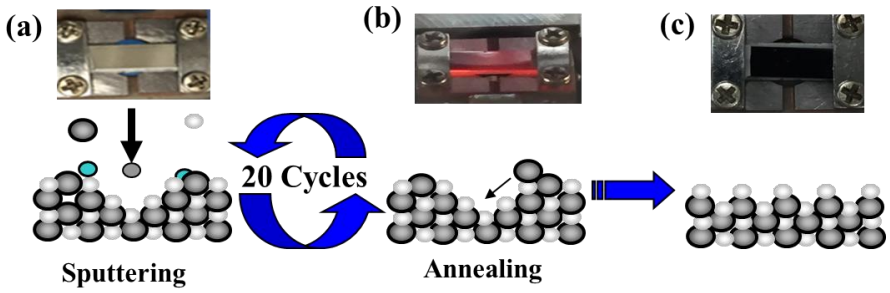

Figure 3.5 Schematic processes of sample preparation.

The new rutile TiO_2(110)-(1×1) surface (shown in white color) is initially treated by Ar ion sputtering using an ion gun. During the sputtering process, an emission current of approximately 20 μA and an ion energy of about 1 keV are used. The vacuum condition is maintained at a pressure of 5.0×10^{-7} Torr with a duration of 15 minutes. After the Ar ion sputtering, the rutile TiO_2(110)-(1×1) surface becomes rough due to the bombardment of energetic ions. To smoothen and flatten the rough substrate surface at the atomic scale, a thermal annealing step is carried out. The sample is heated to a temperature of approximately 960 K (Kelvin) for a duration of 30 minutes. At this temperature, the surface atoms have sufficient thermal energy to diffuse and rearrange, resulting in a more uniform and stable surface. The thermal annealing process helps to restore the surface morphology and remove any defects or roughness caused by the Ar ion sputtering. It promotes the formation of a well-defined and smooth surface suitable for subsequent experiments or characterizations. After more than 20 cycles sputtering and annealing, clean and (oxygen vacancy dominated) reduced surface is generated (shown in black color). And the ion-sputtering system is shown in below:

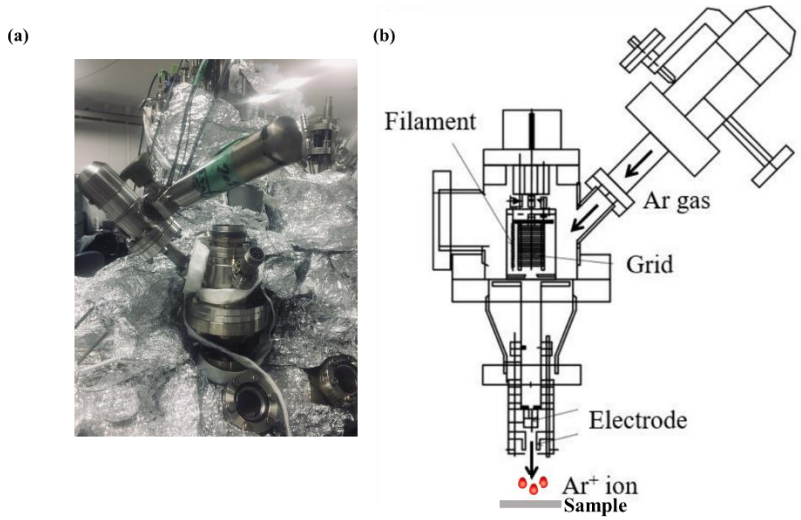

Figure 3.6 Ion gun sputtering device.

3.4.2 Cantilever preparation

The force sensor was an iridium-coated on top of the silicon cantilever (Nano Sensors SD-T10L100, f_0 ~ 1.08 MHz, and force constant ~ 900-4000 N/m). Oscillation amplitude was 500 pm. The tip apex was cleaned at 600 K and Ar ions sputtered to remove the contaminants. Cantilever is shown in Figure 3.7.

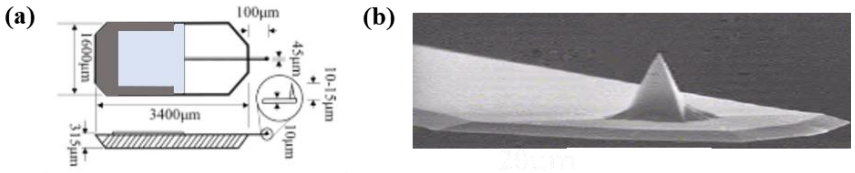

Figure 3.7 (a) Diagram of cantilever. (b) TEM image of the cantilever.

Cantilever is fixed on the cantilever holder by graphene, as shown in Figure 3.8.

Figure 3.8 (a) Cantilever, (b) cantilever holder and (c) a fixed cantilever to the holder.

To enhance the conductivity and improve the electrical properties of the silicon cantilever, an iridium coating is applied on top of it. The iridium coating is a thin layer of iridium material that is deposited onto the surface of the silicon cantilever using a suitable deposition technique such as physical vapor deposition (PVD) or sputtering. The iridium coating serves multiple purposes. Iridium is chosen as the coating material due to its excellent electrical conductivity, chemical stability, and compatibility with

silicon-based systems. It forms a durable and low-resistance interface with the silicon cantilever, ensuring reliable electrical connections and minimizing signal loss. Firstly, it acts as a protective layer, preventing the silicon cantilever from being damaged or contaminated during experiments or handling. Secondly, it provides a conductive pathway, allowing electrical signals to be transmitted between the cantilever and the external circuitry. This is particularly important in techniques such as KPFM where electrical measurements are performed using the cantilever.

3.5 AFM unit and operation system

In this section, we briefly introduce the experimental system and unit, including preparation chamber, main chamber, operation unit, and detection system.

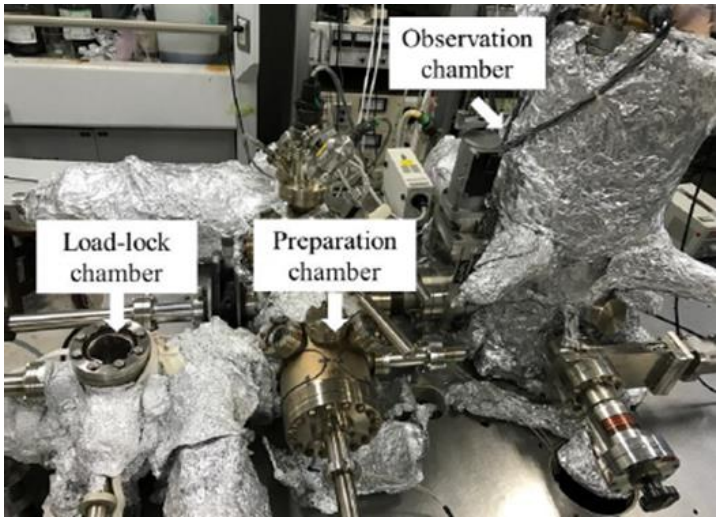

Figure 3.9 Ultra-high vacuum NC-AFM system.

Ours machine mainly contains three parts, load-lock chamber, preparation chamber, and main chamber. The vacuum of load-lock chamber is 1.0×10^{-10} Torr evacuated by rotary pump with turbo molecular pump, and new sample and cantilever are exchanged from this part. The vacuum of preparation chamber is 2.5×10^{-11} Torr, which part is pumped by sputter ion pump. And the sample and cantilever preparations are operated in the preparation chamber. As for the main chamber, the temperature is kept by liquid nitrogen at 78 K, and the vacuum below 2.5×10^{-11} Torr is evacuated by ion pump. All the experiment studies are operated in the main chamber. The schematic of the fabricated machine is shown in Figure 3.9. Observation chamber includes an inner tank and an outer tank filled with liquid nitrogen. To minimize external heat radiation, a triple shield is employed. By placing the measurement unit in contact with the bottom of the dewar and immersing it in liquid nitrogen for a duration of at least two days, and the temperature can be kept at 78 K.

To keep measurement system stable when scanning the atomic image, external vibration and coil spring of operation unit are used. External vibration is an active vibration isolation platform manufactured by HERZ Company of Japan, which consists of sensors, feedback circuit controllers, and actuators that are highly sensitive to the external weight. The whole system is placed on the active vibration isolation platform. During the experiment, measurements of displacement, velocity, or acceleration are captured by the sensors. The actuator then converts the electrical voltage into a mechanical force. Compared to passive vibration isolation systems, the active damping system does not exhibit resonance or amplify vibrations at any frequency, making it highly advantageous for achieving precise and stable measurements. At the unit of operation, coil spring and magnet are used to suspend the sample stage and isolate vibration. The magnetic damper operates by generating a magnetic field that interacts with a magnet attached to the unit cell. This interaction creates a damping effect, reducing the oscillations and vibrations of the unit cell. By implementing the magnetic damper, the stability and sensitivity of the NC-AFM measurements are enhanced, allowing for more accurate and precise imaging and analysis.

The AFM unit mainly consists of a sample stage, cantilever stage, piezo tube, reflection mirror, and laser focusing mirror. The sample stage is connected to piezoelectric actuator, which can allow the sample to move approaching the cantilever and scan in three dimensions. Cantilever holder supports the cantilever and causes it to oscillate by applying drive voltage. The signal transition is consisted by laser loop. Namely, laser is exported from fiber transmitted to the first mirror, then reflected by cantilever, and transmitted to the second mirror, finally collected by photodetector (PD). And the cantilever oscillation can be reflected by the electric signal of PD.

The precise alignment of the sample stage is achieved using the stick-slip approaching mechanism. This mechanism utilizes an approaching piezoelectric actuator, specifically an inertial-driven shear piezoelectric element stack, which generates stick-slip motion through stick-slip actuation technology. To reduce friction, a sapphire plate is attached to the bottom of the stage, and a hemispherical ruby ball is fixed on top of the actuator. The piezoelectric elements are stacked on top of each other, and when an external electric field is applied to both sides of the stack, it induces shear deformation of the elements. A triangular pulse wave voltage is applied to the shearing piezoelectric elements to induce the stick-slip motion of the sample stage [18,19]. This motion is achieved through a cyclic process consisting of stick and slip modes. During the stick mode, the applied bias voltage gradually increases, causing the shearing piezoelectric actuators to deform. As a result, the sample stage experiences movement due to the friction between the ruby ball and the sapphire plate. This gradual increase in voltage allows the sample stage to approach the desired position. Once the bias voltage reaches its maximum value, it suddenly drops. However, due to the inertia of

the sample stage, it cannot immediately follow the retraction of the shearing piezoelectric actuators. By repeating this cyclic process of stick and slip modes, the sample stage can gradually approach the tip or target position.

Next, we talk about the signal detection system. The force interaction between tip and surface can be detected from frequency shift of oscillated cantilever, which reflects the laser signal to the photodetector analyzed by phase-lock loop (PLL). Various techniques have been employed to detect deflection in cantilevers, encompassing a diverse range of methods. These include the utilization of piezoelectric force sensors, optical beam deflection detection (OBD), and optical interferometer detection [20]. In our system, we use OBD method, a focused laser beam is directed onto the cantilever, and the deflection of the cantilever alters the trajectory of the laser beam. This change in the beam's path is detected and measured using optical sensors, allowing for precise quantification of the cantilever deflection.

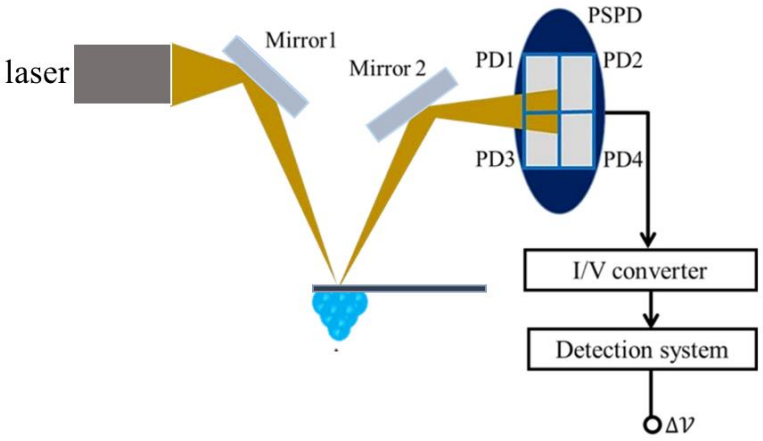

Figure 3.10 Schematic diagram of OBD method.

The laser beam is generated by a laser diode located outside of the chamber. To transmit the laser into the chamber, an optical fiber is employed. And the laser beam is directed onto the backside of the cantilever by mirror 1. A position sensitive photodetector (PSPD) is employed to detect the laser beam reflected by mirror 2. By adjusting the positions of the two mirrors, the laser beam can be aligned, and its spot can be positioned precisely on the center of the PSPD. The position of the laser spot on the PSPD can be altered due to the deflection of the cantilever, resulting in a change in the photocurrent detected by the PSPD. The detected photocurrent is then amplified using a voltage amplifier, typically through an I/V converter. Consequently, the amplified voltage signal serves as the detection signal for further analysis and measurement.

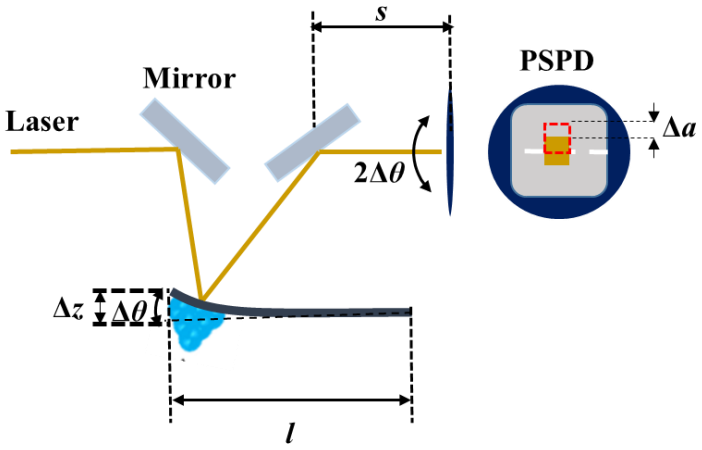

Figure 3.11 Schematic of optical beam deflection working process.

During the scanning process, the deflection angle of both the cantilever and the laser beam can vary in accordance with the displacement of the cantilever. These changes in deflection angle are detected and captured as the measuring signal by the measuring system. The displacement of the cantilever induces the deflection of angle, the relationship can be descripted as [21]:

$$\Delta\theta = \frac{3}{2}\frac{\Delta z}{l}, \tag{3.1}$$

where l is the length of cantilever, Δz is the displacement of cantilever, and $\Delta\theta$ is the deflection angle. The deflection of the cantilever leads to the detection signal shift of PSPD at $2\Delta\theta$. And the spot signal shift Δa as shown in Figure 3.18 can be deduced:

$$\Delta a = 2\Delta\theta \cdot s, \tag{3.2}$$

here, s is the distance between PSPD and the quadripartite photodiode. Combining equation (3.1) with (3.2), we can get the signal shift value

$$\Delta a = 3\frac{s}{l} \cdot \Delta z. \tag{3.3}$$

The amplification factor $\Delta a/\Delta z$ is the deflection sensitivity. In this way, oscillation amplitude of cantilever is measured by PSPD. The laser strength is conversed by photoelectric circuit, and then electrical signal is sent to the processor [22].

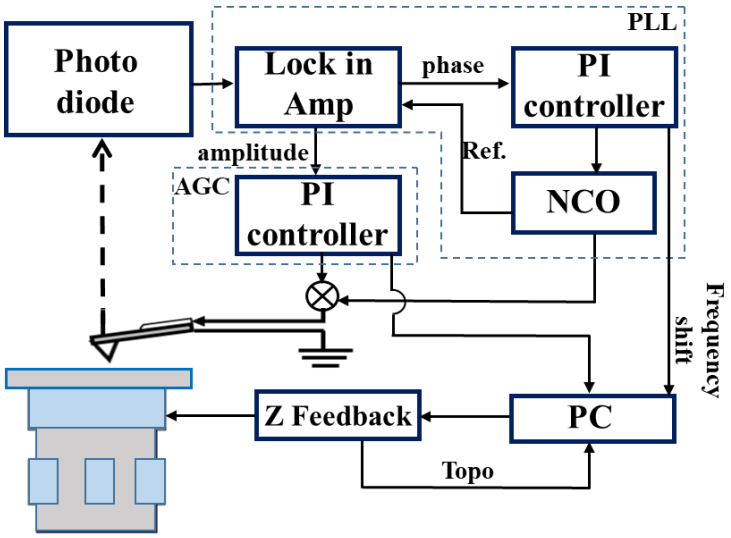

Figure 3.12 Schematic of FM-AFM control circuit.

FM-AFM circuit is shown in Figure 3.12. Laser signal detected by PD is transmitted to the PLL circuit, which consists of lock-in amplifier (LIA), PI controller and numerically controlled oscillator (NCO) reflection regulator. The phase signal is obtained and fed into the PI-controller system. It has been observed that when the cantilever is excited at its resonance frequency, the actual vibration phase is delayed by 90 degrees. To address this phase difference, the vibration phase signal is input to the NCO, and then fed back to the cantilever. This feedback loop ensures that the phase difference between the vibration signal of the cantilever and the excitation signal is consistently maintained at -90 degrees. Furthermore, the amplitude of the detected signal is input into an automatic gain control (AGC) circuit. From the AGC circuit, a PI-control mechanism is employed to adjust the amplitude, aiming to match the oscillated amplitude when it is fed back to the cantilever. This feedback loop helps maintain a desired and consistent amplitude for accurate measurements and control of the cantilever's vibration. Meantime, topographic image can be obtained from *z* feedback signal. To measure the surface potential information, we added the KPFM circuit in parallel to this circuit, as shown in Figure 3.13.

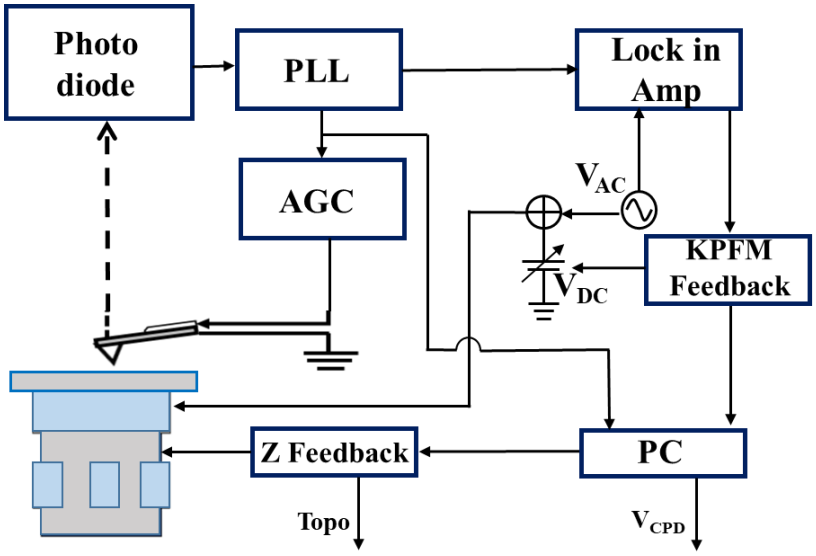

Figure 3.13 Schematic FM-AFM/KPFM simultaneous measurement.

In the FM-AFM with FM-KPFM circuit, frequency shift of oscillated cantilever is generated from AGC while keeping the constant oscillation amplitude. And the frequency shift signal is detected by PD and split into two paths through a PLL circuit. One path is used to measure the oscillation difference while tip-sample interaction, and the other path is used to lock-in amplifier for KPFM circuit. The DC bias voltage (V_{DC}) controller works by nullifying this signal through adjustment of its output, which is added to the modulated AC signal from signal generator. The AC voltage as a reference signal is demodulated by lock-in amplifier, then local surface contact potential difference information can be obtained from applied bias voltage, showing as CPD image.

Chapter 4 Investigating the adsorption characteristics of atoms/molecules on the TiO_2(110) surface

4.1 Introduction

In this chapter, we first introduce the surface and subsurface defects, which are important for surface properties, such as surface charge accumulation, the polaron effect, and surface adsorption. And then, we show the properties of surface adsorbate affected by surface defects. Finally, the surface adsorbates identification and operation are achieved using AFM and KPFM techniques, which can be used to investigate the nature of surface adsorption.

4.2 Surface and subsurface defects of TiO_2(110)

Surface and subsurface defects occur on the surface structural imperfections of TiO_2. These defects include vacancies, interstitials, impurities, dislocations, and other irregularities in the crystal lattice of the bulk TiO_2 sample. Surface defects plays a significant role in shaping the properties and behaviors of TiO_2, particularly with respect to surface reactions and interactions with adsorbed species. These defects can affect surface charge accumulation, catalytic activity, and surface reactivity. For example, surface defects can create localized electronic states that facilitate or suppress the adsorption of molecules or atoms onto the TiO_2 surface. Similarly, subsurface defects can also influence the properties of TiO_2 by altering its bulk structure and surface properties. They can affect diffusion rates, charge transfer, and the stability of adsorbates on the TiO_2 surface. Understanding the nature and behavior of surface and subsurface defects is crucial for optimizing the performance of TiO_2-based semiconductor catalysis.

Oxygen vacancy is one of the most common surface defects. An oxygen vacancy is the absence of an oxygen atom in the crystal lattice of TiO_2, specifically on its 2-coordinated oxygen rows. The oxygen vacancy occurs when one or more oxygen atoms are missing from their regular positions within the lattice structure due to ion sputtering. Oxygen vacancies can significantly influence the surface properties and reactivity of TiO_2. On the (110) surface of TiO_2, oxygen vacancies can lead to several effects. Firstly, they create localized electronic states within the bandgap, which can affect the electronic structure and optical properties. These states can trap charge carriers and influence the conductivity and catalytic activity. Secondly, oxygen vacancies can alter

the surface chemistry of TiO_2. They provide active sites for adsorptions.

Besides, lattice interstitial Ti atom is also a kind of defect. Ti interstitial in TiO_2 refers to a titanium atom that occupies an interstitial position within the crystal lattice. It occurs when a titanium atom is located in an interstitial site instead of its regular position within the lattice structure. The presence of Ti interstitials can have various effects on the properties of TiO_2. They can affect the optical and catalytic properties, alter the electronic structure and influence the diffusion and mobility of charge carriers within the sample. Interstitial Ti atom can also influence the surface reactivity and adsorption behaviors. They can act as active sites for adsorption and participate in surface reactions. Therefore, the presence of Ti interstitials can modify the surface charge distribution and influence the interaction between TiO_2 and adsorbed species.

The oxygen vacancy and Ti interstitial will induce polarons on the surface. Usually, the presence of point defects on transition-metal oxide surfaces can result in the generation of excess electrons. These excess electrons have the ability to locally couple with ionic vibrations, leading to the formation of small polarons. And polarons also influence the surface adsorptions and reactions.

There is another condition that is the dynamic adsorption of water molecule on the TiO_2(110) surface. The water molecule adsorbs at a 5-fold coordinated titanium (Ti_{5c}) site and then spontaneously dissociates at an O_v site [1, 2]. Water dissociation produces hydrogen and hydroxyl species, whereas hydroxyl is adsorbed at titanium rows (Ti rows) to form OH_t and hydrogen bonds to oxygen rows (O rows) to form OH_b. Therefore, hydrogen-containing defects affect the characteristics of the surface [3-7].

4.3 Surface adsorption properties influenced by surface and subsurface defects

To verify the reaction processes of molecules on TiO_2(110) surface, the adsorption mechanism needs to be found. In our research, carbon monoxide, oxygen and gold (Au) are deposited to the surface. The reduced surface without adsorbates is shown in Figure 4.1. Oxygen vacancy is generated during sample preparation, and near the O_v is the site 0, following site 1, site 2 and site 3, which are used to statistic the adsorption sites of molecules affected by this defect.

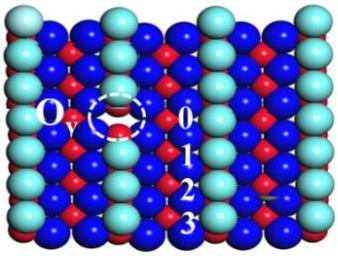

Figure 4.1 Reduced TiO_2(110) surface dominated by oxygen vacancy (O_v).

The reduced sample is transferred into main chamber (2.5×10^{-11} Torr), waiting for the molecule adsorption (oxygen remained in the chamber). Two hours later, we can find that some adatoms appeared on the surface, as shown in Figure 4.2.

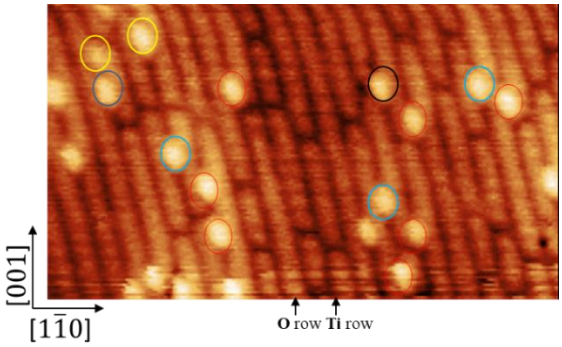

Figure 4.2 Molecule adsorption on the reduced TiO_2(110) surface. Different adsorption sites are marked by colored circles.

In the topographic image, O_v shows black line at O rows. The adsorption sites of molecules are distributed around the O_v defects. We take statistic of these atoms' adsorption site, as shown in Table 4.1. Site 0 is black column, site1 is red column, site 2 is blue column, site 3 is light blue column, and site 4 is yellow column. From the result of adsorption sites calculation, we can get the conclusion that site 1 is the most preferred position for atoms adsorption.

Table 4.1 Distribution of adsorption sites of adatoms.

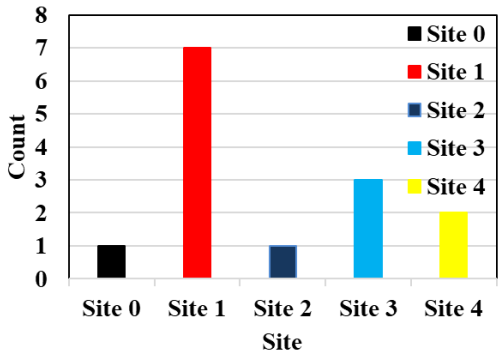

Surface defect influences the adsorption properties can be briefly described as the

site 1 is the stable position for atoms adsorption. The charge distribution or energy barrier near the surface defects can be explained by polaron effect. Next ,we will show the experimental results about surface adsorption：water molecules and hydroxyl, which is the surface adsorption properties study.

4.4 Surface adsorbates identification and operation by AFM/KPFM

The following section is based on the publication:
Qiang Zhu, Yuuki Adachi, Yasuhiro Sugawara, Yanjun Li*, Tip-Induced Dynamic Behaviors of a Water Molecule and Hydroxyl on the Rutile TiO_2(110) Surface.
J. Phys. Chem. C 2022, 126, 31, 13062–13068.

4.4.1 Background

The adsorption and bonding properties of hydroxyl species on metal oxide semiconductor surfaces and interfaces are important for the understanding of catalytic reactions. Surface charge distribution and polaron formation are also affected by hydroxyl species. In this section, we combined atomic force microscopy and Kelvin probe force microscopy techniques to distinguish H_2O and hydroxyl (OH_t at titanium rows and OH_b at bridging oxygen rows) on the rutile TiO_2(110) surface at 78 K. We achieved the manipulation of water molecules and hydroxyl groups to hop across different rows, which is important for understanding the adsorption mechanisms of hydroxyl and further reaction research based on semiconductor catalysis.

In this study, we identified the hydroxyl species on the TiO_2(110) surface by NC-AFM and KPFM at 78 K. We controlled the diffusion and desorption of water molecules and OH_t on the surface. Our results of the precise assignment and manipulation of hydroxyl species would have wide interest in the applications of catalyst- and electrochemistry-based metal oxide semiconductors.

4.4.2 Method

The experiment was performed by using a home-built NC-AFM apparatus equipped with an OBD system under ultrahigh vacuum (2×10^{-11} Torr) at 78 K. The force sensor of the NC-AFM was a commercial Ir-coated silicon cantilever (Nano Sensors SD-T10L100, $k \approx 1500$ N/m, $f_0 \approx 1.08$ MHz). The NC-AFM was operated in the frequency modulation mode with a constant oscillation amplitude of 500 pm. A small oscillation

amplitude increases the spatial resolution. To minimize the thermal drift, atomic tracking and feed-forward methods were used to position the tip on top of the target atoms.

4.4.3 Results and Discussion

The morphological features of the TiO_2(110)-(1 × 1) surface were observed by NC-AFM. The surface consists of two-fold-coordinated bridging oxygen rows (bright rows) and five-fold-coordinated titanium rows (dark rows), as shown in Figure 1. Water exists in the main chamber even under ultra-high vacuum conditions [8]. Some water molecules are dissociated into OH groups, whereas others remain on the surface. In this experiment, we obtained the morphological and CPD properties of OH_t (hydroxyl adsorbed at titanium rows), OH_b (hydrogen bonds to oxygen rows), O_v, and H_2O on TiO_2(110) surface by AFM and KPFM.

In AFM imaging modes, hole and neutral modes can be determined from the contrast of OH_b [9]. The contrast of OH_b appears dark in the hole mode and bright in the neutral mode. However, it is difficult to judge O_v, O_{row}, and hydrogen-included species from the topographic image. In the hole mode, the contrast of O_v is the same as that of OH_b, which is observed as a dark hole in Figure 1a. In the neutral mode, OH_b is difficult to distinguish from the oxygen row as shown in Figure 1d. Combining with the CPD images, the contrast of O_v and OH_b appears as a dark hole, and that of OH_t appears as a bright spot in Figures 1c, f, so we can distinguish these species as shown in Table S1. The negatively charged O_{ad} appears bright in topographic image 1a and CPD image 1c. We marked double charged O_{ad} as O^{2-} and single charged O_{ad} as O^- [10, 11]. Here, O_{ad} was used as the reference species.

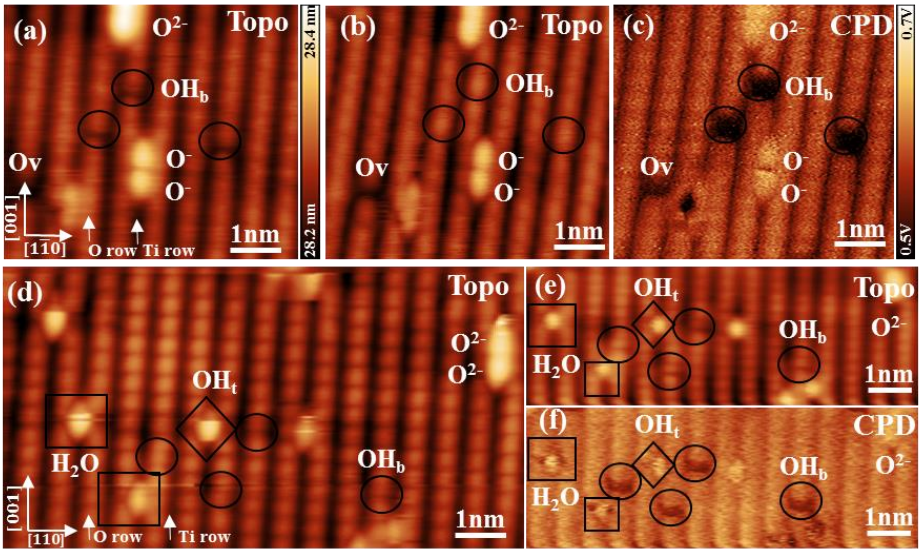

Figure 4.3 AFM and KPFM images ((hole mode (a-c) and neutral mode (d-f)) of half-

oxidized rutile TiO_2(110)-(1 × 1) surface. (a) Topographic AFM image in hole mode. (b, c) Simultaneous nc-AFM and KPFM measurements in the same area. The contrast of OH_b in (b) is the same as that of O_{row} shown bright, whereas OH_b shows dark spot in (a). The CPD contrast of OH_b shows darker than that of O_v in (c). (d) Topographic AFM image in neutral mode. (e, f) Simultaneous nc-AFM and KPFM measurements in the same area. Imaging parameters: f_0 = 1.081 MHz, A = 500 pm, Q = 21,707, and T = 78 K.

It is noted that for Figure 4.3(a), only AFM was carried out, and for Figures 4.3 (b, c), AFM and KPFM measurements were simultaneously carried out. The contrast of OH_b in Figure 1b is different from that in Figure 4.3(a), because the bias of KPFM automatically compensates the surface constant potential, inducing an electrostatic interaction between the tip apex and OH_b. In KPFM images, the positively charged O_v and H of OH_b appear as a dark contrast, whereas OH_b is darker than O_v. The configuration of water molecule consists of a dark spot combined with a bright spot enclosed by rectangles, whereas that of OH_t consists of one bright spot enclosed by rhombus, as shown in Figure 4.3(f).

Identification of OH species

The contrast of topographic and V_{CPD} images with all species in Figure 1 are shown in Table 4.2.

Table 4.2 List all types of species and appearances by two different tip apexes (Si or OH and positive charge)

	Hole mode in (a)-(c)		Neutral mode in (d)-(f)	
	AFM	KPFM	AFM	KPFM
O^-/O^{2-}	Bright	Bright	Bright	Bright
O_v	Dark	Dark		
OH_b	Dark	Dark	Bright	Dark
OH_t			Bright	Bright
H_2O			Bright with dark	Bright with dark

To confirm the species of adsorbates, the manipulations of the hydrogen and oxygen were performed. Firstly, we applied a pulse to the sample at the site indicated by black arrow as shown in Figure 4.4. After the manipulating, we found that the black line disappears, which indicates the hydrogen desorption from the surface as shown in Figure 4.4(b). Then, we applied a positive bias from 0 V to 1.5 V on top of oxygen atom

for further manipulation. After the manipulating, the oxygen became brighter, which indicates the oxygen charged as shown in Figure 4.4(c). The operated OH_t is enlarged in the black rectangle. From the manipulation results, it can be confirmed that the adsorbed specie is OH [12,13].

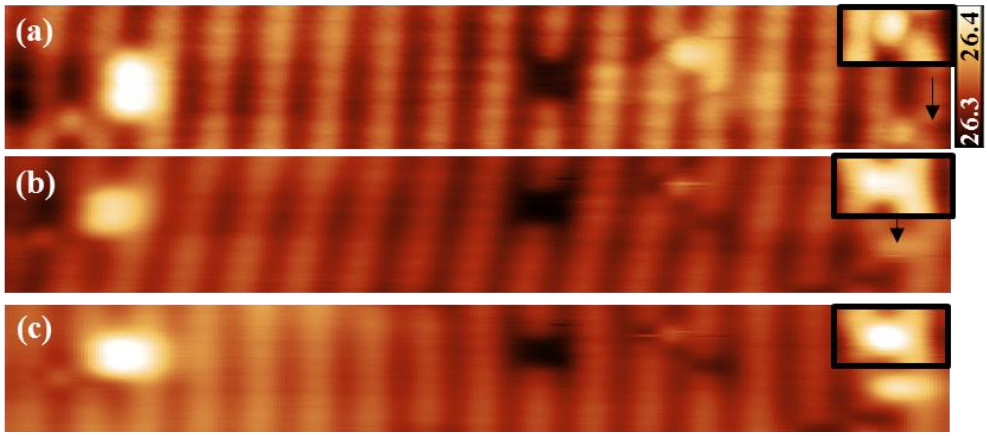

Figure 4.4 OH_t manipulation. (a) Voltage pulse at the site indicated by black arrow. (b) and (c) are manipulation processes of hydrogen desorption and oxygen charged. The first process from (a) to (b) is hydrogen desorption from surface as shown in the enlarged black rectangle. And the second process from (b) to (c) is oxygen charging process. Size: 11 × 1.5 nm^2.

From the manipulation results of hydrogen desorption and oxygen charged, we can deduce two possible structures of the adsorbed species as shown in Figure 4.5. One structure is OH_b with O_{ad}, and the other structure is OH_t.

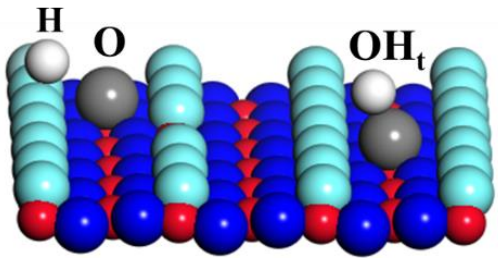

Figure 4.5 Ball model of adsorption structure on TiO_2(110) surface. Bright blue balls: O_{2c}; dark blue balls: O_{3c}; red balls: Ti.

To confirm the adsorption configuration of OH, the bias voltage of 1 V was applied to the sample during scanning in constant height mode. Figure 4.6 shows the forward and backward topographic images, respectively. We found that the difference of AFM images between forward and backward processes, which indicates hydrogen swing from left side to right side (see block arrow) as shown in black circles.

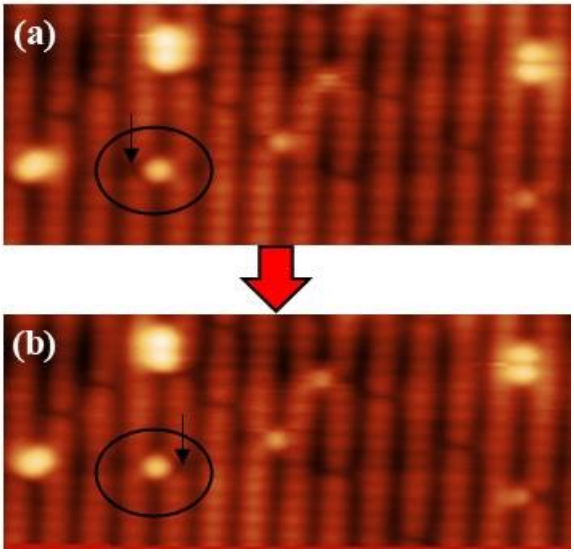

Figure 4.6 Electric field induced hydrogen swing at each side. AFM images of (a) forward and (b) backward. The bias voltage of 1 V on the sample. Size: 10 × 4 nm^2.

Next, we investigated the effect of hydrogen swing by the force. In detail, the adsorption structure of OH depends on the tip-sample distance. When the tip-sample distance decreased, we found that hydrogen swing at two different sides from right in Figure 4.7(a) to left in Figure 4.7(b) (see black arrows).

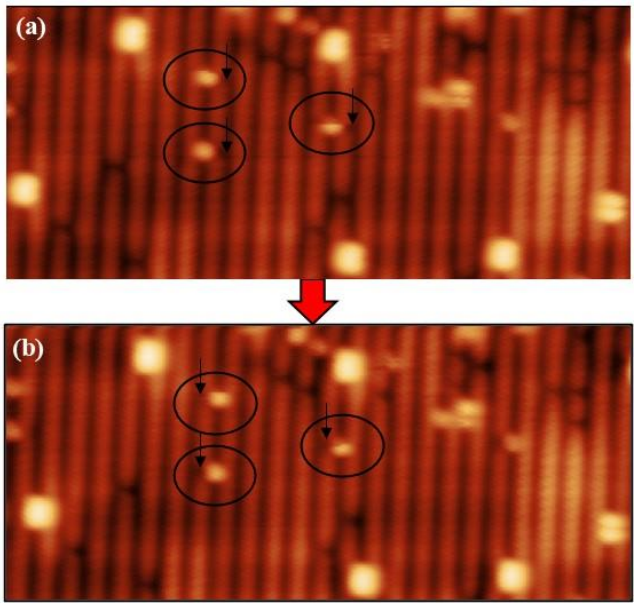

Figure 4.7 Force induced hydrogen swing at each side. AFM images of (a) forward and (b) backward (bias voltage 0 V). Size: 13 × 6 nm^2.

Based on the induced hydrogen swing resulting from bias and force, we can ascertain that the structure is OH_t. Conversely, achieving hydrogen swing over the O_{ad} in OH_b solely through force interaction without external energy (bias voltage) proves

challenging [14,15].

Figure 4.8 shows the topographic images of O^{2-} and OH_b on TiO_2(110) surface in neutral and hole modes, respectively. From the line profiles in Figure 4.8 (b)(e), we find that the height difference between OH_b and the oxygen row is 36 pm. We also carried out frequency shift spectroscopy, and the results are shown in Figure 4.8(c)(f). With the decrease in tip-sample distance, the frequency shift at the OH_b site first decreases, then increases, and finally decreases, whereas the frequency shift at the O site always decreases. These results are in good agreement with the calculations and experiments [16-18]. Therefore, the identification of OH_b can be preliminarily distinguished by the height difference and the frequency shift spectroscopy.

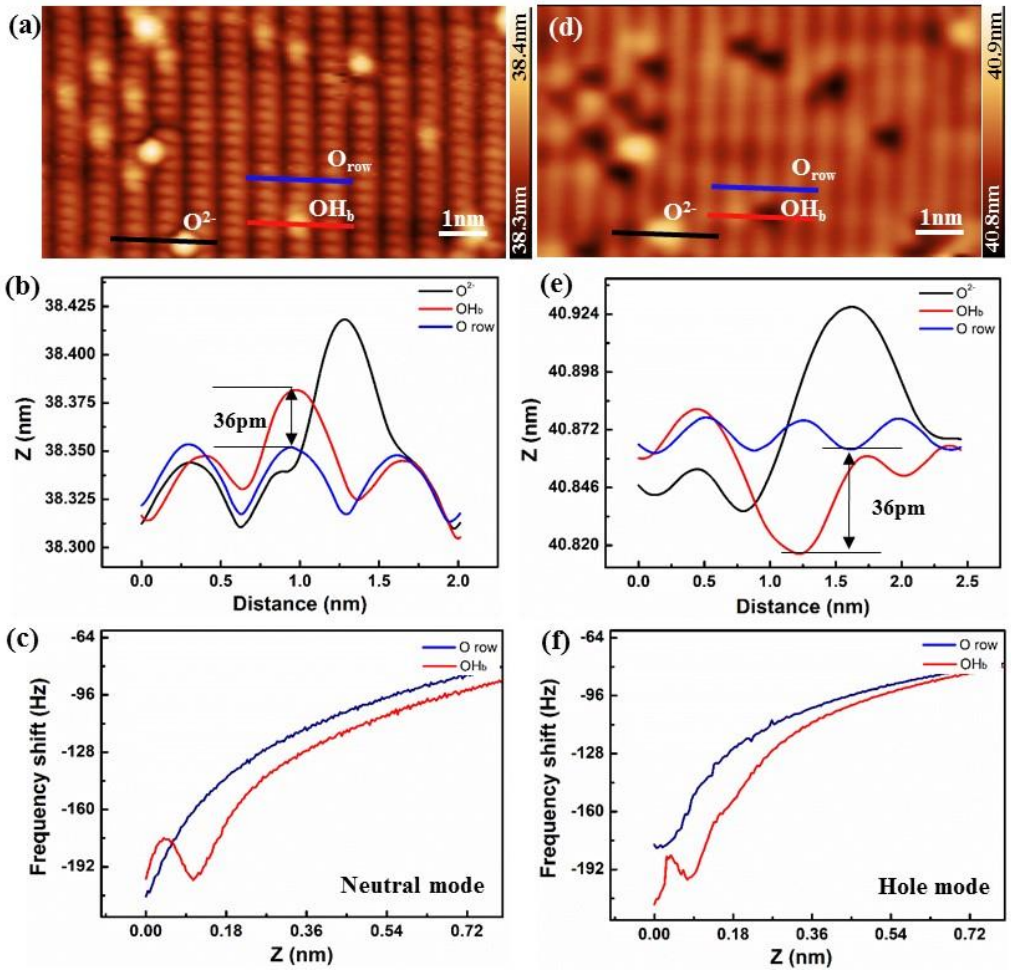

Figure 4.8 AFM images in neutral and hole modes (10 × 6 nm^2). (a) Topographic image, (b) line profiles, and (c) frequency shift spectroscopies in neutral mode. (d) Topographic image, (e) line profiles, and (f) frequency shift spectroscopies in hole mode. O^{2-}, black line; OH_b, red line; and oxygen row, blue line. The height difference of OH_b was measured from the oxygen row to OH_b. Imaging parameters: f_0 = 1.081 MHz, A = 500 pm, Q = 21,707, and T = 78 K.

Next, we discuss the presence of a double peak in the frequency shift spectroscopy.

We consider that the tip was terminated by an OH group [19]. The interaction between the tip apex and OH can be speculated such that the hydrogen on the tip apex repelled the hydrogen of OH_b with decreasing the tip-sample distance. Hence, attractive interaction between the tip apex and OH_b increased and then decreased, and hence, the first minimum of frequency shift appeared, and the hydrogen of the tip apex moved away. Then, attractive interaction between the oxygen of the apex and the hydrogen of OH_b increased with further decreasing the tip-sample distance, and the frequency shift decreased again as shown in the red curve in Figure 4.8(c)(f). As for the bridging O site, the attractive interaction between OH on the tip apex and O increased, so the frequency shift shows a parabolic shape.

In the hole mode, we manipulated the OH_b species many times. Here, we present the results of two consecutive manipulations, as shown in Figure 4.9. The tip was moved to the position marked by the blue arrow, and the bias voltage was applied to the sample [20, 21]. The voltage was gradually increased until a jump of the frequency shift occurred, as shown in black curves in Figure 4.9(d)(z). After applying the sample bias, the dark holes disappeared, as shown in Figure 4.9(b)(c). The jump of the frequency shift in the black curve indicates that the hydrogen desorbed from OH_b. The black and red arrows between the topographic images and frequency shift spectroscopies indicate the manipulation cycles in the order of Figure a →d →b →e →c.

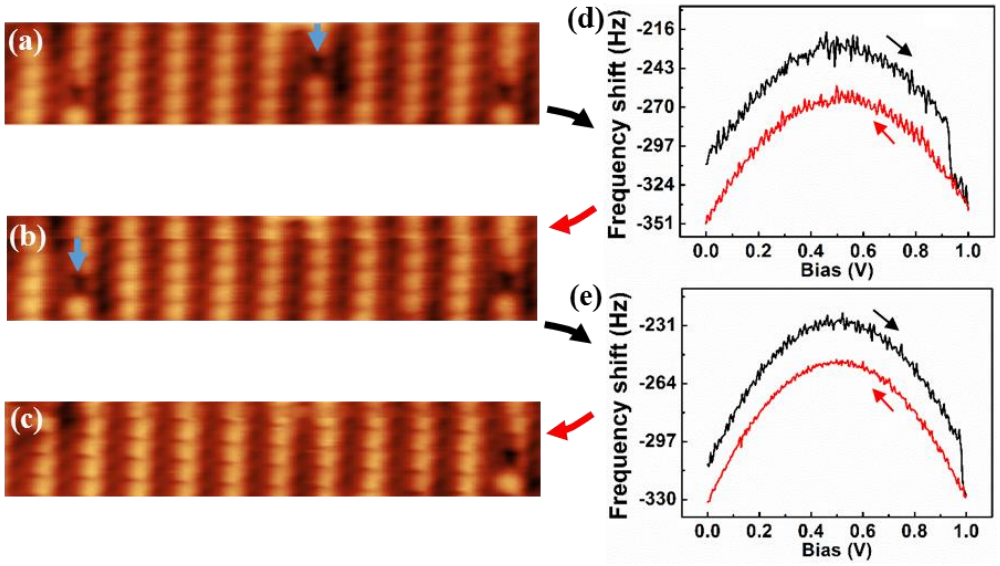

Figure 4.9 OH_b manipulation in hole mode. Topographic images (a) before and (b, c) after manipulation. (d, e) Frequency shift spectroscopies during (black curves) and after (red curves) manipulation. The positive bias sweep was applied from the sample to the tip. The black and red arrows indicate the forward and backward bias sweeps, respectively. Imaging parameters: $\Delta f = 320$ Hz, $f_0 = 1.081$ MHz, $A = 500$ pm, $Q = 21{,}707$, and $T = 78$ K. Size: 10×1.5 nm^2.

The tip-induced reaction in hole and neutral modes are different, although similar bias voltages are applied to OH_b. In the hole mode, the hydrogen desorbs from OH_b after manipulation. In the neutral mode, the hydrogen atoms of OH_b hop along the oxygen row, as shown in Figure 4.10. The manipulation cycles can also be performed in the order of Figure b → f → c → g → d.

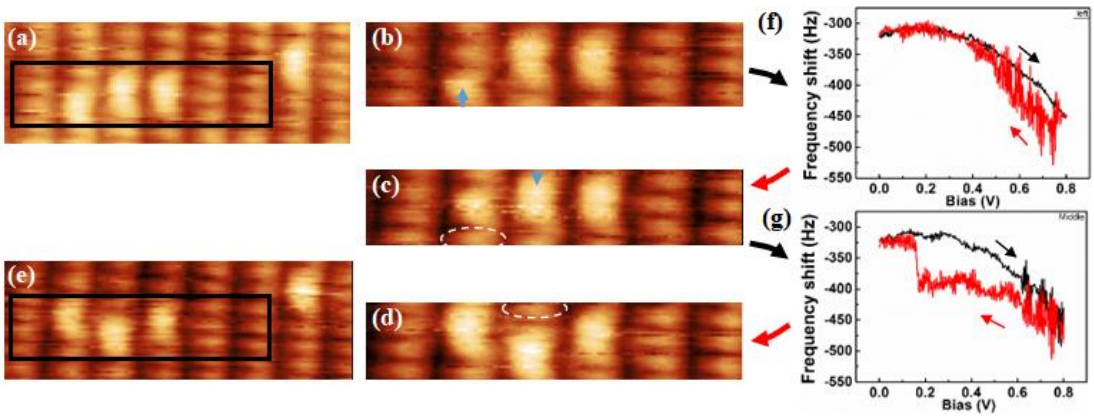

Figure 4.10 OH_b manipulation in neutral mode. AFM images (a) before and (e) after manipulation. (b-d) OH_b manipulation processes. (f, g) Frequency shift spectroscopies. The positive bias sweep was applied from the sample to the tip. Black and red arrows indicate the forward and backward bias sweeps, respectively. Imaging parameters: Δf = 320 Hz, f_0 = 1.081 MHz, A = 500 pm, Q = 21,707, and T = 78 K. (size in (a) and (e): 5.5 × 1.5 nm^2; size in (b)-(d): 3.5 × 1 nm^2).

In the neutral mode, we operated hydrogen atoms by consecutive manipulations, as shown from Figure 4.10(b-d). Figure 4.10(f, g) shows the frequency shift spectroscopies. The white dashed circles indicate the initial hydrogen position. After manipulation, the hydrogen of OH_b hopped to the upper oxygen site and did not desorb from the surface, as shown in Figure 4.10(c, d). It has been pointed out that the manipulation of OH_b in the neutral mode is different from that in the hole mode. In detail, the bias voltage was gradually increased until the manipulation event was found, and then the bias was decreased to 0 V. When the bias voltage was applied to the sample, a local electric field between the tip and the hydrogen atom was generated. The time of application of the bias was 3 ms in both modes. In the neutral mode, the tip apex is not active. The local electric field enabled the hydrogen atom to overcome the energy barrier and diffuse on the surface without desorption. In the hole mode, the tip apex is positively charged and active. The combination of the local electric field and the tip-atom interaction deformed the potential energy of the hydrogen atom, enabling the hydrogen atom to overcome the energy barrier and desorb from the surface.

Before demonstrating the manipulation of water molecule and OH_t in the hole mode, we first confirm the configuration of OH_t, which is shown in Figure 4.4. The results of

two consecutive manipulations show that the configuration of the adsorbate is a combination of hydrogen and oxygen, and its model is shown in Figure 4.5. From the results of the hydrogen shift upon applying a weak bias voltage (Figure 4.6) and the force interaction between the tip and the atom (Figure 4.7), we can confirm that the adsorbed specie is OH_t.

To understand the chemisorption property of hydrogen-containing species for the study of catalytic reactions, we manipulated a water molecule and hydroxyl on the surface. We chose the target area to operate the water molecule enclosed in the black rectangle in Figure 4.11. Before manipulating, we turned on the atomic tracking function to decrease the thermal drift of the relative positions. The tip was moved to the left of the water molecule marked by the blue arrow. A bias voltage was gradually increased until the manipulation event was found and then returned to zero. The current signal was monitored during the manipulation, as shown in Figure 4.11(f, g). After the bias voltage was returned to zero, an AFM image of the same area was obtained immediately, as shown in Figure 4.11(c). We found that the water molecule hopped to the adjacent Ti row: the manipulation sequence is in the order of Figure 4.11(b) → 4.11(f) → 4.11(c). Then, we moved the tip on top of the water molecule and applied the same bias voltage to the sample, and the water molecule desorbed from the surface as shown in the order of Figure 4.11(c) → 4.11(g) → 4.11(d). The manipulation of the water molecule is more difficult than that of OH_b, so we extended the integration time of bias sweep to 10 s to improve the success rate.

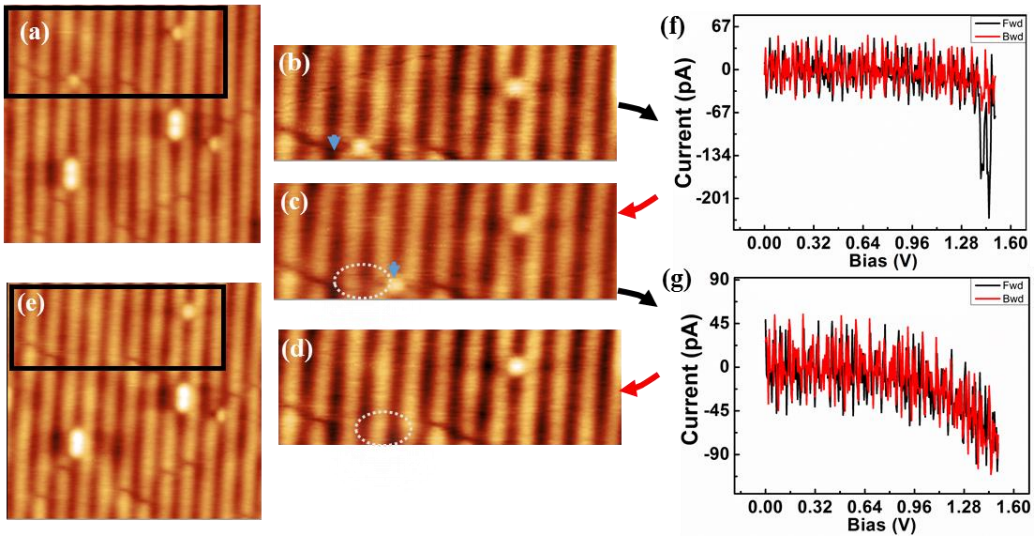

Figure 4.11 Manipulation of water molecule on the TiO_2(110) surface. (a) Initial and (e) final AFM images. (b-d) AFM images of consecutive manipulations. *I-V* curves in (f) and (g) during manipulation. The bias voltage ranged from 0 to 1.6 V. The black and red arrows indicate the forward and backward bias sweeps, respectively. Imaging parameters: Δf = 320 Hz, f_0 = 1.081 MHz, A = 500 pm, Q = 21,707, and T = 78 K. (size in (a) and (e): 7 × 7 nm^2; size in (b-d): 8 × 3.5 nm^2).

The entire manipulation cycles can be performed in the order of Figure b → f → c → g → d. The manipulation of the water molecule is based on the local electric field and tip-atom interactions. When the bias voltage was larger than 0.96 V, the current decreased, which can be regarded as an event that happened. The current flow was also disturbed by the hopping of the water molecule, as shown in Figure 4.11(f, g). We manipulated OH_t in the same way, as shown in Figure 4.12.

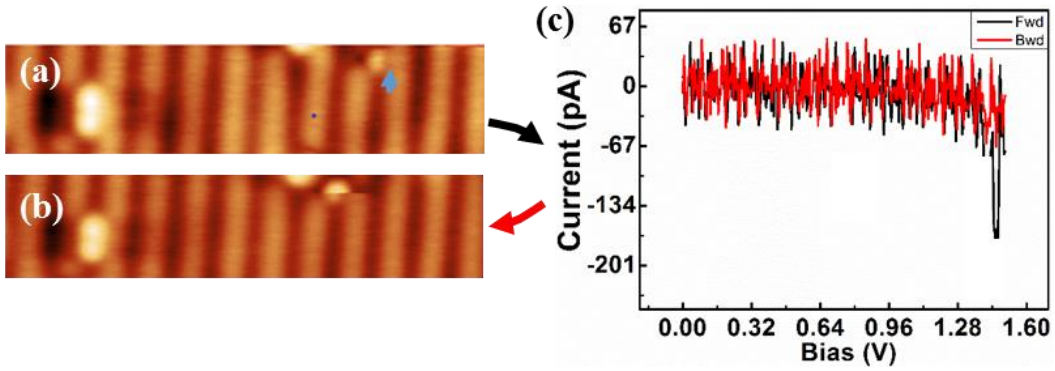

Figure 4.12. Manipulation of OH_t on TiO_2(110) surface. AFM images (a) before and (b) after manipulation. (c) I-V curve during manipulation. The bias voltage ranged from 0 to 1.6 V. The black and red arrow indicates the forward and backward bias sweep, respectively. Imaging parameters: Δf = 320 Hz, f_0 = 1.081 MHz, A = 500 pm, Q = 21,707, and T = 78 K. (size in (a) and (b): 8 × 2 nm^2).

The OH_t can be manipulated in the order of Figure a → c → b. The tip was moved near the OH_t site indicated by the blue arrow in Figure 6a, and the bias was gradually increased until a current was formed, and then returned back to zero (Figure 4.12(c)). Then, the AFM image in Figure 4.12(b) was immediately obtained after the forward and backward bias-current sweep in Figure 6c. After the bias sweep, OH_t hopped to the adjacent Ti row. The small scratch of the manipulated OH_t in Figure 4.12(b) indicates the dynamic adjustment of H atom. After that, the OH_t cannot be manipulated even when a larger bias voltage was applied to the sample, owing to the enhancement of the adsorption energy of OH_t by the adjacent O_{ad}.

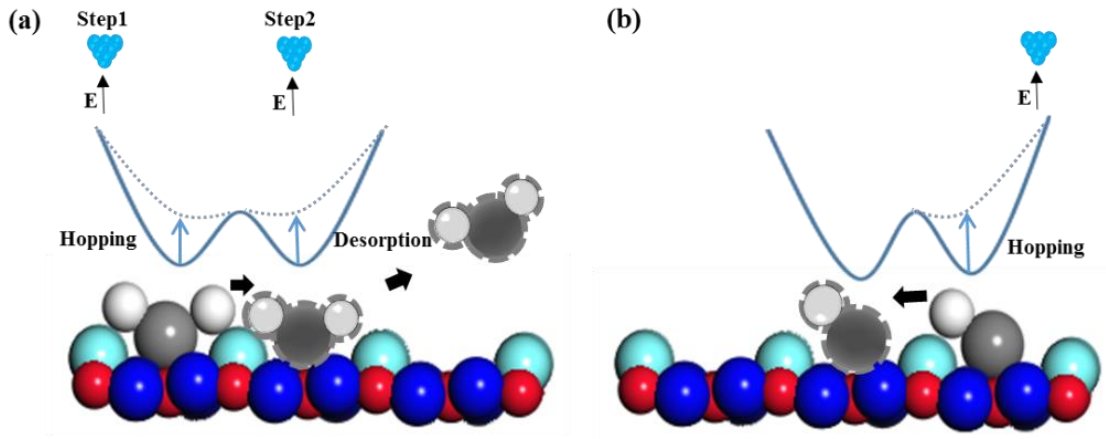

Figure 4.13 Ball model and corresponding manipulation mechanism of (a) the water molecule and (b) hydroxyl (OH_t). The black arrows indicate the direction of movement of the water molecule and hydroxyl. The blue arrows indicate the perturbation of the potential. The ball surrounded by dashed lines indicates the position of the water molecule and hydroxyl after manipulation. The solid and dash curves indicate the potential energy depending on the position of adsorbates and the bias between the tip and the sample. Bright blue balls, O_{2c}; blue balls, O_{3c}; red balls, Ti; dark balls, O of H_2O; white balls, H of H_2O.

The ball model is introduced to illustrate the manipulation mechanism of the water molecule and hydroxyl, as shown in Figure 4.13. In the first step, the tip was placed close to the water molecule, and then a bias voltage was applied to the sample, generating a local electric field from the sample to the tip. In this manner, the water molecule overcame the diffusion energy barrier and jumped to the adjacent Ti row under the effects of the local electric field and tip-molecule interactions. When the second bias was applied on top of the water molecule with a longer integration time, the vertical electric field provides energy that, when combined with tip-molecule interaction, induces the water molecule to desorb from the surface. The same process for OH_t is shown in Figure 7b. The longer integration time increases the success rate of operation.

4.5 Conclusions

In this chapter, we clarified the OH species in the neutral and hole modes and demonstrated the manipulation of a water molecule and OH_t on the TiO_2(110) surface by AFM and KPFM at 78 K. The manipulation was induced by applying a positive sample bias, which generates a local electric field. The combination of short-range force and a local electric field stimulates species to overcome the energy barrier and hop on the surface. We hope that the manipulation of water molecules and hydroxyl groups

with an atomic resolution can be used for understanding the mechanisms of reactions based on semiconductor catalysis. The identification of adsorptions is essential for researching the surface and surface adsorption property.

Chapter 5 Investigating the adsorption properties of CO molecules on the TiO_2(110) surface

5.1 Introduction

In this chapter, we first introduce the adsorption of CO molecules on the TiO_2(110) surface at 78 K. CO adsorption characteristic is important for the studying of CO oxidation. We discuss the CO movement properties in one- and two-dimensional. The study and operation of CO movement can be used to find the suitable site for the catalytic reaction of CO molecule with O_2.

5.2 The adsorption of CO molecules on the TiO_2(110) surface

To find the mechanism of CO oxidation process, the adsorption property research of CO molecule on the TiO_2(110) surface is important. Studying the fundamental steps of catalytic reactions on metal oxide surfaces yields valuable insights in various technological fields, including heterogeneous catalysis, gas sensors, photo-catalysis, and the photooxidation of organic pollutants. Rutile TiO_2, a wide band gap semiconductor with a band gap of 3.0 eV, particularly its (110) surface, has emerged as a model system for investigating reactions on metal oxide surfaces. The interaction of molecular oxygen with TiO_2 surfaces has gained significant attention due to its involvement in photooxidation and water splitting reactions as talked in chapter 4. Temperature programmed desorption (TPD), electron stimulated desorption (ESD), and STM have been employed to investigate different aspects of oxygen chemistry on TiO_2(110). At low temperatures and high O_2 coverage surface, physisorption of O_2 has been observed. Chemisorption of more than one O_2 molecule at an oxygen vacancy site has been reported in previous chapters, and two distinct channels of O_2 dissociation have been identified. To gain a deeper understanding of catalytic reactions involving oxygen on TiO_2 surfaces, studies of adsorbed species with oxygen are necessary. Despite notable advancements in this field, there has been only one reported STM investigation on the interaction between an oxygen adatom and CO adsorbed on TiO_2(110). Furthermore, there has been limited correlation between results obtained from atomic-scale techniques and ensemble-averaged techniques.

Some researchers have investigated the interaction between molecular CO and

atomic O adsorbed on a reduced TiO_2(110) single crystal surface. To explore the interaction, they employ various techniques including STM, ESD, TPD, and DFT calculation. Findings reveal the presence of an attractive interaction between the two adsorbates, as evidenced by the formation of surface CO-O and CO-O-CO complexes. To complement the atomic-scale results, they also present results from ensemble-averaged techniques such as ESD and TPD, which further support the observed interactions. The adsorption model is shown in below.

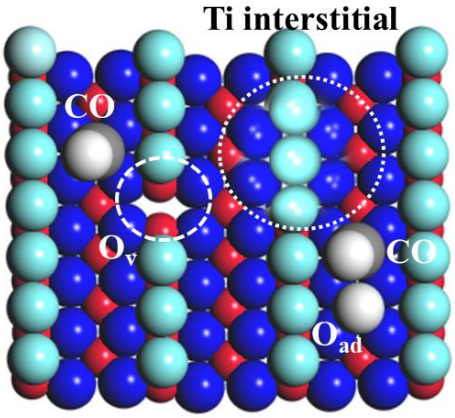

Figure 5.1 Adsorption model of CO molecule influenced by surface defects: O_v, Ti interstitial, and oxygen adatom.

Because of the surface and subsurface defects, adsorption property of CO molecules is strongly influenced by these defects. In the further research, the detailed CO adsorption properties are verified.

5.3 CO molecules motion in one- and two-dimensional

The following section is based on the publication:
Qiang Zhu, Yasuhiro Sugawara, Yanjun Li*, Exploration of CO Movement Characteristics on Rutile TiO_2(110) Surface.
Colloid Surface A 2023, 656, 130402.

The interaction of adsorption molecules with surface active sites of catalysts is the basis of understanding catalytic reactions, which requires knowledge of adsorption energy, thermal stability, and charge distribution. The investigation of adsorption properties of surface adsorbates, such as surface molecular adhesion, charge transfer induced conversion of the chemical state, and molecular dynamic behaviors, is also essential for characterizing the catalytic reactions based surface catalysis [1-9]. The most important application of the CO oxidation reaction on metal oxide surface has

attracted considerable interest for a long time [10-16]. The investigation of CO adsorption properties on different surfaces by SPM is the initial step towards understanding the fundamental mechanism of CO oxidation [17-21]. Studies as that of CO molecule manipulation have been proposed to examine the vibrational excitation molecular dynamic behavior in various surfaces [22-24]. The adsorption configuration of CO molecules on a metal surface was explained by multistep excitation, which is used for clarifying the equivalent molecular orientations: metal-carbon stretching *v* (M-C) and C-C stretching *v* (C-C). Komeda *et al*. demonstrated the electron-stimulated migration of CO molecules adsorbed on a Pt(110) surface with the C-O stretching mode by STM [25]. Morgenstern *et al*. also confirmed the three-body interaction between diffusing CO molecules by an experimental method [26]. Long *et al*. proposed that CO adsorbates promote polaron photoactivity on reduced rutile TiO_2(110) surface [27]. They found that the adsorbed CO attracts polarons to the surface, allowing them to participate in catalytic processes with CO. The adsorption property of CO molecules on TiO_2 surface was measured to understand the elementary processes of CO activation on a catalyst surface [28,29]. NC-AFM is an excellent tool not only for characterizing the atomic structure but also for detecting the force interactions between the NC-AFM tip and the surface. The lateral force induced one-dimensional CO movement along Ti row at the TiO_2 surface by AFM has been proposed, and the force component between the tip and the adsorbate can be directly measured without electronic influence.

In this chapter, we will show two adsorption (stable and movement) states of CO molecules on rutile TiO_2(110) at 78 K. The effect of oxygen adatoms on CO adsorption is verified by force interaction between CO and the tip apex, and the two-dimensional movement state can be achieved with short-range force. The characteristic of CO movement on TiO_2(110) surface is detected by NC-AFM with the lateral drag mode of the oscillation cantilever.

5.3.1 Experimental conditions

The experiment was measured with an OBD unit UHV (5.0×10^{-11} Torr) at 78 K. The NC-AFM was operated in the frequency modulation detection mode. To compensate the thermal drift, atomic tracking method was used, and the sample bias V_s was applied at 0 V to prevent the tunneling current effect. The force sensor was an iridium-coated silicon cantilever (Nano Sensors SD-T10L100, f_0 = 1.08 MHz, and spring constant k = 1500 N/m). Oscillation amplitude A was 500 pm. The tip apex was cleaned by annealing at 600 K and Ar ions sputtering to remove the contaminants.

5.3.2 Results and Discussion

A rutile TiO_2(110)-(1×1) surface contains two-fold coordinated oxygen atoms rows with bright contrast and five-fold coordinated titanium atoms with dark contrast. Usually, the oxygen of the oxidized surface participates in catalytic reactions; therefore, oxygen molecules were exposed to the surface to heal the O_v and to trap free electrons. In addition, the dissociation of oxygen molecules on the rutile TiO_2(110) surface also generates O_{ad}, which affect surface properties [30-32]. The study of CO adsorption characteristics was carried out on the oxidized TiO_2(110) surface. All AFM images are obtained in neutral mode [33,34].

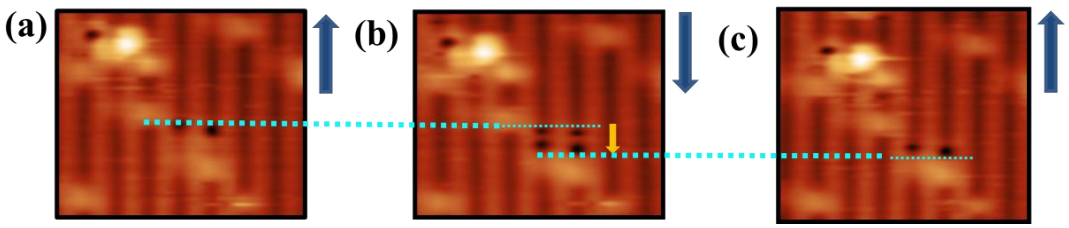

Figure 5.2 CO molecule adsorption and movement at 78 K on the TiO2(110) surface.

CO was exposed to the surface while obtaining the stable topographical image; then, dark spots appeared, as shown in Figure 5.3. There were two states (stable state and movement state) of CO molecules in the experiment because CO diffusion and desorption easily occur on the TiO_2(110) surface at 78 K [35]. The contrast of CO in movement state shows a triangle shape compared with the stable state that shows a dark spot, as shown in Figure 5.3 [36].

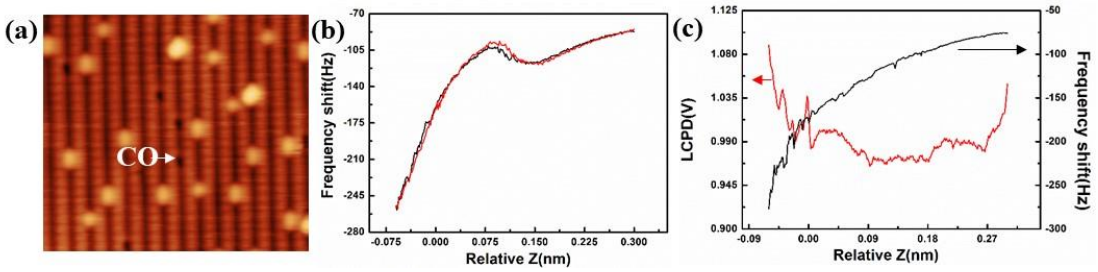

Figure 5.3 Stable state CO molecules on the TiO_2(110) surface. (a) Topographic image of the stable CO molecules on TiO_2 surface at far tip-sample distance. (b) Frequency shift spectroscopy measured on top of CO molecule marked by white arrow. (c) Bias vs Z spectroscopy.

The dark spots observed in Figure 5.3(a) correspond to the CO molecules on the Ti rows in the stable state. How to judge the CO molecules? We measured the frequency spectroscopy on top of dark spot as shown in Figure 5.3(b). According to existing results, two minimum value of the spectroscopy indicates the interaction between CO

with tip. Besides, as shown in bias spectroscopy of Figure 5.3(c), the increasing LCPD value from constant value, coupled with the decreasing tip-sample distance, indicates the presence of a dipole moment within the CO molecule, where the electron of the covalent bond shifts from the carbon atom to the oxygen atom.

The conversion state of CO from the stable state to the movement state can be achieved by decreasing the tip-sample distance approximately 10 Å in the experiment. By decreasing tip-sample distance, the CO movement direction was consistent with the scanning direction, and finally stopped near the O_{ad} site. In the NC-AFM manipulation mode, one-dimensional movement of CO molecules on the surface is induced by the repulsive lateral force in the "pushing" mode, which is considered to be due to the potential between the surface and the CO molecules being perturbed by the tip, namely, the tip-induced potential reorganization [37-40]. The tip-induced potential contains chemical, van der Waals, and electrostatic force. In atomic experimental measurements, the tip-induced potential is dominant in the on-surface molecular lateral manipulation. When the tip approaches the CO molecules, the lateral force breaks the potential landscape of CO on top of the Ti atom and pushes it to hop along the Ti row. Moreover, the adsorbed oxygen atoms also have a strong effect on the CO adsorption and movement properties even the tip interacts with CO. Three consecutive scanning results regarding the CO movement affected by the O_{ad} are shown in Figures 5.4(a) to (c).

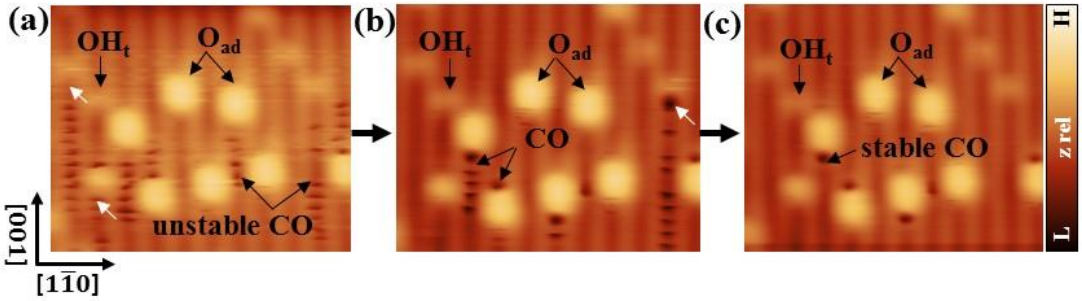

Figure 5.4 Topographic images under consecutive scanning of the same area on rutile oxidized TiO_2(110) surface with CO molecules (0.05 L). (a) Many unstable CO molecules are shown as dark spots. (b) Few stable and unstable CO molecules. (c) Stable CO molecules near O_{ad}. Desorption of some unstable CO molecules indicated by white arrows. (Imaging parameters: Δf = 380 Hz, f_c = 1.08 MHz, A = 500 pm, Q = 18707, T =78 K, size: 6.5×6 nm^2)

The surface CO molecules may exhibit small thermal vibration because of the finite temperature ~78 K. Therefore, the number of CO molecules decreased after scanning many cycles, and the desorbed CO molecules were marked by white arrows, as shown in Figures 5.4(a) to (c). Finally, CO stopped near the O_{ad} sites, as shown in Figure 5.4(c). Here, the atomic defects on the surface and at the subsurface introduce excess electrons

to the surrounding lattice, leading to polarons bound to the defects and local chemistry on the TiO_2 surface. Thus, CO molecules will choose a suitable site for their adsorption, such as O_v sites, and next-nearest-neighbor Ti_{5c} sites (NNN-Ti_{5c}). On the oxidized surface, negatively charged oxygen atoms act as non-equilibrium sites, breaking the potential landscape, thus attracting CO molecules that become stable at oxygen sites [41-43]. While OH_t is not activity site, which does not enhance the CO adsorption [44]. Therefore, CO at OH_t site always desorbs. Furthermore, we measured the force spectroscopy on top of the CO molecule to identify the O_{ad} effect on the CO adsorption property, as shown in Figure 5.5.

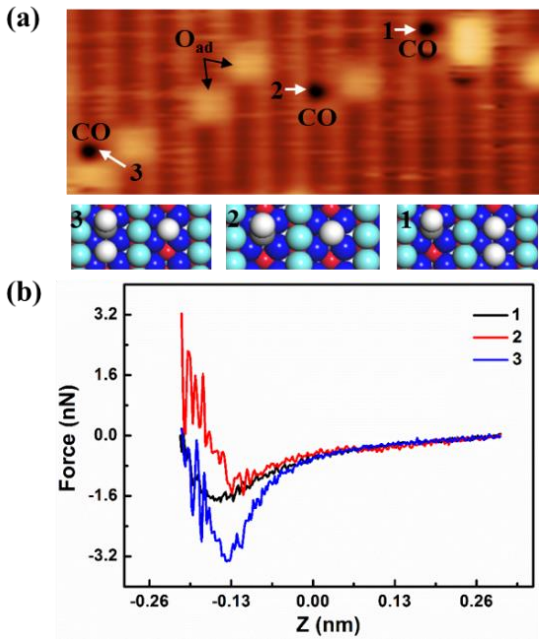

Figure 5.5 O_{ad} effect on CO adsorption. (a) Topographic image of CO adsorption at different O_{ad} sites with relative ball models. (b) Force spectroscopy of CO at different O_{ad} sites. *Z* is the relative tip-sample distance. Bright blue balls, O_{2c}; blue balls, O_{3c}; red balls, Ti; gray balls, C of CO; white balls, O_{ad} and O of CO. (Imaging parameters: Δf = 127 Hz, f_c = 1.08 MHz, A = 500 pm, Q = 18707, T =78 K, size: 8.5×3.5 nm^2.)

Figure 5.5 shows three different CO adsorption sites. The stable state was measured while CO was adsorbed near the O_{ad} site, as shown in Figure 5.5(a). The force curve shows two minima value of CO in the Ti_{5c} site in the supplementary information, corresponding to the weak physical and strong chemical interactions between the tip and the CO molecule. In Figure 5.5(b), the force curves show the parabolic shape. This indicates that CO undergoes a chemical interaction with the tip under the effect of adjacent adsorbed oxygen. When CO is near two O_{ad} sites marked by the number 1, the force is larger than that located near one O_{ad} site, marked by number 2. The force is the largest when CO is surrounded by O_{ad}, marked by number 3. This result demonstrates that the potential landscape is disturbed by O_{ad}, which strongly affects the CO

adsorption property. Therefore, we can conclude that CO adsorption at the oxygen site induces a stronger interaction with the surface. And the related model is shown in Figure 5.6.

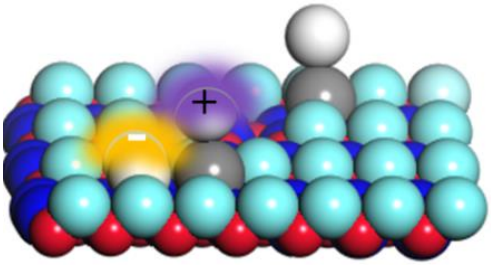

Figure 5.6 CO adsorption model enhanced by O_{ad}.

Because of the interaction of electron gas, positively charged CO molecule can be enhanced by negatively charged oxygen adatoms. The effect of O_{ad} on CO adsorption can be considered a topic of future CO oxidation catalytic research. Thus, the manipulation of CO at a suitable adsorption site is a crucial point in its oxidation reaction. Next, we will discuss a new phenomenon, two-dimensional CO movement on the TiO_2(110) surface at 78 K.

We herein focus on the dynamic behavior of the observed CO movement in two dimensions. The common tip apex usually induces CO movement in one dimension because the lateral component of repulsive force between the tip and the atoms is dominant. Here, we modified the tip apex to operate the CO molecules hopping over the Ti row and moving in two dimensions. The functionalized tip apex was terminated by oxygen atom, which is active for CO molecules not only in one-dimensional repulsive interaction but also in a lateral drag interaction. We applied the voltage bias on top of the oxygen atom at the TiO_2(110) surface. In this way, the oxygen atom can be picked up by the tip. The detailed description was given in a previous paper [45]. Next, we will show the two-dimensional transmission of CO molecules on the TiO_2(110) surface.

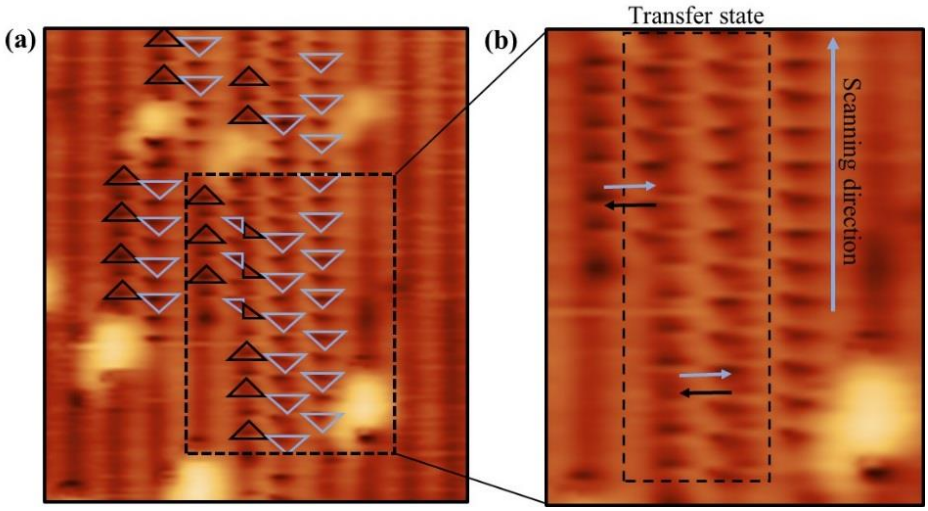

Figure 5.7. Two-dimensional movement of CO molecules on TiO_2(110) surface, operated using oxygen-terminated tip apex. (a) Topographic image of CO movement in two-dimensional. Upward and downward shapes of CO molecules are indicated by black and gray triangles, respectively. (b) Enlargement of black dashed rectangle area in (a). CO skips over the Ti row indicated by cross arrows. A single CO molecule movement along the Ti row on the right side is indicated by the longer gray arrow. (Imaging parameters: Δf = 125 Hz, f_c = 1.08 MHz, size a: 6×7 nm^2; size b: 3×4 nm^2.)

Two-dimensional movement of CO molecules are shown in Figure 5.7. The scanning direction was from down to up. Compared with the previous contrast of CO movement in one dimension, we found that the contrast of CO movement showed two structural shapes simultaneously, namely upward (black) and downward (gray) triangles, as shown in Figure 5.7(a). As we can see, in the transfer state marked by black and gray arrows, the bottom of upward triangles and that of downward triangles are at the same level. The two structural shapes reflect CO molecules in different states, corresponding to the two-dimensional movement of CO molecules movement with the scanning direction simultaneously [25]. CO on the right side hopped in one dimension, marked by the gray arrow shown in Figure 5.7(b). The transfer state in the middle part marked by the black dash rectangle shows CO skipping over the Ti row and moving in two-dimension on the surface. The two-dimensional manipulation of CO molecules can be regarded as a strong chemical interaction between the functionalized tip apex and the CO molecules, inducing the CO molecules to overcome the energy landscape and move around the surface. Compared with the vibrational excitation of CO molecules on metal surface, NC-AFM avoids the desorption of CO molecules on the TiO_2 surface at 78 K, making it effective for the manipulation of CO molecules moving to active sites to react with oxygen. The related mechanism is described below.

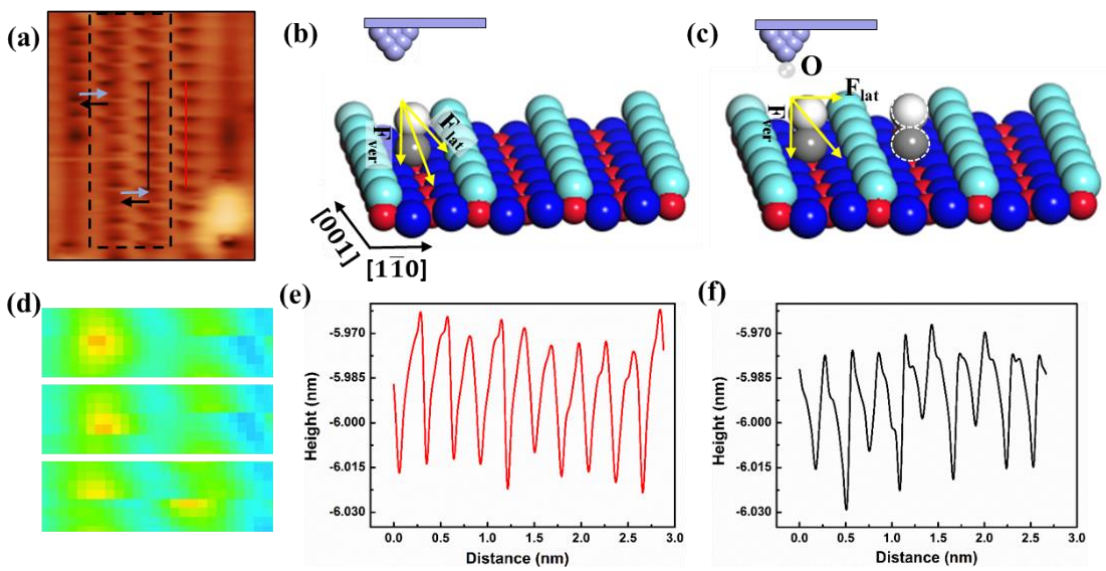

Figure 5.8 Mechanism of two-dimensional movement of CO molecules on TiO_2(110) surface. (a) Topographic image of CO movement. (b) One-dimensional and (c) two-dimensional movement models of CO molecule. (d) Force maps of CO molecule in three different states at different tip-sample distances, from up to down indicates stable (Δf = 100 Hz), one-dimensional (Δf = 115 Hz) and two-dimensional movement (Δf = 125 Hz) of CO molecule. (e) And (f) Line profiles of CO movement in one-dimensional and two-dimensional, respectively. Marked by red and black dash lines in (a). The height difference of one-dimensional movement is not obvious, while the height difference of two-dimensional is obvious in adjacent hopping. Bright blue balls, O_{2c}; blue balls, O_{3c}; red balls, Ti; gray balls, C of CO; white balls, O of CO. (Imaging parameters: Δf = 125 Hz, f_c = 1.08 MHz, size a: 3×4 nm^2)

The one-dimensional and two-dimensional movements of CO molecules on the TiO_2(110) surface are shown in Figure 5.8(a). Tip-induced CO movement vibration interaction is displayed in Figure 5.8(d), which reveals the force field of CO molecules under three different states. We tried to measure the Δf as a function of both the vertical and lateral tip position for the force-induced two-dimensional movement of CO molecules. However, the gradient of force spectroscopy measurements of two dimensional were difficult to obtain due to instability of CO molecules at 78 K. Figures 5.8(b) and 5.8(c) show the one-dimensional and two-dimensional movement models, respectively. The lateral force induced tip pushing mechanism for adsorbates moving on the surface has been reported, such as the movement of molecular CO on Cu(211) and Ag atoms on an Ag(110) surface [46,47]. The repulsive interaction between the tip and CO induces the pushing mode of CO movement. Furthermore, oxygen on the tip apex also interacts with CO and the force cause CO to overcome the energy barrier and hop to the adjacent Ti row. The contrast of CO molecules hopping in two states is

different, and we measured the line profiles of one-dimensional and two-dimensional movement states marked by red and black lines in Figure 5.8(a), as shown in Figures 5.8(e) and 5.8(f), respectively. The height difference of CO hopping across Ti row in $[1\bar{1}0]$ direction is ~10 pm smaller than that of CO hopping along Ti row in $[00\bar{1}]$ direction.

The vector force $F(x, y, z)$ is deduced from the cantilever frequency shift $\Delta f(z)$ [48,49]. Using the Sader-Jarvis formula, $\Delta f(z)$ can be converted to $F_z(z)$.

$$F_z(z) = 2k\int_z^{\infty}\left(1+\frac{A^{1/2}}{8\sqrt{\pi(t-z)}}\right)\Delta f/f_0 - \frac{A^{3/2}}{\sqrt{2(t-z)}}\frac{d(\Delta f/f_0)}{dt}dt, \qquad (1)$$

here, z, k, and A are the oscillation amplitude of the cantilever, the spring constant, and the vertical position. Then, potential $U(z)$ is obtained by the integration of $F_z(z)$ as

$$U(z) = -\int_{\infty}^{z} Fz(t)\,dt, \qquad (2)$$

then, vertical and lateral forces are calculated by deducing the derivative of the $U(z)$ in three directions:

$$Fv(x,z) = -\frac{\partial U(x,z)}{\partial z}, \qquad (3)$$

$$FL(x,z) = -\frac{\partial U(x,z)}{\partial x}, \qquad (4)$$

$$FL(y,z) = -\frac{\partial U(y,z)}{\partial y}. \qquad (5)$$

By keeping a certain interaction setpoint of the oscillation tip and CO molecule, the vertical force F_v causes the CO molecule to overcome the energy potential and the lateral force parallel to the Ti row, F_{Lx}, causes the CO molecule to hop in the scanning direction. Moreover, the lateral force perpendicular to the Ti row, F_{Ly}, causes the CO molecule to hop to the adjacent row.

5.4 Conclusion

We reported the adsorption and motion of CO molecules on a rutile TiO_2(110)-(1×1) surface at 78 K. We found that oxygen adatoms strongly influence the CO adsorption and mobility properties. Furthermore, the oxygen-terminated tip apex was used to probe the CO movement and enable the CO molecule to hop to the adjacent Ti row, achieving the two-dimensional manipulation of CO molecules. The result of CO movement in two-dimensions on TiO_2(110) surface will be of interest for the CO catalytic reaction at a precise site.

Chapter 6 Investigation of Au nanoclusters on the TiO_2(110) surface

6.1 Introduction

In this chapter, we first introduce the Au mediated catalytic reactions, which is an important topic for surface catalysis. And then, the charge states of Au nanoclusters were identified, which is essential to confirm the processes of CO oxidation with positively charged or negatively charged Au participating reaction. Finally, the CO oxidation was obtained on the TiO_2(110) surface by applying bias voltage at 78 K.

6.2 Au mediated surface catalytic reactions

Understanding the mechanism of the superior catalytic power of heterogenous catalysts is an important topic in surface chemistry [1-4]. Single- or few-atom catalysts have gained attentions due to their high efficiency, activity, and stability. Noble metals, such as Pt, Pb, Co and Au have been introduced to the metal/semiconductor surfaces to investigate the high efficiency of surface catalytic reactions [5-8]. The principal role of the supported metal was initially recognized the increase in the metal dispersion and surface area, and the stabilization of the active component. At subsequent research, the physicochemical interactions between the metal and the substrate had been discovered, which strongly influence the catalytic performance through carrier effects [9-11]. The specific carrier effect was firstly observed between the platinum metals and TiO_2. Based on this catalytic system, the classical strong metal-support interaction was put forward. Recently, single-atom catalysts have become a novel research topic of catalysts, suggesting that smaller nanoclusters could play an important role.

Therefore, the catalytic activities of supported noble metals strongly depend on size- and configuration [12-16]. In heterogenous catalysts, this is a particularly the case for gold nanoclusters on rutile TiO_2, which is an efficient catalytic system. Rutile TiO_2 is an active semiconductor material in industrial applications due to its excellent optical, electrical, and catalytic properties. The electron transfer from TiO_2 to gold nanoclusters leads to markedly improved stability and activity in catalytic reactions. Recent studies have revealed the factors of structure, size, facets, and charge state of nanoclusters [17-20]. The charge state of Au atoms and nanoclusters has been a subject of considerable debate in catalytic studies, particularly in the oxidation of CO molecules. Verifying the detailed charge participation in the binding process of CO oxidation remains a

challenge. Tremendous progress has been made in SPM. Probing the charge state of adatoms on supported surface has been demonstrated by scanning tunneling microscopy. However, this technique requires a conducting tunneling junction, which is incompatible with any material. Here, the charge properties of Au on TiO_2 surface can be demonstrated by measuring LCPD maps, which can directly reflect the charge states of Au without considering the conductivity characteristics of substrate.

In this chapter, we present the measurement of charge states of Au particles on the rutile TiO_2(110) surface with atomic resolution by NC-AFM and KPFM. Different adsorption sites and configurations induced differently charged properties of Au are identified.

6.3 Charge states identification of Au nanoclusters

All processes of sample preparation were operated in a vacuum chamber. First, the sample was sputtered with Ar ions of energy 1 keV for 15 min and annealed at 950 K for 30 min. After 20 cycles, a reduced TiO_2(110)-(1×1) surface can be obtained. Next, oxygen was exposed to the surface in the preparation chamber under a pressure of 5.0×10^{-9} Torr and the oxidized TiO_2(110)-(1×1) surface was obtained. And then, the sample was transferred to the observation chamber at 78 K. After the temperature of the sample decreased to 78 K, Au was deposited on the surface by an evaporator (EFM3 Omicron).

6.3.1 Experimental methods

The experiment was performed at a home-build ultrahigh vacuum (5.0×10^{-11} Torr) NC-AFM system under 78 K. The NC-AFM system was operated in the frequency-modulation mode, which is sensitive to the force gradient and obtains high measurement precision. In the experiment, an iridium-coated silicon cantilever with a spring constant of 1500 N/m was used as the force sensor, and the oscillation amplitude A was set to 500 pm. A laser beam was utilized to measure the deviation of the cantilever oscillation caused by the interaction between the cantilever and the sample, specifically employing the OBD method. KPFM images were obtained with the bias voltage feedback in constant-height mode. To compensate for thermal drift, an atomic tracking method was employed, and a sample bias (V_s) of 0 V was applied to mitigate the tunneling current effect.

6.3.2 Results and discussion

A rutile TiO_2(110)-(1×1) surface contains O rows in bright contrast and Ti rows in dark contrast [21]. The clean surface is shown in Figure 6.1(a), which is reduced surface after preparation in ultrahigh vacuum chamber. We can find surface O_v defect and bridge hydroxyl on O rows, showing short black lines on the bright rows. The identification between O_v and OH_b is easily distinguishable by the CPD image due to different charge characteristics [22]. Usually, O_v acts as the most dominant surface defect. The O_v induces excess electrons on the surface and subsurface. After oxygen molecules were exposed to the surface, O_v was filled, generating oxygen adatoms. And O_{ad} obtains excess elections to form O_{ad}^--O_{ad}^- and O_{ad}^{2-}-O_{ad}^{2-} as shown in Figure 6.1(b) [23, 24]. Therefore, in the topographic image of Figure 6.1(b), different contrasts of O_{ad} on the surface indicate different charge states. After the Au was evaporated on the chamber, much larger-sized adatoms can be observed on the surface as shown in Figure 6.1(c). In our sample preparation, deposition of Au atoms was controlled in low-rate flux (about 20 $nA \cdot s^{-1}$) using an electron beam heating evaporator. And the adsorption geometries of O_{ad} and Au are quite different, which can be clearly distinguished by height and size. Au displays brighter and bigger contrast than O_{ad}.

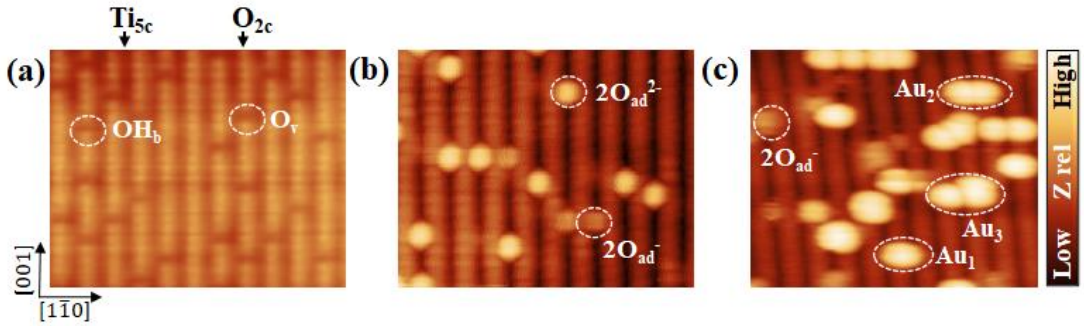

Figure 6.1 Topographic images of rutile TiO_2(110) surface at 78 K. (a) Before, (b) after oxygen adsorption at room temperature and (c) Au atoms deposition on the surface at 80 K. Oxygen vacancies on oxygen rows in (a), and oxygen adatoms with different charge states as bright spots at Ti rows. Au nanoclusters as brighter spots at around oxygen rows. Scale bar indicates relative tip height. Scanning parameters: f_c = 1.12 MHz, A = 500 pm, Q = 14360, T =78 K. Size: 8.0 × 6.0 nm^2.

As we know, surface defects cause the redistribution of surface charge states, so the charge states of adsorbed species such as Au, CO, and O_{ad} on TiO_2(110) are determined by these surface defects. The experimental and theoretical calculations have confirmed that O_v is the most abundant surface electron donor and the most favorable adsorption site for the oxygen [25-27]. The different charge states of O_v and O_{ad} have already been

studied by KPFM [28]. The obvious charge properties of O_v and O_{ad} can be identified, namely, O_v shows a positive charge, while the adsorbed oxygen captures electrons and shows a negative charge. Consequently, upon the deposition of Au onto the surface, the charge state of Au is depended on its adsorption position. The CPD images in Figure 6.2 illustrate the different charge states of Au at various adsorption locations.

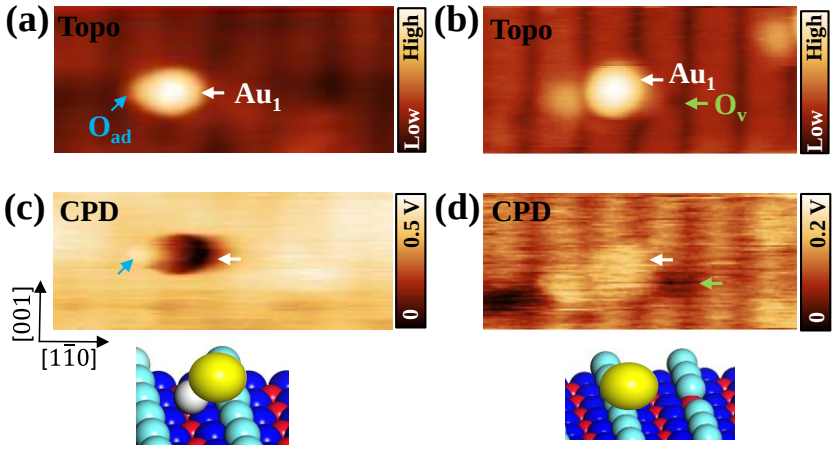

Figure 6.2 Charge state of single Au atom on different locations. (a) Topographic image and corresponding CPD image (c) of Au on the right of O_{ad} site. (b) Topographic image and corresponding CPD image (d) of Au on O_v site. Au: white arrow, O_{ad}: blue arrow, O_v: green arrow. Ball model with Au on different locations (white ball: $O_{ad,}$ yellow balls: Au, light blue balls: $O_{2c,}$ blue balls: $O_{3c,}$ red balls: Ti). Scanning parameters: f_c = 1.12 MHz, A = 500 pm, Q = 14360, T =78 K. Size: 4.3 × 1.8 nm^2.

In Figure 6.2(a), a single Au atom (marked by white arrow) adsorbs at the right of O_{ad} site (marked by blue arrow) and is positively charged. In this state, the strong non-metallic properties of oxygen lead to the electron shift within Au, which is typically expressed in Debye units. The electron distribution in Au is tilted towards the oxygen atom. Additionally, the redistribution of the electron cloud result in the formation of a dipole moment [29-31]. Therefore, Au is positively charged, as shown in dark circle, while the underlying O_{ad} is negatively charged, as shown in white spot in the CPD image of Figure 6.2(c).

In addition to the common result of positively charged Au on the rutile TiO_2 surface, we also observed negatively charged Au in the experiment. In the CPD image of Figure 6.2(d), a single Au atom adsorbs at O_v site and is negatively charged, as shown in bright circle. On the other hand, the positively charged O_v shows a dark hole. In this state, the formation of O_v introduces excess electrons into surrounding lattice, generating polarons bound to the around of O_v [32]. These polarons are responsible for the localized states within the band gap, showing prominent in-gap states below the E_F. And the polaron hopping is constrained around O_v due to its electrostatic attraction with

the positively charged O_v and the stronger el-ph coupling near the O_v [33,34]. The calculation showing that polarons strongly enhance the adsorption of CO, and the adsorbed CO attracts polarons, allowing them to participate in catalytic processes [35]. In the experimental results, the interplay between polaron and adatoms depends on their distance. After adsorption of Au near the O_v site, a strong electronic charge transfer occurred from polarons to Au atoms. Besides, excess electrons generated by additional surface and subsurface defects can also contribute to the negative charge of Au. The number of negatively charged Au cannot be abundant, which should be consistent with the existence of defects. Furthermore, we measured the charge state of Au nanoclusters on the surface.

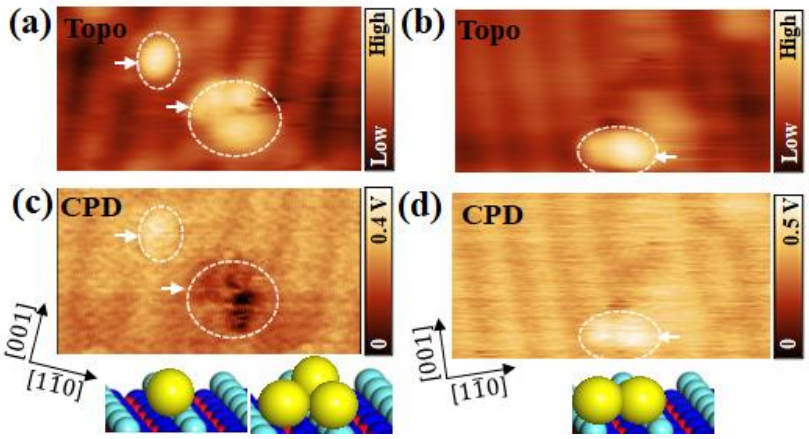

Figure 6.3 Charge states of single, dimer Au and Au nanoclusters on rutile TiO_2(110) surface. (a, b) Topographic images and corresponding CPD images (c, d). Ball model with Au nanoclusters (write ball: $O_{ad,}$ yellow balls: Au, light blue balls: $O_{2c,}$ blue balls: $O_{3c,}$ red balls: Ti). Scanning parameters: f_c = 1.12 MHz, A = 500 pm, Q = 13020, T =78 K. Size: 4.0 × 2.0 nm^2.

Au nanoclusters and single Au atom are shown in Figure 6.3(a), and dimer Au atoms are shown in Figure 6.3(b). In this case, the single Au atom is negatively charged due to the surrounding O_v, while the Au nanoclusters carry positive charges, as shown in CPD image of Figure 6.3(c). At the same time, we found that dimer Au atoms carry negative charges, as shown in CPD image of Figure 6.3(d). Because the charge state of Au nanoclusters depends on the local electronic environment, Zhang, and Salmeron et al. have found the method to reflect local chemical changes by work function [36]. They calculated the Coulomb potential, extracted the charge state using Wood's formula to modify isolated metal nanosphere and derived the work function change of grounded charged metal nanosphere. In this result, we consider the spatial distribution of the metal-induced gap states generated after Au nanoclusters adsorb at the oxygen vacancy and oxygen sites (O_{ad} and bridge O). And the localized metal-induced gap state below the Fermi level provides a channel for the charge transfer from the TiO_2 substrate to the

adsorbed Au nanoclusters. Dimer Au atoms carry electrons from subsurface, showing negatively charged. As for Au nanoclusters, electrons are accumulated at interface between Au nanoclusters and surface, which is the active site for catalytic reaction [37]. Thus, Au nanoclusters carry the positive charge. The related model of surface adsorptions configuration and charge distribution is shown in Figure 6.4.

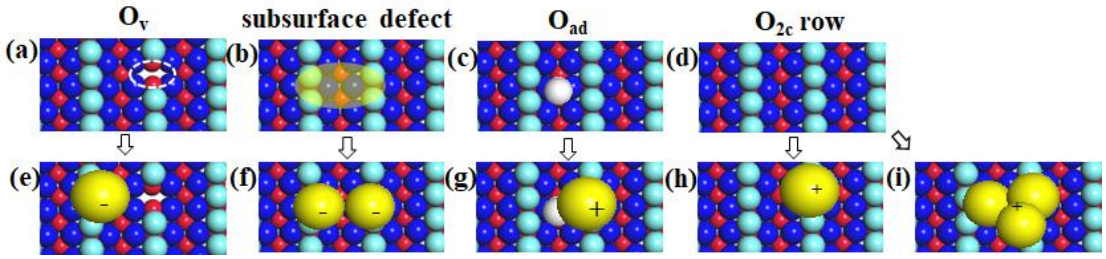

Figure 6.4 Ball model of Au charge states on the rutile TiO_2(110)-1×1 surface. Au: yellow balls, O_{ad} (oxygen adatom): white balls, O_{2c} (2-fold coordinated bridging oxygen atoms): light blue balls, O_{3c} (in-plane 3-fold coordinated oxygen atoms): blue balls, Ti_{5c} (5-fold coordinated Ti atoms): red balls.

According to experimental results, we put forward that negatively charged Au atoms are induced by O_v and subsurface defects, while positively charge Au atoms are induced by oxygen. Charge properties of surface adsorptions on rutile TiO_2 surface are complex due to surface/subsurface defects, polarons, diploe moment and so on. Identification of the charge properties of Au nanoclusters using KPFM method provides a research basis for understanding the principle of single atom catalytic reactions.

We have achieved the charge distinguishment of Au nanoclusters on TiO_2(110) surface by KPFM. The charge properties of Au nanoclusters can be recognized as O_v and subsurface interstitial electrons induced negatively charged Au, while oxygen induced positively charge Au. The result of negatively charged Au proves that the existence of polaron and charge transfer effect, which influences the state of surface adsorbates. The result of positively charged Au demonstrates that the dipole moment between Au atoms and oxygen. The experimental study on the charge states of Au nanoclusters provides an insight for further understanding the participation of noble metals in surface catalysis.

6.4 CO oxidation research

The charge properties of Au can be clearly identified by KPFM. Then, the CO oxidation reaction on TiO_2(110) surface is investigated. In this section, the effectiveness of positively or negatively charged Au in CO oxidation has been verified. To better understand the mechanism of charge influence of Au nanoparticles for CO reaction.

Here, we show the different charge states of Au nanoparticles in different conditions. As shown in Figure 6.5, single Au atom can exist two kinds of charges. Negatively charge Au located at O_v site, while positively charged Au located at oxygen site. The charge accumulation or depletion of Au is determined by surrounding environment. We have analyzed the O_v, polaron, subsurface Ti interstitial effect for negatively charged Au nanoclusters, and the main state of positively charged Au affected by oxygen induced dipole moment.

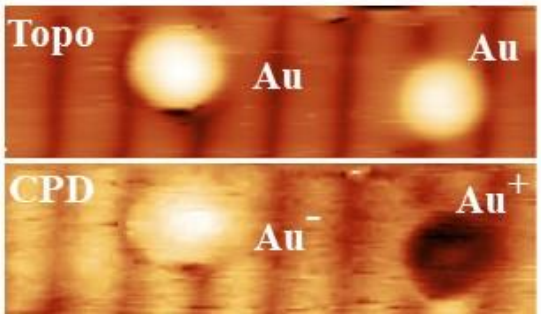

Figure 6.5 Topographic and CPD image of single Au atom on the TiO_2(110) surface.

The surface catalytic reaction can possess a specific charge distribution, which comes from the arrangement of adsorptions and surfaces. Charge transfer between Au and substrate is a premise for surface catalysis due to the distribution of charges affecting the adsorption and binding of reactant molecules. Hence, the charge distribution can significantly determine the active reaction site and selectivity. On the other hand, electric potential different between surface and Au can induce the combination of reactants, affecting catalytic activity. Here, we also display the charge state of trimer Au nanoclusters in Figure 6.6.

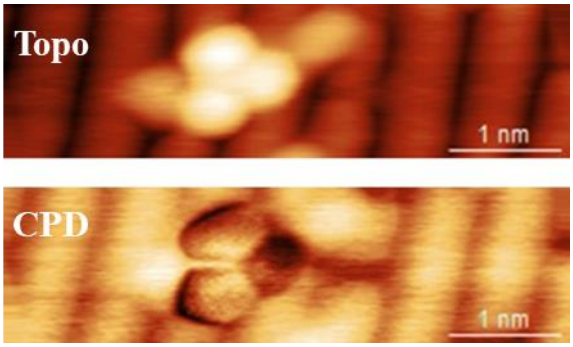

Figure 6.6 Topographic and CPD image of trimer Au on the TiO_2(110) surface.

Comparing with single or dimer Au atoms, the charge states of Au nanoclusters are primarily determined by their metal properties, which make them prone to losing electrons and exhibiting a positively charged state. The active charge state and site for catalytic reaction need to be verified. On the one hand, catalysts often have specific active sites on their surfaces where chemical reactions take place. These sites can have

different charge distributions, making them more or less favorable for particular reaction steps. For example, positively charged sites may enhance the adsorption of negatively charged reactants, while negatively charged sites may favor the adsorption of positively charged species. On the other hand, the charge distribution on the catalyst surface can generate electric fields in the vicinity of the surface. These electric fields can influence the orientation and movement of reactant molecules, promoting specific reaction pathways or affecting the energy barrier for a particular step. We have operated the Au atom by KPFS method to confirm the bonding energy between Au and oxygen, as shown in Figure 6.7.

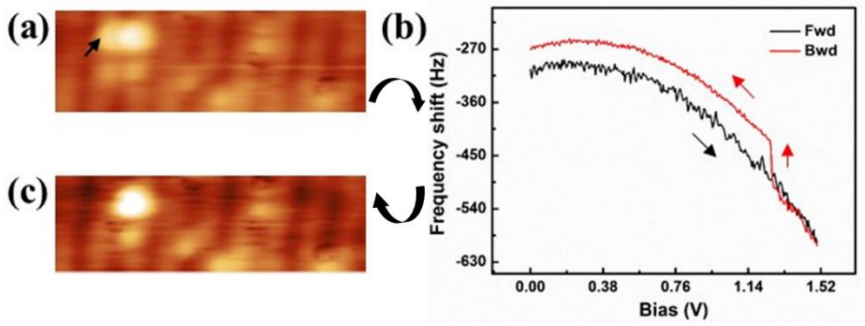

Figure 6.7 Au operation by KPFS method. (a) Before and (c) after applying bias voltage, single Au atom desorbed from the surface. The operated Au is marked by black arrow. And the operation event can be described from bias vs frequency shift curve (b). The jump of the frequency shift represents the process of gold desorption. Size: 6.5 × 1.5 nm^2.

We have chosen the dimer Au atoms in Figure 6.7, which obtain electrons from the subsurface, to explore the interaction between negatively charged Au and surface. By applying a bias voltage above the Au atom marked by black arrow, we found that the Au atom can be easily desorbed from the surface. The desorption event of Au can be described from KPFS curve in Figure 6.7(b), and the frequency shift jump at 1.3 V indicates the desorption of Au atom. We have operated many times, negatively charged Au always desorbs form the surface. The desorption of negatively charged Au implies that the Au atoms occupied by electrons are unstable on the TiO_2 surface. Therefore, this kind of sites is not suitable for surface catalytic reaction. And then, we expose CO on the chamber, detailed process is talked in chapter 5. In this system, CO, O_2 and Au are occupied on the surface. To find the CO oxidation processes, we have operated the CO and O_2, CO and lattice O involving Au, and CO with O_2 involving Au. There are several steps in the CO oxidation reaction. Firstly, CO molecules adsorb onto the TiO_2 surface, forming bonds with the Au atoms. This adsorption is often facilitated by weak interactions, such as van der Waals forces or charge transfer. Then, the adsorbed CO molecules undergo activation, typically by interacting with oxygen species adsorbed on the TiO_2 surface. This interaction can lead to the formation of an intermediate, such as

a surface-bound CO_2 species. The activated CO species reacts with additional oxygen species to form carbon dioxide (CO_2). This reaction may occur through a variety of mechanisms, such as the Langmuir-Hinshelwood mechanism, where two adsorbed species react directly on the catalyst surface. Finally, the produced CO_2 molecules desorb from the TiO_2 surface, releasing the reaction products.

To find the oxidation reaction conditions of CO with oxygen, the experiments are operated at 78 K and the reaction processes can be observed. Because the reaction is not easily to proceed at room temperature, therefore, we observe the reaction at 78 K. Firstly, we choose a single CO with O_{ad} to find the reaction condition on the TiO_2(110) surface as shown in Figure 6.8.

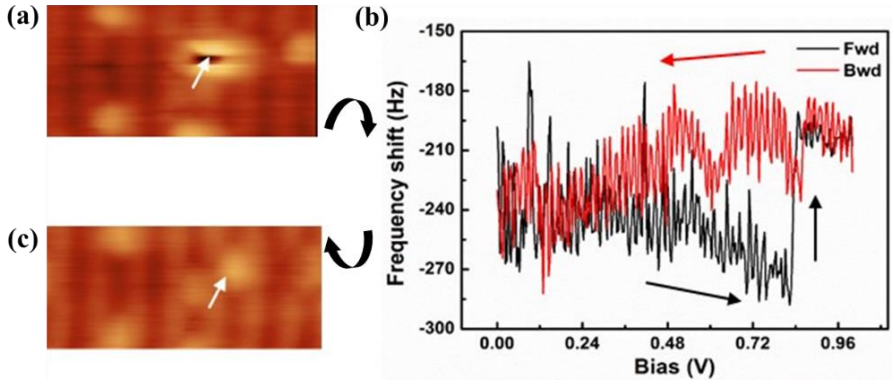

Figure 6.8 Operation of CO with O_{ad} on the TiO_2(110) surface at 78 K.

As shown in Figure 6.8, CO adsorbs on the O_{ad}, and the contrast of CO is dark spot, what have been talked in chapter 5. The topographic image of CO existed with O_{ad} indicates that it is difficult to react between oxygen and CO on the TiO_2(110) surface at 78 K. Then, we apply the bias voltage from 0 - 1 V on top of CO molecule, CO desorbs from the surface, leaving oxygen adatom on the surface. The black curve of bias spectroscopy indicates the bias sweep increases from 0 to 1 V, and jumps around 0.84 V. The desorption event of CO molecule can be described from the jumping of forward bias spectroscopy. In this way, it's difficult to make CO react with oxygen adatom. To avoid the CO desorption, we set the bias sweep point near the CO and oxygen marked by black cross and apply the bias sweep ranging from -0.4 – 2 V to the sample as shown in Figure 6.9(a). After bias sweeping, we can find that oxygen is charged, namely electrons transfer from tip to sample and obtained by oxygen adatoms. After that, we apply second bias sweep at another point as shown in Figure 6.9(c), and the bias voltage is from -0.3 – 1.8 V. The second operation also appears the charging of O_{ad}, which indicates that the reaction of CO and O_{ad} is not feasible at 78 K even applying external energy.

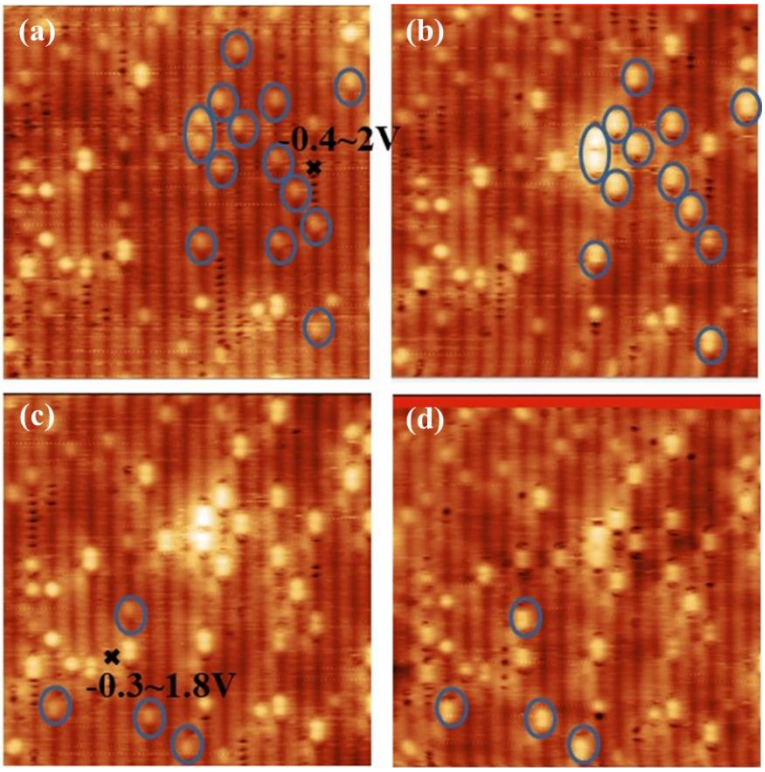

Figure 6.9 Bias voltage sweep operation near the CO and O_{ad} sites.

In the condition of CO with O_{ad} on the TiO_2(110) surface at 78 K, even with the application of external energy, the CO cannot react with oxygen. From the above results, we can conclude that it is difficult for CO and O_{ad} to react at 78 K on TiO_2(110) surface. Therefore, Au is necessary to be introduced for the catalytic system. The Au is deposited on the surface after oxygen exposing, and then CO is exposed to the system at 78 K. CO molecules will dynamically adsorb at the surface as described in chapter 5. The Topographic and CPD images are shown in Figure 6.10.

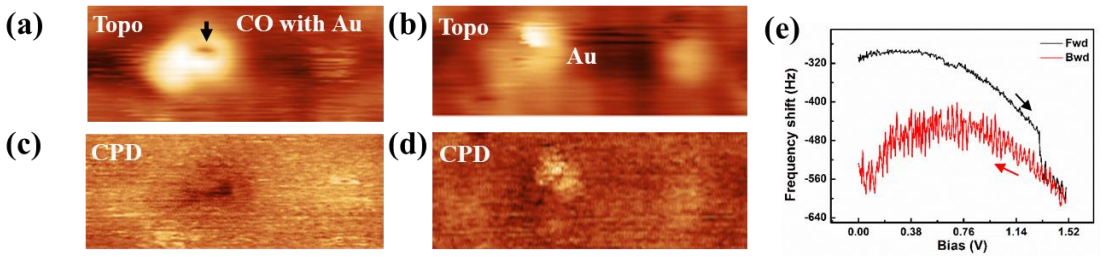

Figure 6.10 The operation of CO molecules and O_{ad} with Au participating in the catalytic system on the TiO_2(110) surface.

Figure 6.10(a) and (c) are topographic and CPD images before operation. CO molecule (shown in dark spot) sticks into a positively charged Au atom. By applying a bias voltage range from 0 – 1.52 V on top of CO molecule, CO reacts with interface oxygen and desorbs from the surface. After reaction, positively charged Au obtain the

electrons change into negatively charged as shown in Figure 6.10(d). And the electron transfer can be described from the jumping of bias spectroscopy in Figure 6.10(e).

6.5 Conclusion

In this chapter, we have achieved the identification of the charge states of Au nanoclusters, which is important for the catalytic reactions of surface reactants. We confirmed that the negatively charged Au nanoclusters are determined by the surface defect O_v and subsurface defect polarons, while positively charged Au nanoclusters are determined by the dipole moment from Au to the oxygen. The charge states identification of the Au nanoclusters can be used for understanding the catalytic reaction processes under which kind of charge transfer. Negatively charged Au nanoclusters were operated; they are easily desorbed from the surface. We conclude that negatively charged Au nanoclusters is unstable for catalytic reactions. Then, comparing with the operation of CO with O_{ad}, operation of CO oxidation under positively charged Au on the TiO_2(110) surface was realized in atomic resolution at 78 K.

Chapter 7 Summary and outlook

7.1 Summary

In this doctoral thesis, I systematically investigated electronic properties of the surface defects and adsorptions, such as oxygen vacancy, hydroxyl, carbon monoxide, and Au nanoclusters on the rutile TiO_2(110) surface by noncontact atomic force microscopy and Kelvin probe force microscopy techniques under ultra-high vacuum condition at 78 K. Because surface defects influence distribution of surface charge, I first systematically identified the surface defects and adsorbates. It is difficult to distinguish oxygen vacancy and hydroxyl species only by topographic image, which induces mistakes for understanding surface reactants adsorption properties. I systematically point out the distinction between oxygen and hydroxyl by combining NC-AFM with KPFM methods, the local contact potential difference of these species can be clear imaged. Besides, I have confirmed that surface defect oxygen vacancy makes surface adsorbates preferred to locate occupy, which indicates defect has strong effect for reactants adsorption. Because CO adsorption is unstable at 78 K, according to our confirmed first result, here, oxygen gas was exposed to the surface for CO adsorption and oxidation reaction. Namely, after oxygen adsorption, CO was exposed to the surface. And CO adsorption properties are further investigated. I found that CO can be pinned at oxygen adatoms sites, and the force measurement on top of CO molecules also indicate strong chemical interaction. Furthermore, to move CO molecules to the active reaction site, I have used oxygen modified tip apex realize two-dimensional movement control of CO molecules. Since CO cannot react with oxygen at 78 K, even when a bias voltage is applied, Au nanoparticles are deposited onto the surface. Au nanoparticles were deposited at low temperature, hence Au nanoparticles with size around 1-3 nm can be obtained. I found that charge states of Au nanoparticles are different due to adsorption environment. The charge states of Au nanoclusters are clearly identified, which is important for understanding the participation of positively or negatively charged Au in the reaction processes of CO oxidation. Through KPFM measurements, I deduce that the negative charge on Au is induced by the charge redistribution of surface and subsurface defects. Additionally, the dipole moment from Au to oxygen induces a positive charge on Au. I observed that the negatively charged Au nanoclusters are easily desorbed from the surface through operating techniques, indicating their instability for catalytic reactions at 78 K. Furthermore, I successfully conducted CO oxidation with oxygen at atomic resolution for the first time at 78 K, involving the participation of positively charged Au nanoparticles. After the reaction,

the positively charged Au obtains electrons and undergoes a change into a negative charge.

7.2 Outlook

This doctoral work provides fundamental research for understanding the properties of surface defects and adsorptions, and operating the catalytic reactions based on the surface catalytic. The future works should be performed in the size effect investigation of Au nanoclusters for charge states and catalytic activity in atomic resolution. And then, designing the reaction sites by operating reactant molecules to suitable active reaction sites.

Appendix

List of main abbreviations

TiO_2	titanium dioxide
CO	carbon monoxide
Au	gold
Ti row	titanium row
O row	oxygen row
OH_t	hydroxyl adsorbed at Ti row
OH_b	hydrogen bonded to bridge oxygen
O_{ad}	oxygen adatom
O_v	oxygen vacancy
SPM	scanning probe microscopy
STM	scanning tunneling microscopy
NC-AFM	noncontact atomic force microscopy
KPFM	Kelvin probe force microscopy
LCPD	local contact potential difference
CPD	contact potential difference
LDOS	local density of state
NPs	nanoparticles
FM mode	frequency modulation mode
AM mode	amplitude modulation mode

References

Chapter 1

[1] E. M. Jones. Chamber process manufacture of sulfuric acid. Ind. Eng. Chem., **1950**, 42, 2208.

[2] B.A. Averill, Moulijn, J., A.van Santen, R. A., Van Leeuwen, P. W. N. W. Catalysis: An Integrated Approach, **1999**, Elsevier, Amsterdam.

[3] Z. Ma, Zaera, F. Heterogeneous Catalysis by Metals. Encyclopedia of Inorganic and Bioinorganic Chemistry, **2006**.

[4] C. Baleizao, Garcia, H. Chiral salen complexes: an overview to recoverable and reusable homogeneous and heterogeneous catalysts. Chem. Rev., **2006**, 106, 3987-4043.

[5] B. Leach. Applied Industrial Catalysis. ISBN 9780124402100, **1983**.

[6] D. Eigler, Schweizer, E. Positioning single atoms with a scanning tunnelling microscope. Nature, **1990**, 344, 524–526.

[7] F. Haber. Chemical warfare. Nature, **1969**. 224: 952.

[8] F. Haber, R. L. Rossignol. The Production of Synthetic Ammonia. Journal of Industrial and Engineering Chemistry, **1913**. 5: 328-331.

[9] G. Centi, E. A. Quadrelli, S. Perathoner. Catalysis for CO_2 conversion: a key technology for rapid introduction of renewable energy in the value chain of chemical industries. Energy & Environmental Science, **2013**, 6(6): 1711-1731.

[10] B. Yilmaz, U. Müller. Catalytic applications of zeolites in chemical industry. Topics in Catalysis, **2009**, 52: 888-895.

[11] J. G. de Vries, S. D. Jackson. Homogeneous and heterogeneous catalysis in industry. Catalysis Science & Technology, **2012**, 2(10): 2009-2009.

[12] P. L. Krapivsky. Kinetics of monomer-monomer surface catalytic reactions. Physical Review A, **1992**, 45(2): 1067.

[13] H. S. Taylor. A theory of the catalytic surface. Proceedings of the Royal Society of London. Series A, Containing Papers of a Mathematical and Physical Character, **1925**, 108(745): 105-111.

[14] G. A. Somorjai, Y. Li. Introduction to surface chemistry and catalysis. John Wiley & Sons, **2010**.

[15] K. W. Kolasinski. Catalytic growth of nanowires: vapor–liquid–solid, vapor–solid–solid, solution–liquid–solid and solid–liquid–solid growth. Current Opinion in Solid State and Materials Science, **2006**, 10(3-4): 182-191.

[16] R. Dittmeyer, K. Svajda, M. Reif. A review of catalytic membrane layers for gas/liquid reactions. Topics in catalysis, **2004**, 29: 3-27.

[17] K. I. Tanaka, A. Ozaki. Acid-base properties and catalytic activity of solid surfaces. Journal of Catalysis, **1967**, 8(1): 1-7.

[18] D. K. Boehme, H. Schwarz. Gas-phase catalysis by atomic and cluster metal ions: the ultimate single-site catalysts. Angewandte Chemie International Edition, **2005**, 44(16): 2336-2354.

[19] M. Anpo, M. Che. Applications of photoluminescence techniques to the characterization of solid surfaces in relation to adsorption, catalysis, and photocatalysis. Advances in catalysis, **1999**, 44: 119-257.

[20] K. Tanabe. Solid acids and bases: their catalytic properties. Elsevier, **2012**.

[21] S. J. Gentry, T. A. Jones. The role of catalysis in solid-state gas sensors. Sensors and Actuators, **1986**, 10(1-2): 141-163.

[22] R. Ciriminna, E. Falletta, C. Della Pina, T. J. Henrique, P. Mario. Industrial applications of gold catalysis. Angewandte Chemie International Edition, **2016**, 55(46): 14210-14217.

[23] M. Okumura, K. Tanaka, A. Ueda, H. Masatake. The reactivities of dimethylgold (III) β-diketone on the surface of TiO_2: A novel preparation method for Au catalysts. Solid State Ionics, **1997**, 95(1-2): 143-149.

[24] W. Keim. Nickel: an element with wide application in industrial homogeneous catalysis. Angewandte Chemie International Edition in English, **1990**, 29(3): 235-244.

[25] J. Heveling. Heterogeneous catalytic chemistry by example of industrial applications. Journal of Chemical Education, **2012**, 89(12): 1530-1536.

[26] J. C. Védrine. Heterogeneous catalysis on metal oxides. Catalysts, **2017**, 7(11): 341.

[27] D. K. Jambhulkar, R. P. Ugwekar, B. A. Bhanvase, D. P. Barai. A review on solid base heterogeneous catalysts: preparation, characterization and applications. Chemical Engineering Communications, **2022**, 209(4): 433-484.

[28] P. L. Gai, E. D. Boyes, S. Helveg, L. Poul. Hansen, G. Suzanne, R. C. Henry. Atomic-resolution environmental transmission electron microscopy for probing gas–solid reactions in heterogeneous catalysis. MRS bulletin, **2007**, 32(12): 1044-1050.

[29] M. D.Ackermann, T. M. Pedersen, B. L. M. Hendriksen, O. Robach, S. C. Bobaru, I. Popa, C. Quiros, H. Kim, B. Hammer, S. Ferrer, and J. W. M. Frenken. Structure and reactivity of surface oxides on Pt (110) during catalytic CO oxidation. Physical review letters, **2005**, 95(25): 255505.

[30] R. Mu, Q. Fu, H. Xu, H. Zhang, Y. Y. Huang, Z. Jiang, S. Zhang, D. L. Tan, X. H Bao. Synergetic effect of surface and subsurface Ni species at Pt−Ni bimetallic catalysts for CO oxidation. Journal of the American Chemical Society, **2011**, 133(6): 1978-1986.

[31] T. Gu, Y. Liu, X. Weng, Z. B. Wu. The enhanced performance of ceria with surface sulfation for selective catalytic reduction of NO by NH_3. Catalysis Communications, **2010**, 12(4): 310-313.

[32] S. Chakrabarti, B. K. Dutta. Photocatalytic degradation of model textile dyes in wastewater using ZnO as semiconductor catalyst. Journal of hazardous materials, **2004**, 112(3): 269-278.

[33] M. Knez, K. Nielsch, L. Niinistö. Synthesis and surface engineering of complex nanostructures by atomic layer deposition. Advanced materials, **2007**, 19(21): 3425-3438.

[34] E. Katz, I. Willner, J. Wang. Electroanalytical and bioelectroanalytical systems based on metal and semiconductor nanoparticles. Electroanalysis: An International Journal Devoted to Fundamental and Practical Aspects of Electroanalysis, **2004**, 16(1-2): 19-44.

[35] M. P. Seah. The quantitative analysis of surfaces by XPS: A review[J]. Surface and Interface Analysis, **1980**, 2(6): 222-239.

[36] H. Ibach, D. L. Mills, Electron Energy Loss Spectroscopy and Surface Vibrations, Academic Press, New York, **1982**.

[37] G. Binnig, H. Rohrer. Scanning tunneling microscopy—from birth to adolescence (Nobel Lecture)[J]. Angewandte Chemie International Edition in English, **1987**, 26(7): 606-614.

[38] J. Sauer. Molecular models in ab initio studies of solids and surfaces: from ionic crystals and semiconductors to catalysts[J]. Chemical Reviews, **1989**, 89(1): 199-255.

[39] G. Binning, C. F. Quate, C. Gerber," Atomic force microscope," Phys. Rev. Lett. **1986**, 56, 930.

[40] S. Morita, F. J. Giessibl, E. Meyer, R. Wiesendanger. Noncontact Atomic Force Microscopy: Springer. **2015**. 3.

[41] Y. J. Li, N. Ozaki, Y. Naitoh, M. Kageshima, Y. Sugawara, C. Hobbs, L. Kantorovich, Origin of p(2×1) Phase on Si(001) by Noncontact Atomic Force Microscopy at 5 K. Phys. Rev. Lett. **2006**. 96. 106104.

Chapter 2

[1] S. E. McNeil. Nanotechnology for the biologist. Journal of leukocyte biology, **2005**, 78(3): 585-594.

[2] S. S. Elnashaie, F. Danafar, H. H. Rafsanjani. Nanotechnology for chemical engineers. Springer Singapore, **2015**.

[3] S. Bayd, M. Adeel, T. Tuccinardi, M. Cordani, F. Rizzolio. The history of

nanoscience and nanotechnology: from chemical–physical applications to nanomedicine. Molecules, **2019**. 25(1), 112.

[4] G. M. Whitesides. Nanoscience, nanotechnology, and chemistry. Small, **2005**, 1(2): 172-179.

[5] F. A. Buot. Mesoscopic physics and nanoelectronics: nanoscience and nanotechnology. Physics Reports, **1993**, 234(2-3): 73-174.

[6] J. Halbritter, G. Repphun, S. Vinzelberg, G. Staikov, W. J. Lorenz. Tunneling mechanisms in electrochemical STM—distance and voltage tunneling spectroscopy. Electrochimica acta, **1995**. 40(10), 1385-1394.

[7] K. Kobayashi, H. Yamada, K. Matsushige. Rev. Sci. Instrum. **2009**, 80, 043708.

[8] E. Meyer. Atomic force microscopy. Progress in surface science, **1992**, 41(1): 3-49.

[9] K. W. Shinato, F. Huang, Y. Jin. Principle and application of atomic force microscopy (AFM) for nanoscale investigation of metal corrosion. Corrosion Reviews, **2020**, 38(5): 423-432.

[10] B. Voigtländer. Atomic force microscopy. Berlin, Germany: Springer, **2019**.

[11] A. Engel, D. J. Müller. Observing single biomolecules at work with the atomic force microscope[J]. Nature structural biology, **2000**, 7(9): 715-718.

[12] C. Roduit, S. Sekatski, G. Dietler, S. Catsicas, F. Lafont, S. Kasas. Stiffness tomography by atomic force microscopy. Biophysical Journal, **2009**. 97(2), 674-677.

[13] X. Zhu, E. Siamantouras, K. K. Liu, X. Liu. Determination of work of adhesion of biological cell under AFM bead indentation. Journal of the mechanical behavior of biomedical materials, **2016**. 56, 77-86.

[14] X. Chen, B. Li, Z. Liao, J. Li, X. Li, J. Yin, W. Guo. Principles and Applications of Liquid-Environment Atomic Force Microscopy. Advanced Materials Interfaces, **2022**. 9(35), 2201864.

[15] A. V. Bolshakova, O. I. Kiselyova, A. S. Filonov, O. Y. Frolova, Y. L. Lyubchenko, I. V. Yaminsky. Ultramicroscopy **2001**, 86, 121-128

[16] Y. F. Dufrêne, T. Ando, R. Garcia, D. Alsteens, D. Martinez-Martin, A. Engel, C. Gerber, D. J. Müller. Imaging modes of atomic force microscopy for application in molecular and cell biology. Nature nanotechnology, **2017**. 12(4), 295-307.

[17] Y. Martin, D. W. Abraham, H. K. Wickramasinghe. High-resolution capacitance measurement and potentiometry by force microscopy. Applied Physics Letters, **1988**, 52(13): 1103-1105.

[18] D. J. Müller, D. Fotiadis, S. Scheuring, S. A. Müller, A. Engel. Electrostatically balanced subnanometer imaging of biological specimens by atomic force microscope. Biophysical journal, **1999**. 76(2), 1101-1111.

[19] J. V. Lauritsen, M. Reichling. Atomic resolution non-contact atomic force microscopy of clean metal oxide surfaces. Journal of Physics: Condensed Matter, **2010**, 22(26): 263001.

[20] F. J. Giessibl. Advances in atomic force microscopy. Reviews of modern physics, **2003**, 75(3): 949.

[21] M. Saint Jean, S. Hudlet, C. Guthmann, J. Berger. Van der Waals and capacitive forces in atomic force microscopies. Journal of Applied Physics, **1996**. 86(9), 5245-5248.

[22] L. Olsson, N. Lin, V. Yakimov, R. Erlandsson. A method for in situ characterization of tip shape in ac-mode atomic force microscopy using electrostatic interaction. Journal of applied physics, **1998**. 84(8), 4060-4064.

[23] F. Albrecht, J. Repp, M. Fleischmann, M. Scheer, M. Ondráček, P. Jelínek. Probing charges on the atomic scale by means of atomic force microscopy. Physical Review Letters, **2015**. 115(7), 076101.

[24] T. Fukuma, K. Kobayashi, H. Yamada, K. Matsushige. Surface potential measurements by the dissipative force modulation method. Review of scientific instruments, **2004**. 75(11), 4589-4594.

[25] J. E. Sader, S. P Jarvis. Accurate formulas for interaction force and energy in frequency modulation force spectroscopy. Applied physics letters, **2004**, 84(10): 1801-1803.

[26] F. J. Giessibl. Atomic resolution on Si (111)-(7× 7) by noncontact atomic force microscopy with a force sensor based on a quartz tuning fork. Applied Physics Letters, **2000**, 76(11): 1470-1472.

[27] N. D. Lang, W. Kohn. Theory of metal surfaces: charge density and surface energy. Physical Review B, **1970**, 1(12): 4555.

[28] K. Kobayashi, H. Yamada, K. Matsushige. Frequency noise in frequency modulation atomic force microscopy. Review of Scientific Instruments, **2009**, 80(4): 043708.

[29] F. J. Giessibl, F. Pielmeier, T. Eguchi, T. An, Y. Hasegawa. Comparison of force sensors for atomic force microscopy based on quartz tuning forks and length-extensional resonators. Physical Review B, **2011**. 84(12), 125409.

[30] D. Tabor, R. H. S. Winterton. The direct measurement of normal and retarded van der Waals forces. Proceedings of the Royal Society of London. A. Mathematical and Physical Sciences, **1969**, 312(1511): 435-450.

[31] N. A. Burnham, R. J. Colton. Measuring the nanomechanical properties and surface forces of materials using an atomic force microscope. Journal of Vacuum Science & Technology A: Vacuum, Surfaces, and Films, **1989**, 7(4): 2906-2913.

[32] S. Morita, F. J. Giessibl, E. Meyer, R. Wiesendanger. (Eds.). Noncontact Atomic Force Microscopy: **2015**. Volume 3. Springer.

[33] W. Melitz, J. Shen, A. C. Kummel, S. Lee. Kelvin probe force microscopy and its application. Surf. Sci. Rep. **2011**, 66, 1.

[34] G. H. Enevoldsen, T. Glatzel, M. C. Christensen, J. V. Lauritsen, F. Besenbacher.

Atomic scale Kelvin probe force microscopy studies of the surface potential variations on the TiO_2(110) surface. Phys. Rev. Lett. **2008**, 100, 236104.

[35] F. Bocquet, L. Nony, C. Loppacher, T. Glatzel. Analytical approach to the local contact potential difference on (001) ionic surfaces: Implications for Kelvin probe force microscopy. Phys. Rev. B. **2008**, 78, 035410.

[36] S. Kitamura, M. Iwatsuki, M. High-resolution imaging of contact potential difference with ultrahigh vacuum noncontact atomic force microscope. Appl. Phys. Lett. **1998**, 72, 3154- 3156.

[37] A. Kikukawa, S. Hosaka, R. Imura. Silicon pn junction imaging and characterizations using sensitivity enhanced Kelvin probe force microscopy. Appl. Phys. Lett. **1995**, 66, 3510-3512.

[38] Y. Sugawara, L. Kou, Z. M. Ma, T. Kamijo, Y. Naitoh, Y. J. Li. High potential sensitivity in heterodyne amplitude-modulation Kelvin probe force microscopy. Appl. Phys. Lett. **2012**, 100, 223104.

[39] Z. M. Ma, L. L. Kou, Y. Naitoh, Y. J. Li, Y. Sugawara. The stray capacitance effect in Kelvin probe force microscopy using FM, AM and heterodyne. Nanotechnology. **2013**, 24, 225701.

[40] L. Kelvin, "Contact electricity of metals", Philos. Mag., 46: p. 82 **1897**.

Chapter 3

[1] U. Diebold. The Surface Science of Titanium Dioxide. Surf. Sci. Rep. **2003**, 48, 53-229.

[2] F. A. Grant. Properties of rutile (titanium dioxide). Reviews of Modern Physics, **1959**, 31(3): 646.

[3] M. Landmann, E. Rauls, W. G. Schmidt. The electronic structure and optical response of rutile, anatase and brookite TiO_2. Journal of physics: condensed matter, **2012**, 24(19): 195503.

[4] M. Ramamoorthy, D. Vanderbilt, R. D. King-Smith. First-principles calculations of the energetics of stoichiometric TiO_2 surfaces. Phys. Rev. B. **1994**, 49, 23, 16721.

[5] P. W. Tasker. The stability of ionic crystal surfaces. Journal of Physics C: Solid State Physics **1979**, 12, 22, 4977.

[6] J. P. LaFemina. Total energy computations of oxide surface reconstructions. Crit. Rev. Surf. Chem. **1994**, 3, 3/4, 297-386.

[7] Y. W. Chung, W. J. Lo, G. A. Somorjai. Low energy electron diffraction and electron spectroscopy studies of the clean (110) and (100) titanium dioxide (rutile) crystal surfaces. Surface Science, **1977**, 64(2): 588-602.

[8] R. Nakamura, N. Ohashi, A. Imanishi, T. Osawa, Y. Matsumoto, H. Koinuma, Y. Nakato. Crystal-face dependences of surface band edges and hole reactivity, revealed

by preparation of essentially atomically smooth and stable (110) and (100) n-TiO_2 (rutile) surfaces. The Journal of Physical Chemistry B, **2005**. 109(5), 1648-1651.

[9] D. A. H. Hanaor, C. C. Sorrell. Review of the anatase to rutile phase transformation. Journal of Materials science, **2011**, 46: 855-874.

[10] R. D. Shannon, J. A. Pask. Kinetics of the anatase-rutile transformation. Journal of the American Ceramic Society, **1965**, 48(8): 391-398.

[11] B. Choudhury, A. Choudhury. Oxygen defect dependent variation of band gap, Urbach energy and luminescence property of anatase, anatase–rutile mixed phase and of rutile phases of TiO2 nanoparticles. Physica E: Low-Dimensional Systems and Nanostructures, **2014**, 56: 364-371.

[12] D. T. Cromer, K. Herrington. The structures of anatase and rutile. Journal of the American Chemical Society, **1955**, 77(18): 4708-4709.

[13] M. A. Henderson. Mechanism for the bulk-assisted reoxidation of ion sputtered TiO_2 surfaces: diffusion of oxygen to the surface or titanium to the bulk? Surf. Sci. **1995**, 343, 1- 2, 1156-1160.

[14] P. J. D. Lindan, N. M. Harrison. First-principles spin-polarized calculations on the reduced and reconstructed TiO_2(110) surface. Phys. Rev. B. **1997**, 55, 23, 15919.

[15] J. M. Pan, B. L Maschhoff, U. Diebold, T. E. Madey. Interaction of water, oxygen, and hydrogen with TiO_2(110) surfaces having different defect densities. Journal of Vacuum Science & Technology A: Vacuum, Surfaces, and Films. **1992**, 10, 4, 2470-2476.

[16] E. Cho, S. Han, H. S. Ahn, K. R. Lee, C. S. Hwang. First-principles study of point defects in rutile TiO_{2-x}. Physical Review B, **2006**. 73(19), 193202.

[17] K. Morita, T. Shibuya, K. Yasuoka. Stability of excess electrons introduced by Ti interstitial in rutile TiO_2(110) surface. The Journal of Physical Chemistry C, **2017**, 121(3): 1602-1607.

[18] L. Cheng, W. Liu, C. Yang, T. Huang, Z. G. Hou, M. Tan. A neural-network-based controller for piezoelectric-actuated stick–slip devices. IEEE Transactions on Industrial Electronics, **2017**. 65(3), 2598-2607.

[19] Y. Zhang, Y. Peng, Z. Sun, H. Yu. A novel stick–slip piezoelectric actuator based on a triangular compliant driving mechanism. IEEE Transactions on Industrial Electronics, **2018**. 66(7), 5374-5382.

[20] C. A. Putman, B. G. De Grooth, N. F. Van Hulst, J. Greve. A detailed analysis of the optical beam deflection technique for use in atomic force microscopy. Journal of Applied Physics, **1992**. 72(1), 6-12.

[21] T. Fukuma, M. Kimura, K. Kobayashi, K. Matsushige, H. Yamada. Development of low noise cantilever deflection sensor for multienvironment frequency-modulation atomic force microscopy. Review of Scientific Instruments, **2005**. 76(5), 053704.

[22] S. Moreno-Flores, J. L. Toca-Herrera. Hybridizing surface probe microscopies: Toward a full description of the meso-and nanoworlds. CRC Press, **2012**.

Chapter 4

[1] R. Schaub, N. Thostrup, N. Lopes, E. Lagsgaard, I. Stensgaard, J. K. Norskov, F. Besenbacher. Oxygen vacancies as active sites for water dissociation on rutile TiO_2(110). Phys. Rev. Lett. **2001**, 87, 266104.

[2] N. G. Petrik, G. A. Kimmel. Reaction Kinetics of Water Molecules with Oxygen Vacancies on Rutile TiO_2(110). J. Phys. Chem. C. **2015**, 119, 23059-23067.

[3] U. Diebold. The surface science of titanium dioxide. Surf. Sci. Rep. **2003**, 48, 53-229.

[4] O. Björneholm, M. H. Hansen, A. Hodgson, L. M. Liu, D. T. Limmer, A. Michaelides, P. Pedevilla, J. Rossmeisl, H. Shen, G. Tocci. Water at interfaces. Chem. Rev. **2016**, 116, 7698-7726.

[5] R. T. Mu, Z. J. Zhao, Z. Dohnálek, J. L. Gong. Structural motifs of water on metal oxide surfaces. Chem. Soc. Rev. **2017**, 46, 1785-1806.

[6] H. J. Shin, J. J. Jung, K. Motobayashi, S. Yanagisawa, Y. Morikawa, Y. Kim, M. Kawai. State-selective dissociation of a single water molecule on an ultrathin MgO film. Nat. Mater. **2010**, 9, 442-447.

[7] L. R. Merte, G. W. Peng, R. Bechstein, F. Rieboldt, C. A. Farberow, L. C. Grabow, W. Kudernatsch, S. Wendt, E. Lagsgaard, M. Mavrikakis, F. Besenbacher. Water-mediated proton hopping on an iron oxide surface. Science **2012**, 336, 889-893.

[8] S. Wendt, J. Matthiesen, R. Schaub, E. K. Vestergaard, E. Lagsgaard, F. Besenbacher, B. Hammer. Formation and splitting of paired hydrogen groups on reduced TiO_2(110). Phys. Rev. Lett. **2006**, 96, 066107.

[9] Y. J. Li, H. F. Wen, Q. Z. Zhang, Y. Adachi, E. Arima, Y. Kinoshita, H. Nomura, Z. M. Ma, L .L. Kou, Y. Tsukuda, Y. Naitoh, Y. Sugawara, R. Xu, Z. H. Cheng. Stable contrast mode on TiO_2 (110) surface with metal-coated tips using AFM. Ultramicroscopy. **2018**, 191, 51-55.

[10] Q. Z. Zhang, Y. J. Li, H. F. Wen, Y. Adachi, M. Miyazaki, Y. Sugawara, R. Xu, Z. H. Cheng, J. Brndiar, L. Kantorovich, I. Štich. Measurement and manipulation of the charge state of an adsorbed oxygen adatom on the rutile TiO_2 (110)-1×1 surface by nc-AFM and KPFM. J. Am. Chemi. Soc. **2018**, 140, 15668-15674.

[11] Y. Adachi, H. F. Wen, Q. Z. Zhang, M. Miyazaki, Y. Sugawara, H. Q. Sang, J. Brndiar, L. Kantorovich, I. Štich, Y. J. Li. Tip-induced control of charge and molecular bonding of oxygen atoms on the rutile TiO_2(110) surface with atomic force microscopy. ACS nano **2019**, 13, 6917-6924.

[12] H. F. Wen, H. Q. Sang, Y. Sugawara, Y. J. Li. Dynamic behavior of OH and its

atomic contrast with O adatom on the Ti site of TiO_2(110) at 78 K by atomic force microscopy imaging. Appl. Phys. Lett. **2020**, 117, 051602.

[13] H. F. Wen, Y. Adachi, Q. Z. Zhang, M. Miyazaki, Y. Sugawara, Y. J. Li. Identification of atomic defects and adsorbate on rutile TiO_2(110)-(1×1) surface by atomic force microscopy. J. Phys. Chem. C. **2019**, 123, 25756-25760.

[14] Z. Zhang, O. Bondarchuk, B. D. Kay, J. M. White, J. M, Z. Dohnalek. Imaging water dissociation on TiO_2(110): Evidence for inequivalent geminate OH groups. The Journal of Physical Chemistry B, **2006**. 110(43), 21840-21845.

[15] S. C. Li, Z. Zhang, D. Sheppard, B. D. Kay, J. M. White, Y. Du, I. Lyubinetsky, G. Henkelman, Z. Dohnálek. Intrinsic diffusion of hydrogen on rutile TiO_2(110). Journal of the American Chemical Society, **2008**. 130(28), 9080-9088.

[16] A. Yurtsever, D. Fernandez-T, C. González, P. Jelínek, P. Pou, Y. Sugimoto, M. Abe, R. Pérez, S. Morita. Understanding image contrast formation in TiO_2 with force spectroscopy. Phys. Rev. B. **2012**, *85*, 125416.

[17] M. Wagner, B. Meyer, M. Setvin, M. Schmid, U. Diebold. Direct assessment of the acidity of individual surface hydroxyls. Nature, **2021**. 592(7856), 722-725.

[18] A. Shiotari, Y. Sugimoto. Ultrahigh-resolution imaging of water networks by atomic force microscopy. Nature communications, **2017**, 8(1): 14313.

[19] J. V. Lauritsen, A. S. Foster, G. H. Olesen, M. C. Christensen, A. Kühnle, S. Helveg, R. J. Rostrup-N, B. S. Clausen, M. Reichling, F. Besenbacher. Chemical identification of point defects and adsorbates on a metal oxide surface by atomic force microscopy. Nanotechnology. **2006**, 17, 3436.

[20] S. Fatayer, B. Schuler, W. Steurer, I. Scivetti, J. Repp, L. Gross, M. Persson, G. Meyer. Reorganization energy upon charging a single molecule on an insulator measured by atomic force microscopy. Nature nanotechnology, **2018**, 13(5): 376-380.

[21] Y. Adachi, H. Q. Sang, Y. Sugawara, Y. J. Li. Single hydrogen atom manipulation for reversible deprotonation of water on a rutile TiO_2(110) surface. Communications Chemistry, **2021**. 4. 5.

Chapter 5

[1] G. A. Somorjai, New model catalysts (platinum nanoparticles) and new techniques (SFG and STM) for studies of reaction intermediates and surface restructuring at high pressures during catalytic reactions. Appl. Surf. Sci. **1997**. 121. 1-19.

[2] Q. Z. Zhang, Y. J. Li, H. F. Wen, Y. Adachi, M. Miyazaki, Y. Sugawara, R. Xu, Z. H. Cheng, J. Brndiar, L. Kantorovich, I. Štich, Measurement and manipulation of the charge state of an adsorbed oxygen adatom on the rutile TiO_2(110)-1×1 surface by nc-AFM and KPFM. J. Am. Chem. Soc. **2018**. 140. 15668-15674.

[3] Y. Adachi, H. F. Wen, Q. Z. Zhang, M. Miyazaki, Y. Sugawara, H. Q. Sang, J. Brndiar, L. Kantorovich, I. Štich, Y. J. Li, Tip-induced control of charge and molecular bonding of oxygen atoms on the rutile TiO_2(110) surface with atomic force microscopy. ACS. nano. 2019. 13. 6917-6924.

[4] J. Q. Ren, J. S. Zhao, Z. G. Dong, P. K. Liu, Molecular dynamics study on the mechanism of AFM-based nanoscratching process with water-layer lubrication. Appl. Surf. Sci. **2015**. 346. 84-98.

[5] I. Otsuka, M. Yaoita, M. Higano, S. Nagashima, R. Kataoka, Tapping mode AFM study on the surface dynamics of a single glucose oxidase molecule on a Au(111) surface in water with implication for a surface-induced unfolding pathway. Appl. Surf. Sci. **2004**. 235 1-2: 188-196.

[6] K. M. Gameel, I. M. Sharafeldin, A. U. Abourayya, A. H. Biby, N. K. Allam, Unveiling CO adsorption on Cu surfaces: new insights from molecular orbital principles. Phys. Chem. Chem. Phys. **2018**. 20. 25892-25900.

[7] Ke. Wang, S. H. He, Y. Z. Lin, X. Chen, W. X. Dai, X. Z. Fu, Photo-enhanced thermal catalytic CO_2 methanation activity and stability over oxygen-deficient Ru/TiO_2 with exposed TiO_2{001} facets: Adjusting photogenerated electron behaviors by metal-support interactions. Chiese. J. Catal. **2022**. 43. 391-402.

[8] G. Cheng, Z. H. Cai, X. J. Song, X. Chen, W. X. Dai, X. Z. Fu, Visible light enhanced thermocatalytic CO+NO reaction over metastable $NiCo_2O_4$ catalyst. Appl. Catal. B-Environ. **2022**. 304. 120988.

[9] Q. Z. Li, C. J. Wu, K. Wang, X. X. Wang, X. Chen, W. X. Dai, X. Z. Fu, Comparison of the catalytic performance of Au/TiO_2 prepared by in situ photodeposition and deposition precipitation methods for CO oxidation at room temperature under visible light irradiation. Catal. Sci. Technol. **2022**. 12. 237-249.

[10] I. H. Kim, H. O. Seo, E. J. Park, S. W. Han, Y. D. Kim, Low temperature CO oxidation over iron oxide nanoparticles decorating internal structures of a mesoporous alumina. Sci. Rep. **2017**. 7. 1-11.

[11] K. R. Harikumar, C. N. R. Rao, Interaction of CO with CuZnO catalyst surfaces prepared in situ in the electron spectrometer: evidence for CO_2^- and related species relevant to methanol synthesis. Appl. Surf. Sci. **1998**. 125. 245-249.

[12] A. D. Allian, K. Takanabe, K. L. Fujdala, X. H. Hao, T. J. Truex, J. Cai, C. Buda, M. Neurock, E. Iglesia, Chemisorption of CO and mechanism of CO oxidation on supported platinum nanoclusters. J. Am. Chem. Soc. **2011**. 133. 4498-4517.

[13] Y. Zhou, Z. Y. Wang, C. J. Liu, Perspective on CO oxidation over Pd-based catalysts. Catal. Sci. Techol. **2015**. 5. 69-81.

[14] Z X. Li, H. L. Wang, X. X. Wu, Q. L. Ye, X. T. Xu, B. Li, F. Wang. Novel synthesis and shape-dependent catalytic performance of Cu-Mn oxides for CO oxidation. Appl. Surf. Sci. **2017**. 403. 335-341.

[15] Z. H. Li, Y. Geng, L. Ma, X. Y. Chen, J. H. Li, H. Z. Chang, J. W. Schwank, Catalytic oxidation of CO over Pt/Fe_3O_4 catalysts: Tuning O_2 activation and CO adsorption. Front. Env. Sci. Eng. **2020**.14.1-9.

[16] A. J. Therrien, A. J. R. Hensley, M. D. Marcinkowski, R. Q. Zhang, F. R. Lucci, B. J. M. Coughlin, A. C. Schilling, J-S. McEwen, E. C. H. Sykes, An atomic-scale view of single-site Pt catalysis for low-temperature CO oxidation. Nat. Catal. **2018**. 1. 92-198.

[17] B. Huang, H. Kobayashi, T. Yamamoto, T. Toriyama, S. Matsumura, Y. Nishida, K. Sato, K. Nagaoka, M. Haneda, W. Xie, Y. Nanba, M. Koyama, F. L. Wang, S. Kawaguchi, Y. Kubota, H. Kitagawa, A CO adsorption site change induced by copper substitution in a ruthenium catalyst for enhanced CO oxidation activity. Angew. Chem. **2019**. 131. 2252-2257.

[18] J. Hulva, M. Meier, R. Bliem, Z. Jakub, F. Kraushofer, M. Schimid, U. Diebold, C. Franchini, G. S. Parkinson, Unraveling CO adsorption on model single-atom catalysts. Sci. **2021**. 371. 375-379.

[19] T. M. Hafshejani, W. J. Wang, J. Heggemann, A. Nefedov, S. Herssler, Y. M. Wang, P. Rahe, P. Thissen, C. Wöll, CO adsorption on the calcite (10.4) surface: a combined experimental and theoretical study. Phys. Chem. Chem. Phys. **2021**. 23. 7696-7702.

[20] X. H. Yu, X. M. Zhang, L. X. Jin, G. Feng, CO adsorption, oxidation and carbonate formation mechanisms on Fe_3O_4 surfaces. Phys. Chem. Chem. Phys. **2017**. 19. 17287-17299.

[21] F. Y. Hu, R. P. Ye, Z. H. Liu, R. B. Zhang, G. Feng, Structure–activity relationship of Ni-based catalysts toward CO_2 methanation: recent advances and future perspectives. Energ. Fuel. **2021**. 36. 156-169.

[22] J. Oh, H. Lim, R. Arafune, J. Jung, M. Kawai, Y. Kim, Lateral hopping of CO on Ag(110) by multiple overtone excitation. Phys. Rev. Lett. **2016**. 116. 056101.

[23] M. Emmrich, M. Schineiderbauer, F. Huber, A. J. Weymouth, N. Okabayashi, F. J. Giessibl, Force field analysis suggests a lowering of diffusion barriers in atomic manipulation due to presence of STM tip. Phys. Rev. Lett. **2015**. 114. 146101.

[24] T. Komeda, Y. Kim, M. Kawai, B. N. J. Persson, H. Ueba, Lateral hopping of molecules induced by excitation of internal vibration mode. Sci. **2002**. 295. 2055-2058.

[25] C. Zaum, K. Morgenstern, Experimental evidence for a three-body interaction between diffusing CO molecules. Nano. Lett. **2016**. 16. 3001-3004.

[26] C. Cheng, Y. Zhu, W. H. Fang, R. Long, O. V. Prezhdo, CO Adsorbate promotes polaron photoactivity on the reduced rutile TiO_2(110) surface. J. Am. Chem. Soc. **2022**. 2. 234-245.

[27] X. Li, T. Haunold, S. Werkovits, L. D. Marks, P. Blaha, G. Rupprechter, CO adsorption and disproportionation on smooth and defect-rich Ir(111). J. Phys. Chem.

C. **2022**. 126. 6578-8589.

[28] Y. Adachi, Y. Sugawara, Y. J. Li, Probing CO on a rutile TiO_2(110) surface using atomic force microscopy and Kelvin probe force microscopy. Nano. Res. **2022**. 15. 1909-1915.

[29] X. J. Wang, C. Y. Jia, E. Sharman, G. Z. Zhang, X. Li, J. Jiang, Carbon monoxide oxidation promoted by surface polarization charges in a CuO/Ag Hybrid catalyst. Sci. Rep. **2020**. 10. 1-9.

[30] Y. G. Du, N. A. Deskins, Z. R. Zhang, Z. Dohnalek, M. Dupuis, I. Lyubinetsky, Formation of O adatom pairs and charge transfer upon O_2 dissociation on reduced TiO_2(110). Phys. Chem. Chem. Phys. **2010**. 12. 6337-6344.

[31] H. Xu, S. Y. Tong, Interaction of O_2 with reduced rutile TiO_2(110) surface. Surf. Sci. **2013**. 610. 33-41.

[32] M. D. Rasmussen, L. M. Molina, B. Hammer, Adsorption, diffusion, and dissociation of molecular oxygen at defected TiO_2(110): A density functional theory study. J. Chem. Phys. **2004**. 120. 988-997.

[33] H. P. Pinto, G. H. Enevoldsen, F. Besenbacher, J. V. Lauritsen, A. S. Foster, The role of tip size and orientation, tip–surface relaxations and surface impurities in simultaneous AFM and STM studies on the TiO_2(110) surface. Nanotechnology. 2009. 20. 264020.

[34] Y. J. Li, H. F. Wen, Q. Z. Zhang, Y. Adachi, E. Arima, Y. Kinoshita, H. Nomura, Z. M. Ma, L. L. Kou, Y. Tsukuda, Y. Naitoh, Y. Sugawara, R. Xu, Z. H. Cheng, Stable contrast mode on TiO_2(110) surface with metal-coated tips using AFM. Ultramicroscopy. **2018**. 191. 51-55.

[35] N. G. Petrik, R. M, A. Dahal, Z. T. Wang, I. Lyubinetsky, G. A. Kimmel, Diffusion and photon-stimulated desorption of CO on TiO_2(110). J. Phys. Chem. C. **2018**. 122. 15382-15389.

[36] A. Schwarz, A. Köhler, J. Grenz, R. Wiesendanger, Detecting the dipole moment of a single carbon monoxide molecule. Appl. Phys. Lett. **2014**. 105. 011606.

[37] J. A. Stroscio, R. J. Celotta, Controlling the dynamics of a single atom in lateral atom manipulation. Sci. 306 (2004) 242-247. doi: 10.1126/science.1102370.

[38] J. A. Stroscio, D. M. Eigler, Atomic and molecular manipulation with the scanning tunneling microscope. Sci. **1991**. 254. 1319-1326.

[39] A. Zangwill, Physics at Surfaces. Cambridge University Press: Cambridge, **1988**. 204-231.

[40] K. Oura, V. G. Lifshits, A. Saranin, A. V. Zotov, Katayama M, Surface science an introduction. Springer: New York, **2003**. 325-356.

[41] M. Reticcioli, M. Setvin, M. Schmid, U. Diebold, C, Franchini. Formation and dynamics of small polarons on the rutile TiO_2(110) surface. Phys. Rev. B. 2018. 98. 045306.

[42] M. Reticcioli, U. Diebold, G. Kresse, C. Franchini, Small polarons in transition metal oxides. Handbook of Materials Modeling: Applications: Current and Emerging Materials, **2020**. 1035-1073.

[43] D. Mombrú, M. Romero, M. G. Sandoval, R. Faccio, Á. W. Mombrú, Role of surface defects on the adsorption of poly (9-vinylcarbazole) on TiO_2 using the monomer as a donor: acceptor model. Appl. Surf. Sci. **2019**. 487. 1104-1110.

[44] M. Miyazaki, Y. Sugawara, Y. J. Li, Charge behavior of terminal hydroxyl on rutile TiO_2(110). Langmuir. **2021**. 37. 10588-10593.

[45] Q. Z. Zhang, H. F. Wen, Y. Adachi, M. Miyazaki, Y. Sugawara, R. Xu, Z. H. Cheng, Y. J. Li, Electrical engineering of the oxygen adatom and vacancy on rutile TiO_2(110) by atomic force microscopy at 78 K. J. Phys. Chem. C. **2019**. 123. 28852-28858.

[46] J. T. Li, W. D. Schneider, R. Berndt, Low-temperature manipulation of Ag atoms and clusters on a Ag(110) surface. Appl. Phys. A. **1998**. 66. 675-S678.

[47] M. Gajdoš, A. Eichier; J. Hafner, G. Meyer, K. H. Rieder, CO adsorption on a Cu(211) surface: First-principle calculation and STM study. Phys. Rev. B. **2005**. 71. 035402.

[48] Y. Sugimoto, T. Namikawa, K. Miki, M. Abe, S. Morita, Vertical and lateral force mapping on the Si(111)-(7×7) surface by dynamic force microscopy. Phys. Rev. B. **2008**. 77. 195424.

[49] J. E. Sader, Accurate formulas for interaction force and energy in frequency modulation force spectroscopy. Appl. Phys. Lett. **2004**. 84. 1801-1803.

Chapter 6

[1] S. Mitchell, J. Pérez-Ramírez, Single atom catalysis: a decade of stunning progress and the promise for a bright future, Nat. Commun. **2020**. 11. 4302-4304.

[2] X. F. Yang, A. Q. Wang, B. T. Qiao, J. Li, J. Y. L, T. Zhang, Single-atom catalysts: a new frontier in heterogeneous catalysis, Accounts. Chem. Res. 2013. 46. 1740-1748.

[3] Q. Zhang, J. Guan, Applications of single-atom catalysts, Nano. Res. 2022. 15. 38-70.

[4] G. Kyriakou, M. B. Boucher, A. D. Jewell, E. A. Lewis, T. J. Lawton, A. E. Baber, H. L. Tierney, M. F-Stephanopoulos, E. C. H. Skyes, Isolated metal atom geometries as a strategy for selective heterogeneous hydrogenations, Sci. 2012. 335. 1209-1212.

[5] J. L. Zhang, J. Y. Liu, L. F. Xi, Y. F. Yu, N. Chen, S. H. Sun, W. C. Wang, K. M. Lange, B. Zhang, Single-atom Au/NiFe layered double hydroxide electrocatalyst: probing the origin of activity for oxygen evolution reaction, J. Am. Chem. Soc. 2018. 140. 3876-3879.

[6] K. Qi, X. Q. Cui, L. Gu, S. S. Yu, X. F. Fan, M. C. Luo, S. Xu, N. B. Li, L. R.

Zheng, Q. H. Zhang, J. Y. Ma, Y. Gong, F. Lv, K. Wang, H. H. Huang, W. Zhang, S. J. Guo, W. T. Zheng, P. Liu, Single-atom cobalt array bound to distorted 1T MoS_2 with ensemble effect for hydrogen evolution catalysis, Nat. Commun. 2019. 10. 5231-5240.

[7] H. S. Wei, Y. J. Ren, A. Q. Wang, X. Y. Liu, X. Liu, L. L. Zhang, S. Miao, L. Li, J. Y. Liu, J. H. Wang, G. F. Wang, D. S. Su, T. Zhang, Remarkable effect of alkalis on the chemoselective hydrogenation of functionalized nitroarenes over high-loading Pt/FeO_x catalysts, Chem. Sci. 2017. 8. 5126-5131.

[8] P-W. Yu, S. Elmas, T. Roman, X. Pan, Y. T. Yin, C. T. Gibson, G. G. Andersson, M. R. Andersson, Highly active platinum single-atom catalyst grafted onto 3D carbon cloth support for the electrocatalytic hydrogen evolution reaction, Appl. Surf. Sci. 2022. 595. 153480.

[9] F. Solymosi, Importance of the electric properties of supports in the carrier effect, Catal. Rev. 1968. 1. 233–255.

[10] X. C. Zhou, W. L. Xu, G. K. Liu, D. Panda, P. Chen, Size-dependent catalytic activity and dynamics of gold nanoparticles at the single-molecule level, J. Am. Chem. Soc. 2010. 132. 138-146.

[11] Y. Han, C. J. Liu, Q. F. Ge, Interaction of Pt clusters with the anatase TiO_2(101) surface: A first principles study, J. Phys. Chem. B. 2006. 110. 7463-7472.

[12] X. C. Zhou, W. L. Xu, G. K. Liu, D. Panda, P. Chen, Size-dependent catalytic activity and dynamics of gold nanoparticles at the single-molecule level, J. Am. Chem. Soc. 2010. 132. 138-146.

[13] L. Dong, L. L. Yin, Q. N. Xia, X. H. Liu, X. Q. Gong, Y. Q. Wang, Size-dependent catalytic performance of ruthenium nanoparticles in the hydrogenolysis of a β-O-4 lignin model compound, Catal. Sci. Technol. 2018. 8. 735-745.

[14] S. W. Cao, F. Tao, Y. Tang, Y. T. Li, J. G. Yu, Size-and shape-dependent catalytic performances of oxidation and reduction reactions on nanocatalysts, Chem. Soc. Rev. 2016. 45. 4747-4765.

[16] C. Liang, J. Y. Cheong, G. Sitaru, S. Rosenfeldt, A. S. Schenk, S. Gekle, II-D. Kim, A. Greiner, Size-Dependent Catalytic Behavior of Gold Nanoparticles, Adv. Mater. Interfaces. 2022. 9. 1-8.

[17] D . T. Boyle, A. W. Jeremy, R. M. Palomino, V. H. Lam, D. A. Schlosser, W. J. Andahazy, C. Z. Stopak, D. J. Stacchiola, J. A. Rodriguez, A. E. Baber, Elucidation of Active Sites for the Reaction of Ethanol on TiO_2/Au(111), J. Phys. Chem. C. 2017. 121. 7794−7802.

[18] I. X. Green, W. J. Tang, M. Neurock, J. T. Yates Jr, Insights into Catalytic Oxidation at the Au/TiO_2 Dual Perimeter Sites, Acc. Chem. Res. 2014. 47. 805−815.

[19] A. Mellor, A. Wilson, C. L. Pang, C. M. Yim, F. Maccherozzi, S. S. Dhesi, C. A. Muryn, H. Idriss, G. Thornton, Photoemission Core Level Binding Energies from

Multiple Sized Nanoparticles on the Same Support: TiO_2(110)/Au, J. Chem. Phys. 2020. 152. 1-7.

[20] M. S. Chen, D. W. Goodman, The Structure of Catalytically Active Gold on Titania, Sci. 2004. 306. 252−255.

[21] U. Diebold, The surface science of titanium dioxide, Surf. Sci. Rep. 2003. 48. 53-229.

[22] H. F. Wen, Y. Adachi, Q. Z. Zhang, M. Miyazaki, Y. Sugawara, Y. J. Li, Identification of Atomic Defects and Adsorbate on Rutile TiO_2(110)-(1×1) Surface by Atomic Force Microscopy, J. Phys. Chem. C. 2019. 123. 25756–25760.

[23] Q. Z. Zhang, Y. J. L., H. F. Wen, Y. Adachi, M. Miyazaki, Y. Sugawara, R. Xu, Z. H. Cheng, J. Brndiar, L. Kantorovich, I. Štich, Measurement and manipulation of the charge state of an adsorbed oxygen adatom on the rutile TiO_2(110)-1×1 surface by nc-AFM and KPFM, J. Am. Chem. Soc. 2018. 140. 15668–15674.

[24] Y. Adachi, H. F. W., Q. Z. Zhang, M. Miyazaki, Y. Sugawara, H. Q. Sang, J. Brndiar, L. Kantorovich, I. Štich, Y. J. Li, Tip-induced control of charge and molecular bonding of oxygen atoms on the rutile TiO_2(110) surface with atomic force microscopy, ACS Nano. 2019. 13. 6917-6924.

[25] Y. G. Du, N. A. Deskins, Z. R. Zhang, Z. Dohnalek, M. Dupuis, I. Lyubinetsky, Formation of O adatom pairs and charge transfer upon O_2 dissociation on reduced TiO_2(110), Phys. Chem. Chem. Phys. 2010. 12. 6337-6344.

[26] M. D. Rasmussen, L. M. Molina, B. J. Hammer, Adsorption, diffusion, and dissociation of molecular oxygen at defected TiO_2(110): A density functional theory study, J. Chem. Phys. 2004. 120. 988-997.

[27] E. Lira, S. Wendt, P. P. Huo, J. Hansen, R. Streber, S. Porsgaard, Y. Y. Wei, R. Bechstein, E. Lægsgaard, F. Besenbacher, Dissociative and molecular oxygen chemisorption channels on reduced rutile TiO_2(110): An STM and TPD study, Surf. Sci. 2010. 604. 1945-1960.

[28] Q. Zhu, Y. Adachi, Y. Sugawara, Y. J. Li. Tip-induced Dynamic Behaviors of Water Molecule and Hydroxyl on the rutile TiO_2(110) Surface, J. Phys. Chem. C. 2022. 126. 13062-13068.

[29] H. Ishii, K. Sugiyama, E. Ito, K. Seki, Energy level alignment and interfacial electronic structures at organic/metal and organic/organic interfaces, Adv Mater. 1999. 11. 605-625.

[30] T. C. Leung, C. L. Kao, W. S. Su, Y. J. Feng, C. T. Chan, Relationship between surface dipole, work function and charge transfer: Some exceptions to an established rule, Phys. Rev. B. 2003. 68. 195408.

[31] S. H. Dong, B. Lin, X. F. Cui, S. J. Tan, B. Wang, Photoresponses of supported Au single atoms on TiO_2(110) through the metal-induced gap states, J. Phys. Chem. Lett. 2019. 10. 4683-4691.

[32] A. L. Shluger, K. P. M., P. V. Sushko, D. M. Ramo, A. V. Kimmel, Modelling of electron and hole trapping in oxides, Model. Simul. Mater. Sci. Eng. 2009. 17. 084004-084014.

[33] C. Y. Guo, X. Z. Meng, H. X. Fu, Q. Wang, H. M. Wang, Y. Tian, J. B. Peng, R. Z. Ma, Y. X. Weng, S. Meng, E. Wang, Y. Jiang, Probing nonequilibrium dynamics of photoexcited polarons on a metal-oxide surface with atomic precision, Phys. Rev. Lett. 2020. 124. 20-22.

[34] M. Reticcioli, M. Setvin, M. Schmid, U. Diebold, C. Franchini, Formation and dynamics of small polarons on the rutile TiO_2(110) surface, Phys. Rev. B. 2018. 98. 4-15.

[35] C. Cheng, Y. H. Zhu, W. H. Fang, R. Long, O. V. Prezhdo, CO adsorbate promotes polaron photoactivity on the reduced rutile TiO_2(110) surface, JACS Au. 2021. 2. 234-245.

[36] Y. J. Zhang, O. Pluchery, L. Caillard, A. F. Lamic-Humblot, S. Casale, Y. J. Chabal, M. Salmeron, Sensing the charge state of single gold nanoparticles via work function measurements, Nano Lett. 2015. 15. 51-55.

[37] W. T. Yuan, B. E. Zhang, K. Fang, X. Y. Li, T. W. Hansen, Y. Ou, H. S. Yang, J. B. Wagner, Y. Gao, Y. Wang, Z. Zhang, In situ manipulation of the active Au-TiO_2 interface with atomic precision during CO oxidation, Sci. 2021. 371. 517-521.

List of Publications

1. **Q. Zhu**, Y. Sugawara, and Y. J. Li, "Exploration of CO movement characteristics on rutile TiO_2(110) surface", *Colloids and Surfaces A. Physicochemical and Engineering Aspects*, **656**, 130402, 2023.
2. **Q. Zhu**, Y. Adachi, Y. Sugawara, Y. J. Li, "Tip-induced dynamic behaviors of a water molecule and hydroxyl on the rutile TiO_2(110) surface", *The Journal of Physical Chemistry C*, **126**, 13062–13068, 2022.
3. **Q. Zhu**, R. Xu, Z. H. Cheng, Y. Sugawara, and Y. J. Li, "Charge state of Au nanoclusters on oxidized rutile TiO_2(110) surface by AFM/KPFM at 78 K", *Under Review*.
4. S. R. Zhou, J. Y. Wei, **Q. Zhu**, H. Q. Sang, Y. Sugawara, Y. J. Li, "Study of CO molecules on Pd/Al_2O_3/NiAl(110) surface by atomic force microscopy and Kelvin probe force microscopy", *Journal of Nanoparticle Research*, 2023.
5. H. Guo, X. Li, **Q. Zhu**, Z. R. Zhang, Y. S. Liu, H. F, Wen, Y. J. Li, J. Tang, J. Liu, "Imaging nano-defects of metal waveguides using the microwave cavity interference enhancement method", *Nanotechnology*, **31**, 455203, 2020.

List of Presentations

1. **Q. Zhu**, Y. Sugawara, and Y. J. Li, "Exploration of CO movement in two-dimensional on rutile TiO_2(110) surface by AFM at 78 K", The 22nd International Vacuum Congress, Sapporo, September, 2022. (Oral)
2. **Q. Zhu**, Y. Adachi, Y. Sugawara, and Y. J. Li, "Water molecule and hydroxyl manipulation on TiO_2(110) surface by AFM/KPFM", The 5th International Symposium on "Elucidation of Next Generation Functional Materials・Surface and Interface Prop", Osaka, October, 2021. (Oral, Invited)
3. **Q. Zhu**, Y. Adachi, Y. Sugawara, and Y. J. Li, "Exploration of charge properties of Au NPs on rutile TiO_2(110) surface by AFM/KPFM at 78 K", The 70th JSAP Spring Meeting 2023, Sophia University, March, 2023. (Poster)
4. **Q. Zhu**, Y. Sugawara, and Y. J. Li, "CO movement in two-dimensional on rutile TiO_2(110) surface", 2022年度関西薄膜・表面物理セミナー, Osaka, November, 2022. (Oral)
5. **Q. Zhu**, Y. Adachi, Y. Sugawara, and Y. J. Li, "Water molecule and hydroxyl adsorption properties on TiO_2(110) surface", The 69th JSAP Spring Meeting 2022, Aoyama Gakuin University, March, 2022. (Poster)

Acknowledgement

In my doctoral study, four years have passed by in a hurry. During the study abroad period, I have experienced new cultures and acquired new knowledge. It's a meaningful time in my life. Here, I would like to express my gratitude first and foremost to my tutor Prof. Yanjun Li. She gives me a chance to study abroad and receive different information. In my experiments and life, she also gives me a lot of support. Thank you very much! And I also appreciate Prof. Yasuhiro Sugawara, he gives me advice in my experiments.

I express my gratitude to all the members of the doctoral committee for their review and valuable contributions to improving my doctoral dissertation.

I would like to express my appreciation to assistant professor Yoshitaka Naitoh, he gives me advice and suggestions for my study. Moreover, I thank Huanfei Wen, Quanzheng Zhang, Yuuki Adachi, Masato Miyazaki, Shanrong Zhou and Zhang Qu, who share the experiment experience, and give me lots of experimental advice. I give many thanks to the lab members Miku Hirowatari, Hiroki Yamasaki, Jiuyan Wei, Yiqun Li, Tomo Nishino and Sota Odani for the helping in the experiment and the fun time in the lab. I thank the secretaries Kyoko Nakagawa and Ayaka Kitaichi, who help me a lot in my lab life. I would also like to express my thanks to all my friends, who helped me a lot.

Last but not least, I want to thank my parents and my family members for their continuous support and understanding during my doctoral study.